OPTICAL, STRUCTURAL, AND TRANSPORT PROPERTIES OF InN, $In_xGa_{1-x}N$ ALLOYS GROWN BY METALORGANIC CHEMICAL VAPOR DEPOSITION

by

NEELAM KHAN

M.Sc, University of the Punjab, 2000
M. Phil, University of the Punjab, 2003

AN ABSTRACT OF A DISSERTATION

submitted in partial fulfillment of the requirements for the degree

DOCTOR OF PHILOSOPHY

Department of Physics
College of Arts and Science

KANSAS STATE UNIVERSITY
Manhattan, Kansas

2009

Abstract

InGaN based, blue and green light emitting diodes (LEDs) have been successfully produced over the past decade. But the progress of these LEDs is often limited by the fundamental problems of InGaN such as differences in lattice constants, thermal expansion coefficients and physical properties between InN and GaN. This difficulty could be addressed by studying pure InN and $In_xGa_{1-x}N$ alloys.

In this context Ga-rich $In_xGa_{1-x}N$ ($x \leq 0.4$) epilayers were grown by metal organic chemical vapor deposition (MOCVD). X-ray diffraction (XRD) measurements showed $In_xGa_{1-x}N$ films with x= 0.37 had single phase. Phase separation occurred for x ~ 0.4. To understand the issue of phase separation in Ga-rich $In_xGa_{1-x}N$, studies on growth of pure InN and In-rich $In_xGa_{1-x}N$ alloys were carried out.

InN and In-rich $In_xGa_{1-x}N$ (x~0.97- 0.40) epilayers were grown on AlN/Al_2O_3 templates. A Hall mobility of 1400 cm^2/Vs with a carrier concentration of $7x10^{18}cm^{-3}$ was observed for InN epilayers grown on AlN templates. Photoluminescence (PL) emission spectra revealed a band to band emission peak at ~0.75 eV for InN. This peak shifted to 1.15 eV when In content was varied from 1.0 to 0.63 in In-rich $In_xGa_{1-x}N$ epilayers. After growth parameter optimization of In- rich $In_xGa_{1-x}N$ alloys with (x= 0.97-0.40) were successfully grown without phase separation.

Effects of Mg doping on the PL properties of InN epilayers grown on GaN/Al_2O_3 templates were investigated. An emission line at ~ 0.76 eV, which was absent in undoped InN epilayers and was about 60 meV below the band edge emission peak at ~ 0.82 eV, was observed to be the dominant emission in Mg-doped InN epilayers. PL peak position and the temperature dependent emission intensity corroborated each other and suggested that Mg acceptor level in InN is about 60 meV above the valance band maximum.

Strain effects on the emission properties of InGaN/GaN multiple quantum wells (MQWs) were studied using a single blue LED wafer possessing a continuous variation in compressive strain. EL emission peak position of LEDs varies linearly with the biaxial strain; a coefficient of 19 meV/GPa, characterizes the relationship between the band gap energy and biaxial stress of $In_{0.2}Ga_{0.8}N$/GaN MQWs.

OPTICAL, STRUCTURAL, AND TRANSPORT PROPERTIES OF InN, $In_xGa_{1-x}N$ ALLOYS GROWN BY METALORGANIC CHEMICAL VAPOR DEPOSITION

by

NEELAM KHAN

M.Sc, University of the Punjab, 2000
M. Phil, University of the Punjab, 2003

A DISSERTATION

submitted in partial fulfillment of the requirements for the degree

DOCTOR OF PHILOSOPHY

Department of Physics
College of Arts and Science

KANSAS STATE UNIVERSITY
Manhattan, Kansas

2009

Approved by:

Major Professor
Dr. Hongxing Jiang

Copyright

Abstract

InGaN based, blue and green light emitting diodes (LEDs) have been successfully produced over the past decade. But the progress of these LEDs is often limited by the fundamental problems of InGaN such as differences in lattice constants, thermal expansion coefficients and physical properties between InN and GaN. This difficulty could be addressed by studying pure InN and $In_xGa_{1-x}N$ alloys.

In this context Ga-rich $In_xGa_{1-x}N$ ($x \leq 0.4$) epilayers were grown by metal organic chemical vapor deposition (MOCVD). X-ray diffraction (XRD) measurements showed $In_xGa_{1-x}N$ films with x= 0.37 had single phase. Phase separation occurred for x ~ 0.4. To understand the issue of phase separation in Ga-rich $In_xGa_{1-x}N$, studies on growth of pure InN and In-rich $In_xGa_{1-x}N$ alloys were carried out.

InN and In-rich $In_xGa_{1-x}N$ (x~0.97- 0.40) epilayers were grown on AlN/Al_2O_3 templates. A Hall mobility of 1400 cm^2/Vs with a carrier concentration of $7x10^{18}cm^{-3}$ was observed for InN epilayers grown on AlN templates. Photoluminescence (PL) emission spectra revealed a band to band emission peak at ~0.75 eV for InN. This peak shifted to 1.15 eV when In content was varied from 1.0 to 0.63 in In-rich $In_xGa_{1-x}N$ epilayers. After growth parameter optimization of In- rich $In_xGa_{1-x}N$ alloys with (x= 0.97-0.40) were successfully grown without phase separation.

Effects of Mg doping on the PL properties of InN epilayers grown on GaN/Al_2O_3 templates were investigated. An emission line at ~ 0.76 eV, which was absent in undoped InN epilayers and was about 60 meV below the band edge emission peak at ~ 0.82 eV, was observed to be the dominant emission in Mg-doped InN epilayers. PL peak position and the temperature dependent emission intensity corroborated each other and suggested that Mg acceptor level in InN is about 60 meV above the valance band maximum.

Strain effects on the emission properties of InGaN/GaN multiple quantum wells (MQWs) were studied using a single blue LED wafer possessing a continuous variation in compressive strain. EL emission peak position of LEDs varies linearly with the biaxial strain; a coefficient of 19 meV/GPa, characterizes the relationship between the band gap energy and biaxial stress of $In_{0.2}Ga_{0.8}N$/GaN MQWs.

Table of Contents

List of Figures

List of Tables

Acknowledgement

All praise to almighty Allah, the most merciful and beneficent, who gave me the potential and ability to complete this research work successfully. Without his blessings and guidance it would not have been possible to achieve this degree.

I don't have enough words to express my deep indebtedness to my parents for their prayers, love, trust, and moral support all the way in my life. I am grateful to them for sending me far away from them for so many years to achieve my goal of doctoral studies. This dissertation was impossible without their love and support.

I would like to specially thank my advisors Dr. Hongxing Jiang and Dr. Jingyu Lin for their valuable suggestions, encouragement and guidance throughout my research work.

Thanks to Dr. Jing Li for teaching me III- nitride growth and characterization techniques and for the informative discussions. I would also like to thank Dr. Cris Ugolini for helping me to learn MOCVD growth system, and how to fix technical problems in it. I would like to acknowledge past and present group members, Professor Sixuan Jin, Dr. Zhaoyang Fan, Dr. Mim Lal Nakarmi, Dr. Neeraj Nepal, Dr. Talal Al Tahtamouni, Rajendra Dahal, Bed Nidhi Pantha, Ashok Sedhain and Weiping Zhao for their cooperation, assistance and useful discussions.

Very special thanks to Dr. James Edgar for serving as my committee member and providing constant support, valuable suggestions and assistance through out my research work. I appreciate his deep interest in my research progress and guidance on how to become a successful researcher in future. I am grateful to my committee member, Dr. Oshea for his valuable advice from time to time and motivation. Furthermore, I am thankful to Dr. Mark Hollingsworth and Dr. Kevin Lease for serving on my advisory committee.

I would like to thank Dr. Sanjay Rebello and Dr. Tim Bolton for their valuable suggestions, and guidance on how to become a good teacher.

I am thankful my teacher Dr. Mujahid Kamran from Pakistan who guided and encouraged me for doctoral studies, while I was doing M.Phil from University of the Punjab. I appreciate his interest in the progress of my studies and research.

Thanks to my M.Phil supervisor, Dr. Sadat Anwar Siddique from Pakistan for his interest in my doctoral research progress.

I would like to acknowledge my brothers and sisters, Naureen, Iram, Khurram, Naveed and Zeeshan for their love and support.

I am thankful to Dr. Talat Rahman for her guidance and encouragement from time to time. And her family members, especially Nosheen and Sharyar's family, who took care of me like their own family member, in times of stress and was always available to provide me moral support and encouragement.

At last, I am thankful to all of my friends around me for their continuous support especially Chandana Ghosh and Samina Zia.

Dedication

To my loving parents

CHAPTER 1 - Introduction

III-V wide band gap nitrides include aluminum nitride (AlN), gallium nitride (GaN), indium nitride (InN) and their alloys. All of these are compounds of nitrogen which is the smallest element from group V in the periodic table. Very strong chemical bonds result within the III-nitride material system due to the large difference in electro-negativity between group III and V elements. AlInGaN alloys are direct band gap energy materials whose energy can be tuned from 0.7 eV for InN to 6.2 eV for AlN. These energies correspond to a wavelength range from 200 nm to 1700 nm which covers the ultraviolet to infrared spectral bands. Due to the mechanical hardness and larger band gaps of III-V nitrides, they can operate at high temperatures and power levels. Intrinsically radiative recombinations in III-nitrides result in high speed of carriers, and along with the large band offset of 2.7 eV and 5.4 eV for GaN/AlN and InN/AlN hetrostructures respectively, the design of quantum well based devices with high quantum efficiencies are permissible. III-nitride based devices are potentially attractive for applications such as laser diodes, light emitting diodes, solar blind UV detectors, and high power electronic devices such as transistors and thyristors. Photonic devices based on III-nitrides, particularly UV/blue light sources, have promising applications in early missile threat detection and interception, chemical-bio-agent detection, and as high optical storage density media. InGaN based blue /green light emitting diodes are already in use in full color liquid crystal diode (LCD) displays and traffic lights, whereas blue laser diodes are predicted to replace red lasers in the current CD/DVD read/write systems [1], [Reference [1] provides a good overview of these applications].

As of today, III-nitrides have gained a significant position in the science and technology of compound semiconductors, as well as in modern electronic and optical devices.

1.1 Crystal Structure and properties of III-nitrides

The energy band gap of a semiconductor is its most important parameter, and determines its transport and optical properties as well as many other phenomenons. Figure 1.1 compares the bandgap energy versus lattice constants (a) of III- V nitrides with that of various semiconductors such as SiC, GaAs, and ZnSe [2]. It has been found that the true band gap of InN is ~ 0.7 eV instead of the 1.9 eV value found in earlier studies [3]. The band gap energies of nitride materials cover the entire range from infrared to ultraviolet in the electromagnetic spectrum.

Conventional semiconductors, such as silicon (Si) or gallium arsenide (GaAs) have cubic symmetry with diamond or zinc-blende crystal structure. III-nitride semiconductors crystallize in stable wurtzite lattice structure. Nitrogen atoms form a hexagonal close packed structure (hcp) and half of the tetrahedral sites are occupied by group III element in the hcp lattice. The InN crystal structure along the c-axis is considered as a layered structure with atoms in hexagons stacked in a sequence of $In_AN_AIn_BN_BIn_AN_AIn_BN_B$….. . The zinc blende structure differs from the wurtzite structure by the stacking sequence of $In_AN_AIn_BN_BIn_CN_CIn_AN_A$…. III-nitride materials grown by MOCVD have wurtzite structure. Figure 1.2 shows the hexagonal wurtzite lattice structure of III-V nitride with nitrogen atoms represented by gray circles and group III-elements represented by yellow ones. Each III-atom represented by yellow circles is coordinated by four nitrogen atoms and vice versa [4].

III-nitrides are polar crystals because of the absence of a center of symmetry along the c-axis, which leads to many potentially useful properties such as piezoelectricity, pyroelectricity and non linear optical properties. Wide band gap III-nitrides especially GaN possess lower carrier concentrations as compared to Si and GaAs over a larger temperature range. Low leakage and dark current is the consequence of this lower carrier concentration, which is important for photodetectors and electronic devices. The strong chemical bonding within III-nitrides results in high melting points, mechanical strength and chemical stability of these materials. These materials also possess good thermal conductivity. III-nitride based devices can operate at high temperatures as well as in hostile environments [1, 5]. Some of the extraordinary physical properties of III-nitrides are listed in the Table 1.1[1]

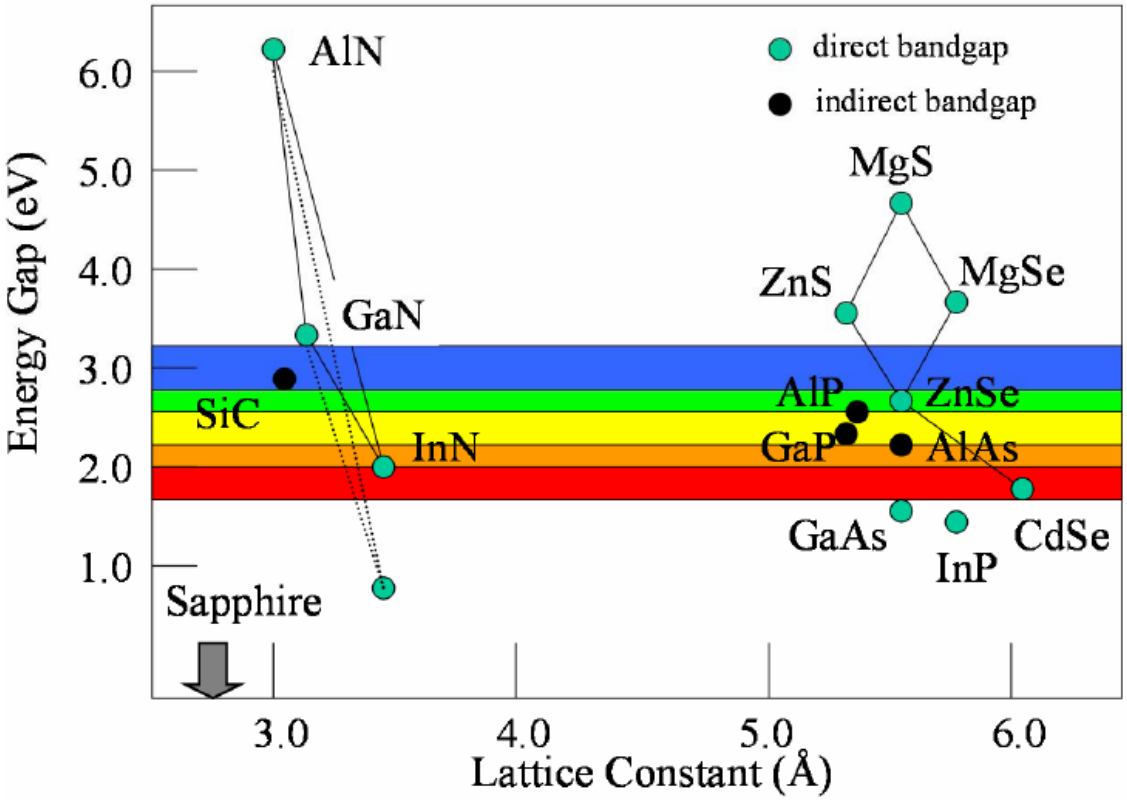

Figure 1.1 Bandgap energy of various semiconductors versus in-plane lattice constant [2]. Recent work indicates that band gap of InN is around 0.7 eV [3].

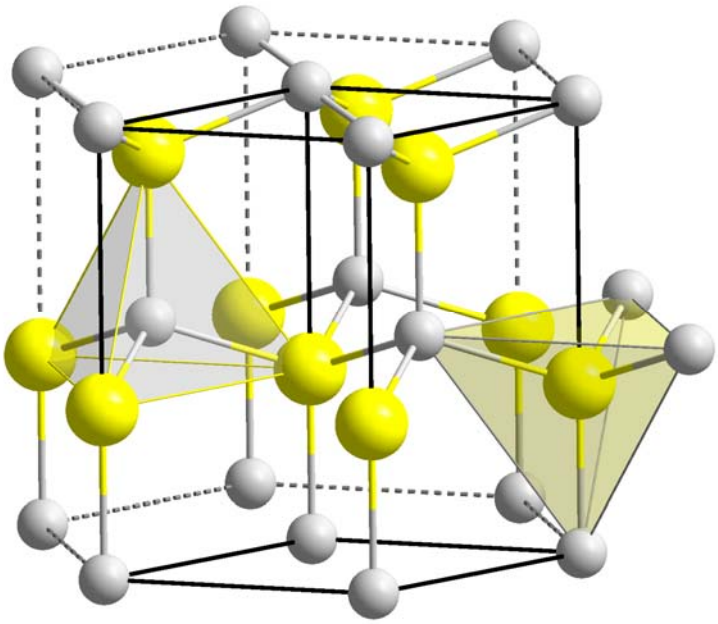

Figure 1.2 Schematic illustration showing the wurtzite lattice structure of III-V nitrides with N atoms represented by gray circles and group III-elements represented by yellow ones [4]

Table 1.1 Physical properties of III-nitride materials [1]

	AlN	GaN	InN
300 K energy gap (eV)	6.2	3.44	0.7
Lattice constant, a (Å)	3.112	3.189	3.545
Lattice constant, c (Å)	4.982	5.186	5.703
Electron effective mass m_e	0.4	0.2	0.05
Hole effective mass m_h	2.7	0.8	0.5
ε (0)	9.14	10.4 (E$\parallel$c) 9.5 (E$\perp$c)	15.3
ε (∞)	4.84	5.8 (E$\parallel$c) 5.4 (E$\perp$c)	9.3
Thermal expansion coefficient α_a (10^{-6} K^{-1})	5.27 (20-800^{o}C)	4.3 (17-477^{o}C)	5.6 (280^{o}C)
Thermal expansion coefficient α_c (10^{-6} K^{-1})	4.15 (20-800^{o}C)	4.0 (17-477^{o}C)	3.8 (280^{o}C)
Melting point (° C)	3000	> 1700	1100
Thermal conductivity κ (W/cm K)	2.0	1.3	0.8
Refractive index, n	2.2 (0.60 μm)	2.35 (1.0 μm)	2.56 (1.0 μm)

1.2 Brief history of nitride development

The first AlN, GaN and InN compound semiconductors were grown in 1907[6], 1910[7], and 1932[8], respectively. Sapphire has been widely used as a substrate for the growth of III-V nitride epilayers although it has a 13.8 % lattice mismatch. As the epitaxial growth had to be performed on foreign substrates, it made it impossible to grow bulk III-nitride crystals and only poor quality GaN films could be grown. A breakthrough occurred in GaN research, when GaN epilayer growth was reported by hydride vapor phase epitaxy (HVPE) in 1969 [9]. HVPE is a suitable technique for producing bulk materials which can be used to study many of their physical properties. Metalorganic chemical vapor deposition (MOCVD) was first developed for GaN in 1971, and is now the most common technique for producing epitaxial thin films[10].

The research of GaN epilayers was interrupted from 1970-1980 due to the difficulty in growing crystals of high quality especially p-type GaN. Two fundamental breakthroughs were made in the 1980. The first one was the introduction of a low temperature ~500^{o}C GaN buffer layer to reduce the lattice mismatch between sapphire and GaN thin films. This buffer layer allowed the growth of good quality GaN on a foreign substrate in 1983 [11]. The second was the demonstration of Mg-doped GaN through low energy electron beam irradiation (LEEBI) in 1989 [12]. The passivation of Mg acceptors by hydrogen was the main difficulty in obtaining p-GaN. The activation of Mg-type acceptors was done by using rapid thermal annealing in N_2 ambient or vacuum at temperatures above 750^{o}C in 1992 [13]. These advances led to the impressive research and development work in III-nitride based compound semiconductor science and technology which resulted in the realization of ultraviolet, violet, blue and green light emitting diodes (LEDs) and laser diodes (LDs) [14-21]. Although remarkable progress has been made in GaN and low indium composition~ 20% in $In_xGa_{1-x}N$ material growth and development based on these devices, still much research is required to improve the device performance. Achieving high quality InN and In-rich InGaN is another challenging task. Relatively little attention has been devoted to the growth of InN and In-rich InGaN alloys in spite of their potential for achieving full color emission by varying the In content.

This dissertation will cover research in the areas of undoped and Mg-doped InN, Ga-rich and In-rich InGaN epilayers, and the effect of compressive strain on InGaN/GaN quantum wells for solid state lighting and solar cell applications.

1.3 InN and In-rich InGaN alloys

The recent discovery of the narrow band gap of InN ~ 0.67± 0.05 eV, which is smaller than previously reported band gap of 1.9 eV, has attracted extensive interest for the optical communication in the infrared wavelength region [22-30]. Among all the III-nitride semiconductors, InN exhibits the highest electron mobility and saturation velocity due to the lower effective mass for electrons [31]. The theoretically calculated values of mobility for InN and GaN are about 4400 and 1000 cm^2/ Vs respectively [32]. To date, molecular beam epitaxy (MBE) grown samples showed the highest electron mobility of about 2200 cm^2/Vs with an electron concentration of $3x10^{17}$ cm^{-3} [33]. InN based field effect transistors (FETs) are predicted to have a tremendously high speed with a cutoff frequency of over 1 THz for 0.1 μm gates. Thus InN is considered to be a potential material for the fabrication of high speed and performance hetrojunction field effect transistors (HFETs). As compared to GaN and AlN, the use of InN would allow photonic devices in the red wavelength region as well as for faster electronic devices. InN based optoelectronic devices have the potential of a red emitter with no toxic elements, such as arsenic and phosphorus in GaAs, and GaP based devices. In addition, InN is a potential material for low cost high efficiency solar cells [34].

$In_xGa_{1-x}N$ alloys with energies from 0.7 to 3.4 eV can be tuned from ultraviolet to near infrared region by varying the In content. Figure 1.3 shows the band gap energy verses Ga content in $In_{1-x}Ga_xN$ alloys which covers almost the whole solar spectrum range. One can get the useful part of solar spectrum by varying Ga content between 0 and 0.63 in the $In_{1-x}Ga_xN$ alloys, which varies band gap energies from 0.7 to 2.4 eV. Figure 1.3 also shows the band gap energies of currently used materials for high efficiency multijunction (MJ) solar cell such as Ge (0.66 eV), GaAs (1.43 eV) and GaInP (1.9 eV).

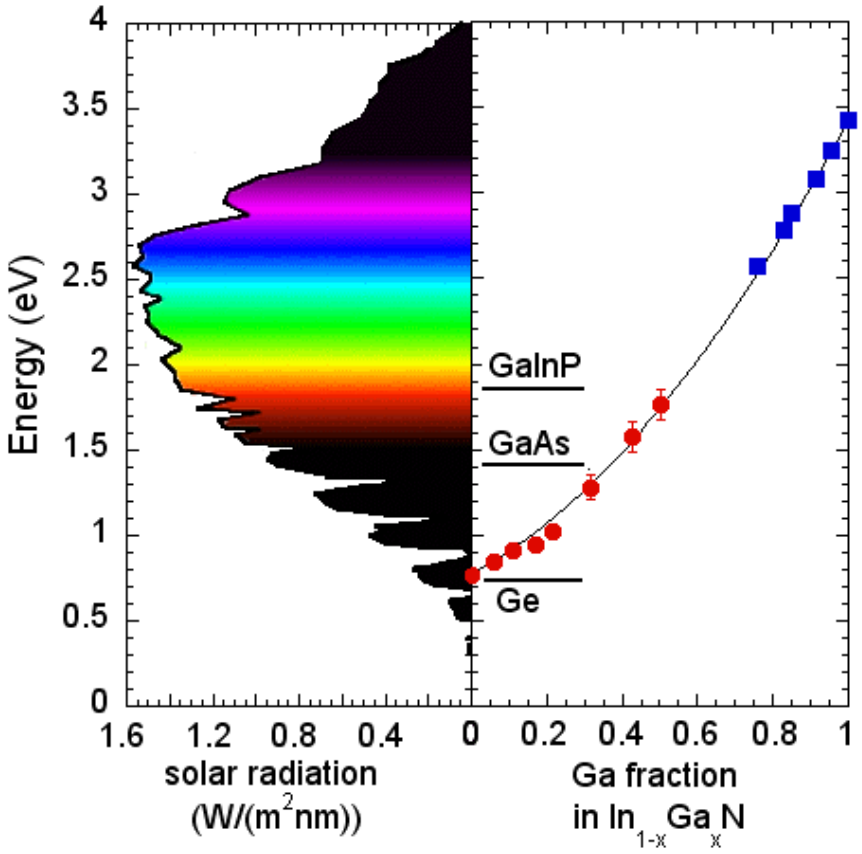

Figure 1.3 Band gap energy of InGaN alloys system cover the entire solar spectrum. The gap energies of conventional multijunction (MJ) solar materials (Ge, GaAs, and GaInP) are also shown in the right hand panel for comparison [29].

The deposition process of currently high efficiency MJ solar cells require a number of different precursor streams such as Al, In, Ga, As and P and up to 20 different layers including the tunnel junctions. Thus it is potentially attractive to design the MJ solar cells using a single ternary alloy system of InGaN, as it provides the flexibility of choosing the number and band gap energies of the constituent junctions. Furthermore, InGaN alloys have great potential for use in solar cells for space applications as they offer a higher degree of resistance to radiation damage [29,35].

InGaN based blue-green LEDs and LDs have already been successfully fabricated that employ $In_xGa_{1-x}N$ films with lower In contents of about $x < 0.2$ [36]. Recently, the properties of $In_xGa_{1-x}N$ films with a higher In content $x > 0.5$ have also been investigated by several research groups [37-40].

Furthermore, the growth of InN based quantum well (QW) structures with wavelength emission at approximately 1.55 μm was reported, in which the barrier $In_xGa_{1-x}N$ layers with x= 0.7-0.8 were used [41]. In general the phase separation issue makes it very difficult to grow In-rich InGaN with higher In content [42, 43]. Also the growth temperature of InN and In-rich InGaN epilayers is limited to the 500-750^oC range due to the large vapor pressure of N_2 over InN [34]. This lower temperature results in poor crystalline quality due to the lower decomposition rate of ammonia, which acts as a source of nitrogen. In fact the crystalline quality of In-rich InGaN is considerably poorer than that of InGaN films with a lower In content, and the crystalline quality of InN is much better than that of In-rich InGaN according to different reports [38, 34]. Optical devices employing InN-InGaN hetrostructure quantum wells require the growth of high quality In-rich InGaN epilayers.

1.4 Native defects and electron concentration

As is discussed in the above section there are many potential applications of InN, but many important properties such as band gap energy of this material and origin of high electron concentrations in nominally undoped InN are still under debate.

Conduction band density of states and smallest effective mass of InN has significant consequences for the effects of unintentional n-type doping on its band gap

energy. When carrier concentrations are such that they partly fill the conduction band, it is regarded as an effect called Burstein-Moss shift. Earlier reported larger band gap energy values of InN ~ 1.9 eV can be attributed to this Burstein-Moss shift [44, 45]. Thus the band gap energy when measured by optical absorption spectroscopy is overestimated due to the transition of excited electrons from the Fermi level within the conduction band to the top of valance band.

It was realized early that InN exhibits an exceptional tendency for n-type conductivity. As grown undoped InN is always n-type with a very high background electron concentration as high as $10^{21}cm^{-3}$[34]. The major reason behind this high n-type conductivity is still unclear. Oxygen and hydrogen impurities are the potential causes of the unintentional *n*-type conductivity in as-grown InN films [46-48]. On the other hand nitrogen vacancies can also be considered as a defect responsible for the unintentional n-type character of InN [49, 50]. There had been many experimental reports also which supports this view [51, 52]. It was observed experimentally that the background electron concentration decreases and Hall mobility increases by increasing the NH_3/TMI in MOVPE grown InN epilayers. Also the higher NH_3 decomposition rate at high temperatures provides more reactive nitrogen that results is improved transport properties [34]. More recently, it is widely accepted that InN films possess a surface electron accumulation layer due the pinning of Fermi level at about 0.8 eV above the conduction band minimum due to intrinsic surface states [22, 53, 54]. This electron accumulation layer is localized within the first 5nm of the InN film surface with an electron concentration as high as 10^{21} cm^{-3} [55]. It creates problems when assessing the effects of p-type dopants in InN films, as direct electric contact to the bulk is prevented by it. Eliminating this electron accumulation layer is extremely challenging since it is an intrinsic property of InN resulting from the nature of its bulk band structure. In fact, this is perhaps the main problem in the realization of InN based devices where electron accumulation layer is unwanted. Sensors, terahertz emitters, spintronics device and semiconductor/superconductor hybrid devices are the possible applications that utilize surface electron accumulation layer [56].

In order to realize InN based optoelectronic devices, it is essential to achieve InN with p-type conductivity. However due to the high unintentional n-type electron

concentration and electron accumulation layer, the growth of p-type InN has proven to be very challenging. Only very recently p-type InN using Mg acceptors been demonstrated by capacitance-voltage measurements which indicates the conductivity due to acceptors below the n-type surface [55, 57]. This electron accumulation layer isolated the surface from p-type bulk and prevents the electrical contact to the material.

1.5 Challenges in controlling p-type Conductivity in III-nitrides

Controlling especially p-type conductivity in III-nitrides is important to the realization of optical devices. Figure 1.4 shows the band gap energies of III-nitrides along with the Fermi level stabilization energy (E_{FS}), which measures the average dangling bond energy when defects are introduced. It is located at about 0.8 eV and 1.5 eV above the conduction band and valance band edges respectively of InN. Recent studies by high electron energy loss spectroscopy of the InN surface confirmed the position of E_{FS}, which shows that Fermi energy is pinned about 1.64 eV above the valance band edge [22,58].

This Fermi level lying within the conduction band of InN has very important consequences for its doping properties. The extreme tendency of InN for unintentional n-type doping of InN can be explained by the Amphoteric Defect Model. According to this model the location of conduction and valance band edges relative to E_{FS} determines the doping behavior of semiconductors. The higher the location of the valance band edge, the easier it is to make p-type semiconductor. If we compare the prospects of p–type doping in InN with that of GaN, the hole concentration of 10^{18} cm^{-3} in the Mg- doped correspond to the Fermi energy of $E_F = E_{FS}$- 2.3 eV. It would be possible to dope InN with p-type to extent higher than GaN, if the same position of Fermi energy can be achieved as can be seen in figure 1.4

However, successful p-type doping of InN requires the elimination of surface electron accumulation as well as possible donor impurities and defects [58,59].

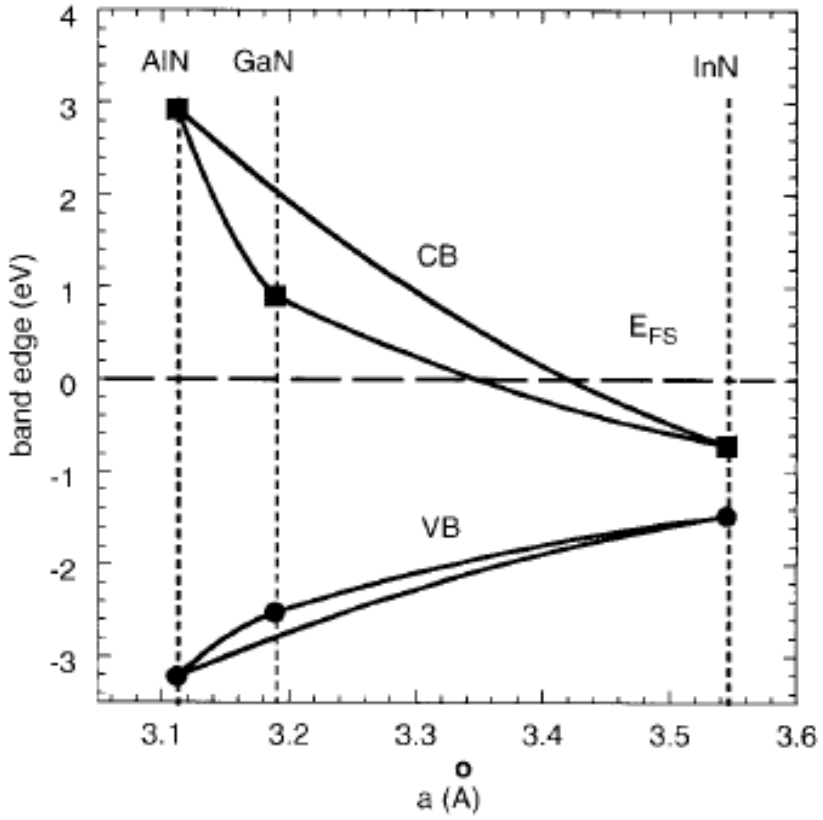

Figure 1.4 The calculated valance and conduction band edges of group III-N ternary alloys verses in-plane lattice constant. All the band gap energies are references to the Fermi level stabilization [58].

1.5 Outline of the dissertation

InGaN based, blue and green light emitting diodes (LEDs) have been produced successfully over the past decade. But due to the large differences in lattice constants and thermal expansion coefficients and mechanical properties between InN and GaN, the progress of these LEDs is limited. This difficulty could be addressed by studying pure InN and $In_xGa_{1-x}N$ alloys. Also it is useful to get information about the band gap energy of these materials. In this context systematic studies had been made on the growth and characterization of InN and $In_xGa_{1-x}N$ alloys. This dissertation is divided into four main chapters. A brief introduction is given in this chapter. The experimental set up for the growth and characterization of materials are given in chapter 2. The experimental results and discussions are given in chapter 3. Finally a general conclusion is presented in chapter 4.

CHAPTER 2 - Experimental apparatus and techniques

This chapter briefly describes the experimental set up used for the material growth and characterization techniques to study the crystalline quality, surface morphology, transport, and optical properties of the materials in this work.

2.1 Metal organic chemical vapor deposition system

Although there are many techniques to grow III-nitrides but metal organic chemical vapor deposition (MOCVD) and molecular beam epitaxy (MBE) are the major techniques among them.

In MBE growth, the constituent elements of III-nitrides are deposited in the form of molecular materials on a heated substrate to form an epitaxial layer. The low growth temperature and lack of sufficient radical nitrogen atoms are the main problems for MBE growth of III-nitrides. As a result, it has been very difficult to obtain p-type materials by MBE, which limits its use for producing light emitting structures based on III-nitrides. Nevertheless, MBE has been very successful in producing some unique polar structures such as field effect transistors (FETs), in which p-type material is avoided. Furthermore it had been a successful technique to grow InN, p- type InN and In-rich InGaN epilayers that require low growth temperature.

On the other hand MOCVD technology is an efficient technique to grow III-nitride materials and devices, which require high growth temperature. MOCVD utilizes metalorganic sources from group III-elements. The group V element is usually a hydride such as ammonia (NH_3) to provide reactive nitrogen. Typically the hydride reacts with the metalorganic source in hydrogen or nitrogen ambient under proper temperature and pressure conditions. Molecules of required semiconductor material are produced, which then adsorbs on the substrate surface to produce an epitaxial layer. Most of the materials mentioned in this dissertation were grown by a home built metal organic chemical vapor deposition (MOCVD) system. A commercial, Thomas Swan MOCVD system has also been used to grow device structures mentioned in this work. Figure 2.1 shows the photograph of MOCVD system used in this work.

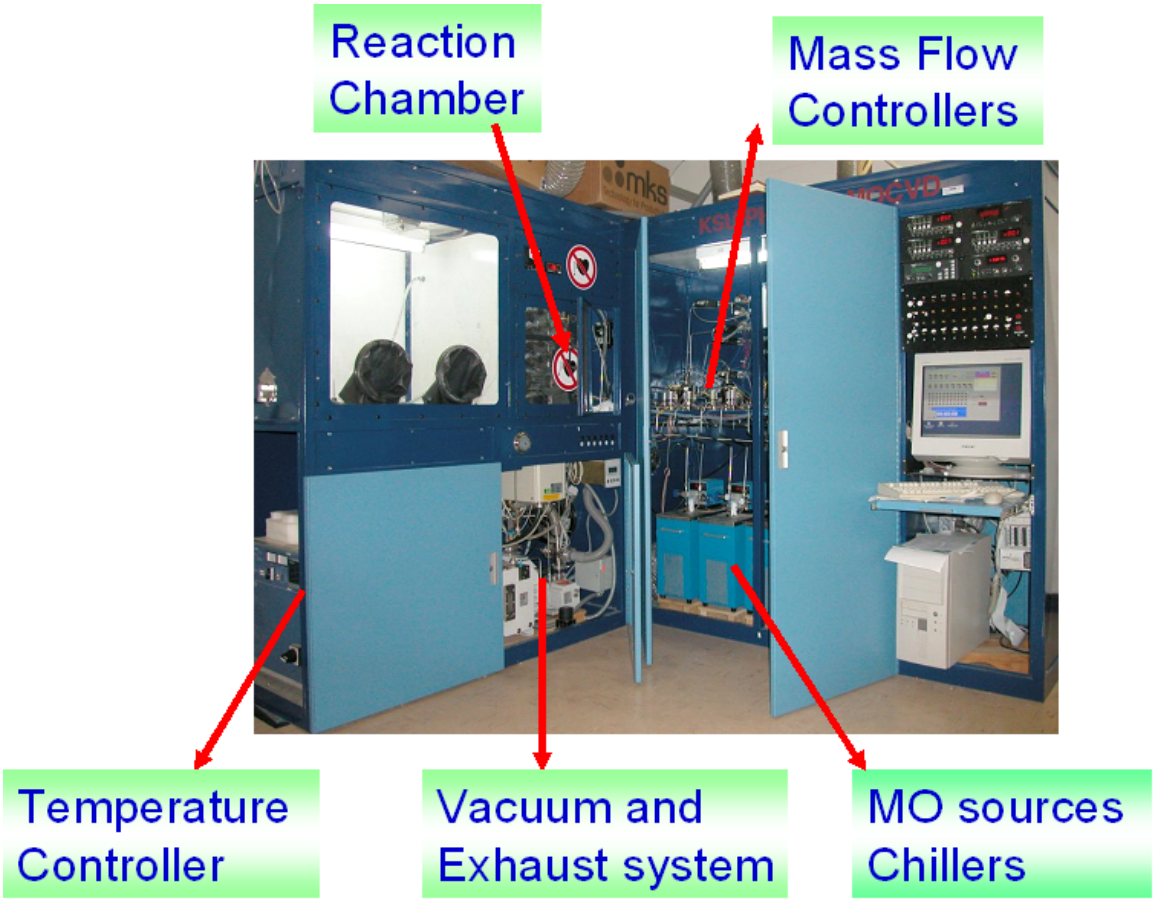

Figure 2.1 Photograph of the MOCVD system used for this work

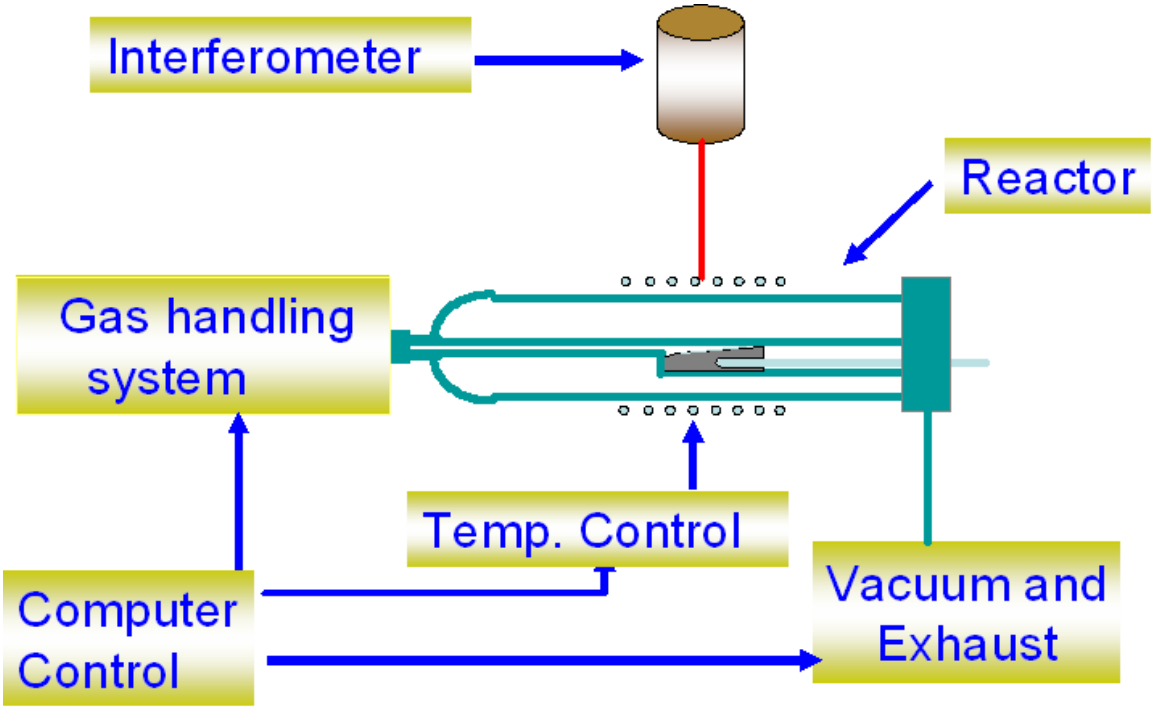

Figure 2.2 Schematic diagram of MOCVD system used for this work

The MOCVD system mainly consists of five main parts: the gas handling system, the reactor, the heating system, the exhaust and vacuum system, and interferometer for *insitu* monitoring. The schematic diagram of MOCVD system is shown in figure 2.2.

The main part of the system is the reactor part where growth reaction takes place. System has a horizontal, rectangular-shaped quartz reactor. A boron nitride (BN) coated graphite susceptor is used to hold the substrate. A 10 kW RF generator (TIG- 10/100) is used to heat up the susceptor. The temperature of the susceptor is measured by an R type thermo-couple (Platinum/Rhodium alloy) inserted in the susceptor through a quartz tube. The temperature is controlled by a Eurotherm temperature controller (Model-904).

The system has four metal-organic (MO) sources trimethylgallium (TMGa), triethylgallium (TEGa) for Ga, Trimethylindium (TMIn) for In, bicyclopntadinayl magnesium (CP_2Mg) for Mg obtained from Epichem Inc. All MO sources are temperature and pressure controlled to ensure constant vapor pressure. They are held in stainless steel bubblers mounted in temperature controlled chillers. The temperatures of the bubblers that contain TMGa, TEGa, TMIn, Cp_2Mg are set at 3, 21, 21, and 21^oC respectively. Blue ammonia (99.99994%) was used as the N source.

High purity hydrogen (99.999%) passed through a palladium purifier is used as carrier gas. A separate line for N_2 was employed so that growth can be carried out in H_2, N_2. To reduce the pre-reaction of metal-organic sources with ammonia, it was introduced in the reactor by a separate line. The bubbler pressures were maintained at 910 torr during material growth. The flow rates of all gases and MO sources controlled by computer through pneumatic valves and mass flow controllers (MFC). These valves and MFC are controlled by computer through a PIO-96 card.

To pump down the system to low pressure, a high capacity mechanical pump (Pfeiffer DUO-350) with oil filter pump was used . A turbo pump coupled into this system is employed to pump down to vacuum ($1x10^{-5}$ torr) before the growth. Pressure in conjunction was adjusted thought a pressure controller (MKS-Type 651 C), a pressure sensor (MKS-type 722) and a throttle valve (MKS-type-653) . An interferometer (Epieye-2000) was attached to the growth chamber for *insitu* monitoring of growth rate, thickness and qualitative monitoring of surface for epilayers. An ORS Epieye has a laser of wavelength 670 nm and a detector assembled in a stage to produce the interference

pattern. A computer interfaced control unit receives the signal from the detector when interference occurs from light reflected from surfaces of sapphire and growing epilayer.

Figure 2.3 shows a typical interference pattern for GaN and InN epilayer growth on sapphire substrate. Growth rate can be calculated directly from the width between two maxima or minima. Figure 2.4 shows the temperature profile of InN epilayer grown on sapphire. It helps to monitor the actual temperature of suceptor during growth of different epilayers.

To interface all aspects of the MOCVD system, a custom designed control chassis in conjunction with a Ni-Daq board and a specialized Delphi software program was employed. The software program allows for direct input of varying growth parameters in recipe format. The software also automates the growth process thus reducing operator error and time lag of manual input.

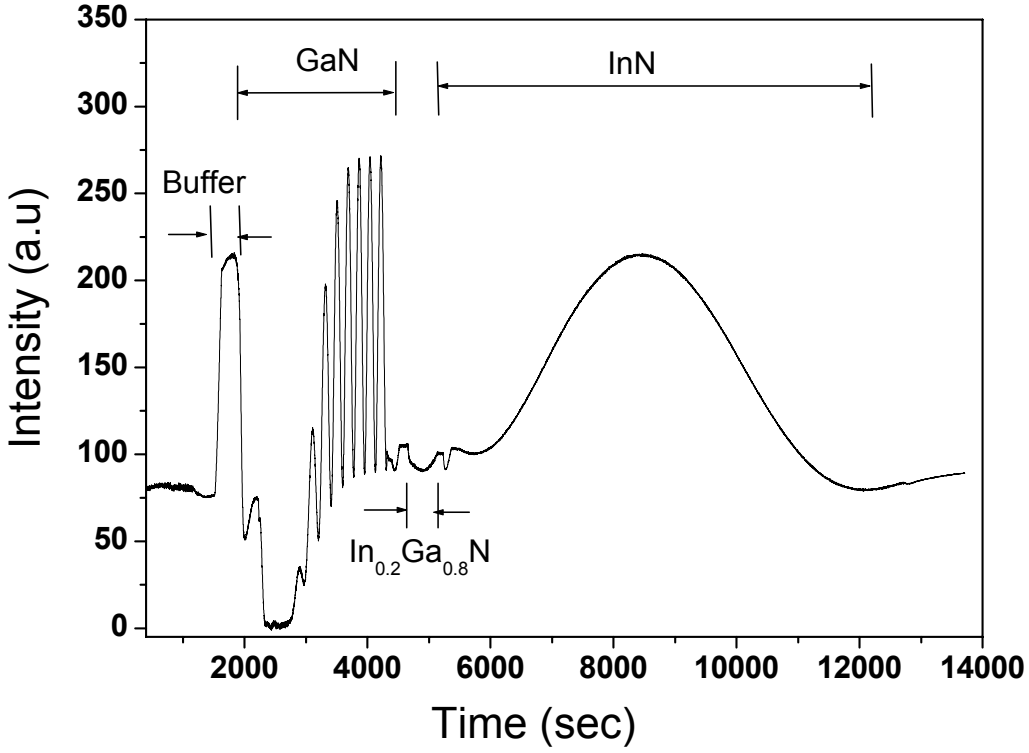

Figure 2.3 Interference pattern of an InN epilayer growth on GaN/ Sapphire template

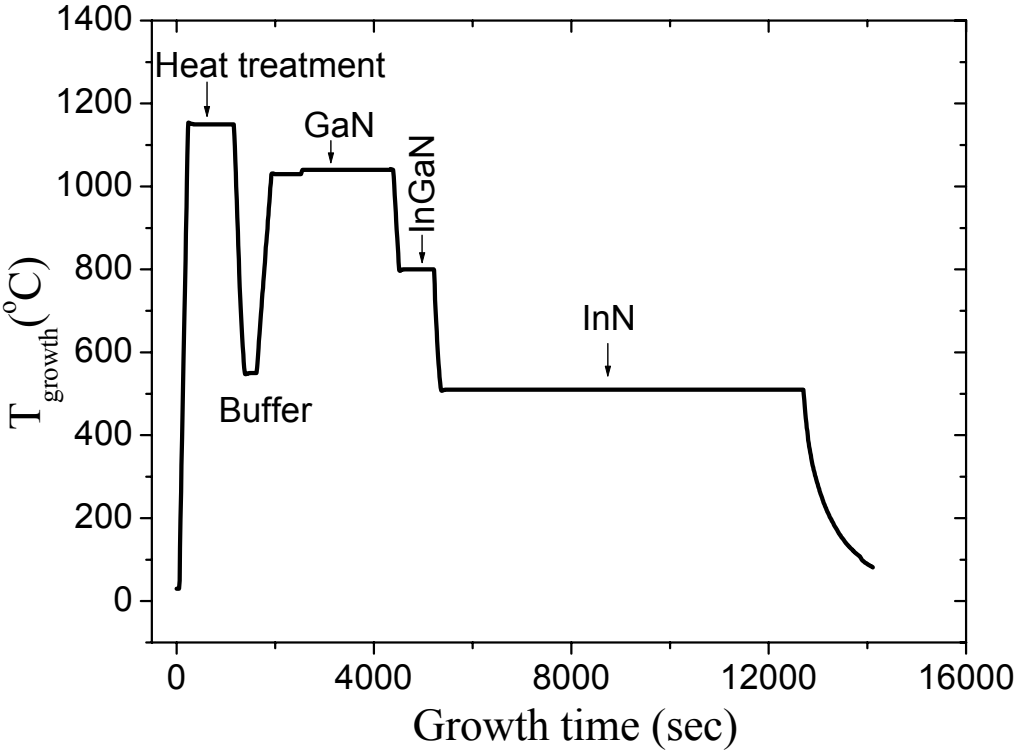

Figure 2.4 Growth temperature profile of an InN epilayer grown on Sapphire

2.2 Characterization Techniques:

Characterization of samples after growth is important in order to improve the material quality and other properties. There are many characterization techniques to do optical and electrical characterization and to study crystalline quality and surface morphology. Some of techniques are described below that were used in our study.

2.2.1 X-Ray Diffraction (XRD) system

X-ray diffraction (XRD) is a very useful tool to determine the crystalline quality, lattice constants, alloy compositions for GaN, InN, AlN and their alloys and strain in the epilayers. This basic principle behind this technique is detection of scattering from different crystal planes. When X-rays of wavelength λ are incident on a crystal, constructive interference from lattice planes can be described by Bragg's Law.

$$2d_{hkl} \sin\theta = n\lambda \tag{2.1}$$

Where d_{hkl} is the lattice plane spacing for a given miller indices, and n is the order of diffraction. The lattice spacing for hexagonal crystal system is given as

$$d_{hkl} = \frac{1}{\sqrt{\frac{4}{3}\left(\frac{h^2 + hk + k^2}{a^2}\right) + \frac{l^2}{c^2}}} \tag{2.2}$$

Where a and c are in-plane and out of plane lattice constants, and hkl are the miller indices, respectively [60].

According to Vegard's law, the lattice constants of alloys, such as $In_xGa_{1-x}N$ for a given value of x can be calculated by a linear extrapolation between those of the binaries, GaN and InN.

$$a\ (In_xGa_{1-x}N) = x^*\ a(InN) + (1-x)^*\ a(GaN) \tag{2.3}$$

By combining Eqn. (2.1) and (2.2), the alloy content can be determined from XRD data. Rocking curves (ω- scan) obtained by fixing the detector at twice the Bragg angle (i.e. 2θ) and scanning over ω is a way to probe the crystalline quality. FWHM of rocking curves in different planes are used to measure the degree of crystalline quality.

The XRD system employed for this study is manufactured by Rigaku (RINT2000V/PC series).

It includes a RINT2000V/PC series vertical goniometer and x-ray generator. The goniometer (with radius of 185 mm) can make θ/2θ coupled scan and, θ, 2θ individual scans. The measured 2θ angle range can change from -10° to 158°. Computer controlled variable slits with high precision are used for x-ray analysis. The x-ray source is from a sealed-off Cu x-ray tube. The characteristic wavelengths are $CuK_{\alpha 1}$ = 1.54056 Å and $CuK_{\alpha 2}$ = 1.54439 Å. The XRD peaks from $CuK_{\alpha 2}$ can be eliminated by a software application.

Figure 2.5 is the typical θ/2θ scan curve for InN epilayer grown on GaN templates. As we can see, there is single peak from c-plan diffraction of undoped InN epilayer, indicating the sample is single phase and single crystal. Figure 2.6 shows the ω-rocking curve for symmetric (0002) reflection for undoped InN epilayer grown on GaN template with FWHM of 500 arc sec.

XRD analysis done in this work involves symmetric as well asymmetric Bragg reflections. Symmetric rocking curves have miller indices of h=k=0, [e.g. (002), (004), etc.]. The symmetric scan can only give the information along the c-axis. If there is some change in the a-axis, or the crystal lattice has some twist, one cannot get any information from the symmetric scan. The asymmetric rocking curves have h, k≠ 0. The asymmetric scan, like the scan from (104) plane can reveal more information in the growth plane of crystal.

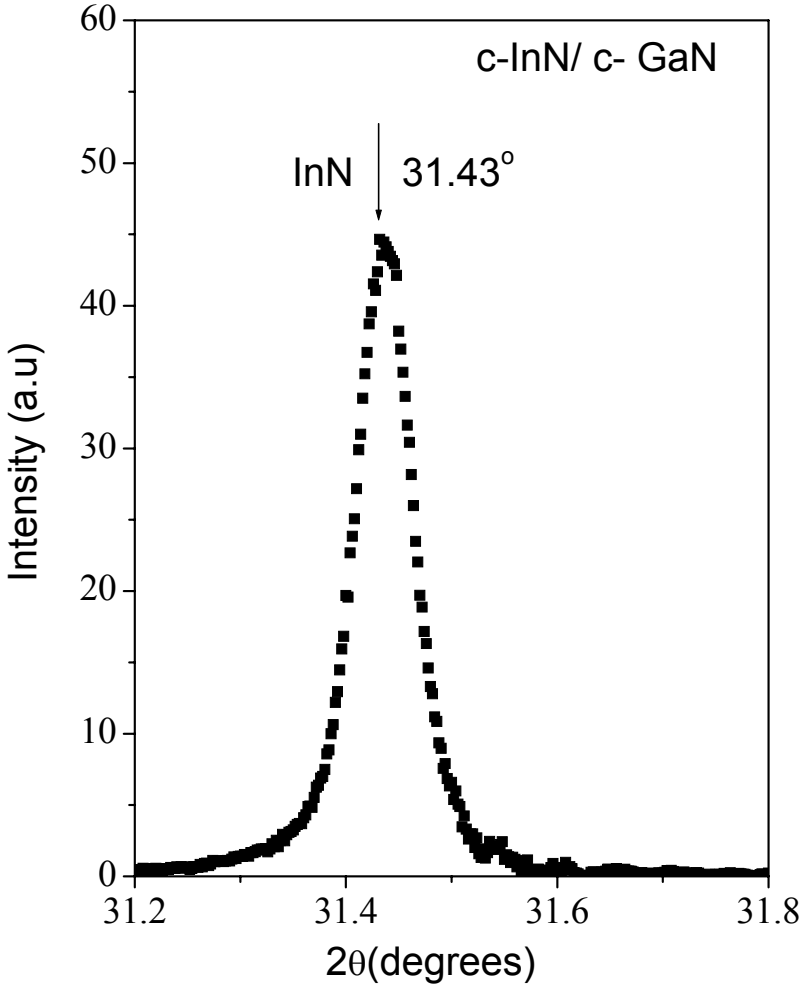

Figure 2.5 θ-2θ scan for typical InN grown on GaN/ Sapphire template

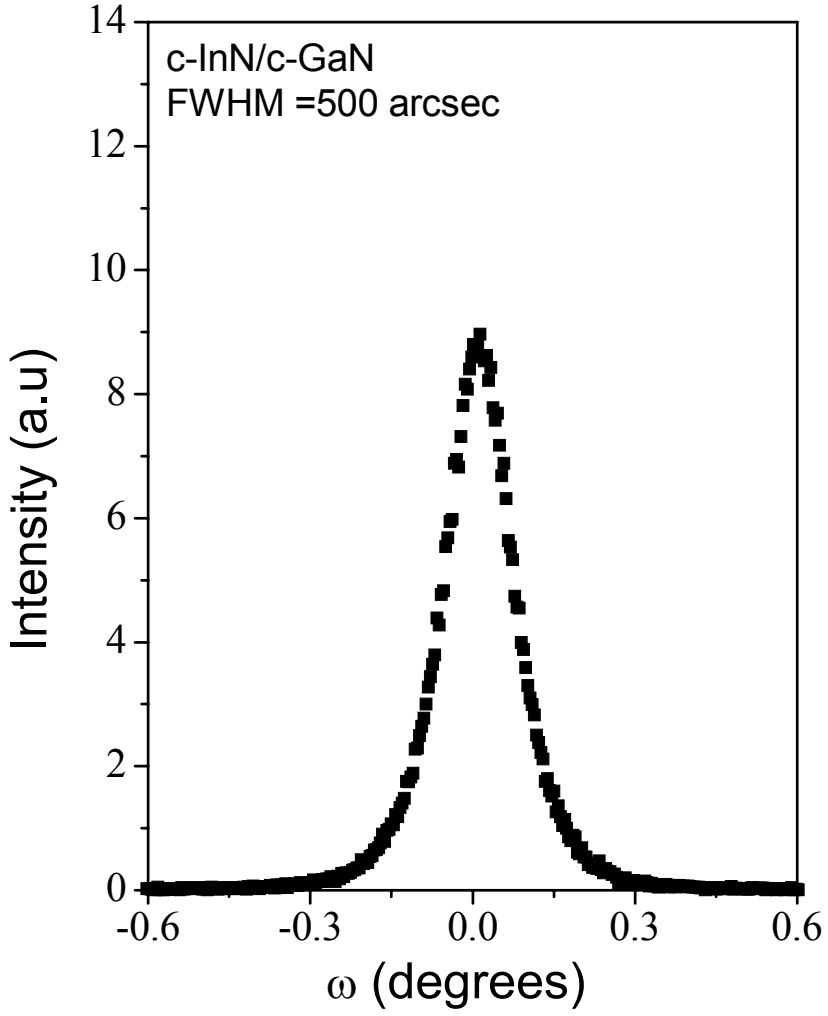

Figure 2.6 ω- scan for typical InN grown on GaN/ Sapphire template

2.2.2 Optical microscope

The optical microscope is one of the characterization tools that requires no sample preparation and uses visible light and system of lenses to magnify the image of epilayers surfaces. Optical microscopy is an important tool used for optimization of III-nitride films growth in this study. Surface morphologies of the as-grown films are often attributed to specific growth process parameters and crystal growers can address these problems by studying the surface studies. Figure 2.7 shows the Nikon eclipse ME 600 microscope used to inspect the surface of as grown samples.

Figure 2.7 Picture of Nikon eclipse ME 600 optical microscope used for this work

2.2.3 Hall Effect measurement

Hall Effect measurement is one of the most commonly used characterization tool to asses the transport properties of a semiconductor such as its carrier concentration, conductivity and mobility. The Van-der pauw configuration is the most common configuration used to study a layered structure where only one layer of known thickness is doped. In this configuration, four ohmic contacts are made on the corners of a square shaped sample. A constant current is applied across two opposite ends of sample and a magnetic field is applied perpendicular to the surface of sample. The electrons or holes producing this current experience a force in the direction which is determined by relation F= q(VxB), where V and B are the carrier velocity (in the direction of current) magnetic field respectively. As a consequence an electric field is established in this direction, which can be determined by measuring the voltage drop at the remaining two ends. This voltage is known as hall voltage. Carrier concentration can be determined using this hall voltage, magnetic field strength and current, which in turn uses to calculate electron or hole mobility. Figure 2.8 shows the picture of Hall Effect measurement set up in our lab.

Our Hall Effect measurement system is schematically illustrated in figure 2.9. Hall Effect switching card (Keithley Model 7065) is the central device in the measurement system which is used to perform the resistivity and hall voltage measurements. This card has a low electromagnetic interference power supply to maximize isolation and minimum noise effects and selectable input characteristics for either high or low resistivity measurements. To minimize the effects of leakage current resistance and capacitance signals from the sample were input into the card through triaxial cables.

A multimeter (Keitheley model 196) was used for measuring the hall voltage. A current source (Keitheley model 220), with ± 0.5 pA to ± 101 mA current range and 10^{14} Ω output resistance, was used to supply a current to the sample, and the current flow through the sample was monitored by a picoammeter (Keithley model 485) with 0.1 pA resolution. The magnetic field was provided by an electromagnet which can be controlled through DIO-2000 controller. The field strength for variable temperature measurement was 0.426 Tesla, and can be as high as 2.5 Tesla at room temperature in the central position where the sample was placed with surfaces perpendicular to the field direction.

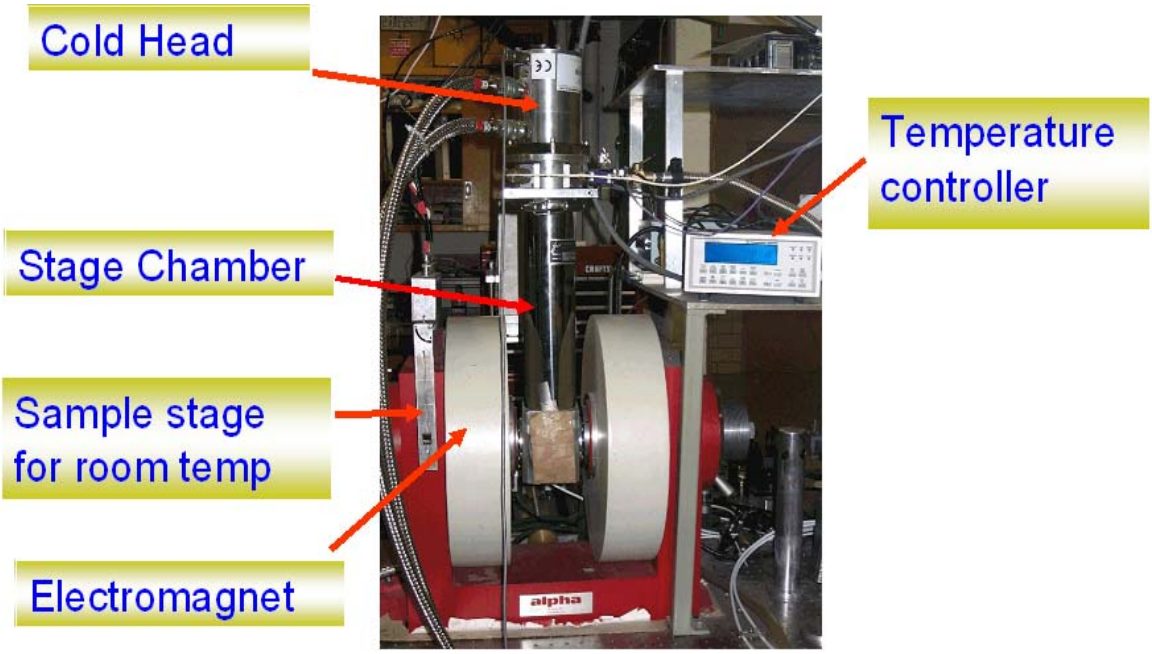

Figure 2.8 Hall-effect measurement setup in our lab

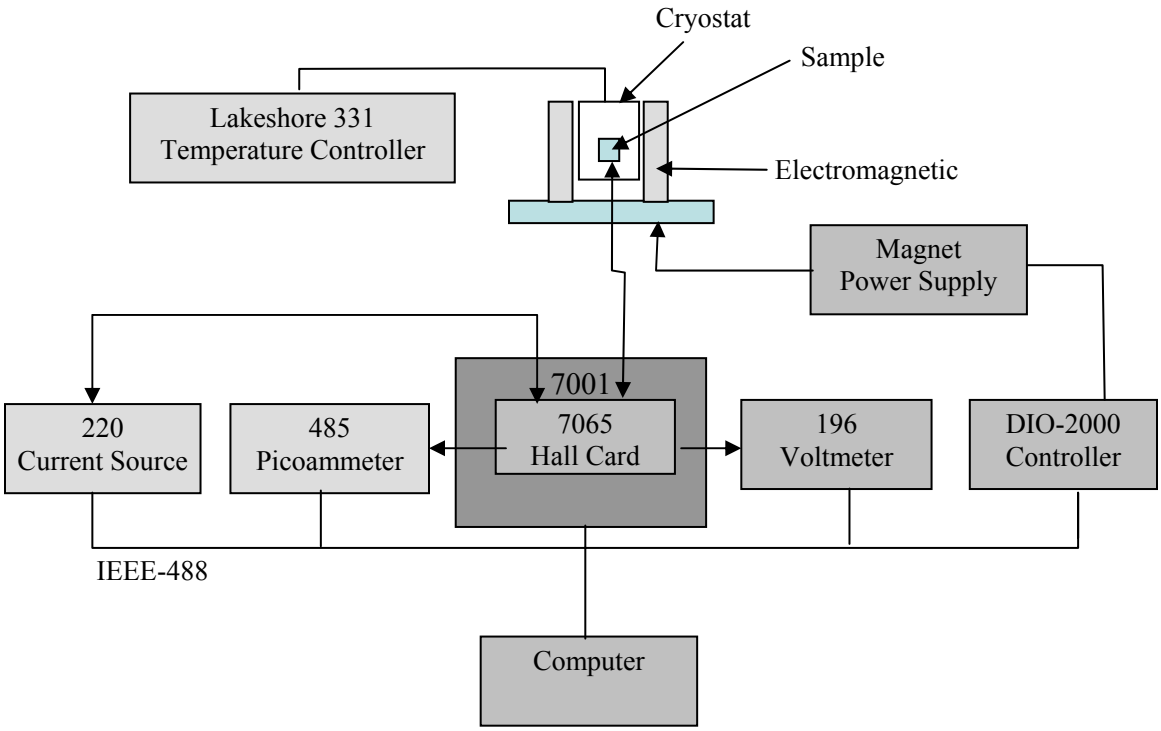

Figure 2.9 Schematic diagram of Hall-effect measurement set up

For temperature dependent Hall measurement, the sample was attached to copper sample holder. The sample holder was then mounted to the cold finger of a closed-cycle He refrigerator (CTI- Cryogenics). The refrigerator can operate at different temperatures ranging from 10 to 900 K. It consists of an air-cooled compressor, two interconnecting pipes, a cold head, and a four window optical chamber, which is specially designed for photo-excited Hall measurements. The cold head has to be pumped to a low pressure (<100 mτ) before turning on the refrigerator. A mechanical pump (Edwards RV3) was used to pump down the cold head to a pressure of 0.015 torr. A semiconductor sensor and a temperature controller (Lakeshore 331) was employed to monitor the sample temperature

2.2.4 Atomic Force Microscopy (AFM)

One of the common instruments to measure surface roughness is the atomic force microscope (AFM). AFM determines the topographic images of the sample by measuring repulsive and attractive forces between tip and the sample with the high vertical (< 1 Å) and lateral (~ 10 Å) resolution. Figure 2.10 shows the photograph of AFM used in this study which was Quesant 250 model manufactured by Quesant Company. The AFM consists of a microscale cantilever with a sharp tip at its end that is used to scan the specimen surface. The cantilever is typically silicon or silicon nitride with a tip radius of curvature on the order of nanometers. In general the tip is made of silicon. The tip must be sharp and thin to get into every nook and corner of the surface and strong enough to survive the forces and shouldn't bend under normal loads.

When the tip is brought into close proximity of a sample surface, forces between the tip and the sample lead to a deflection of the cantilever according to Hooke's law. A laser spot reflected from the top of cantilever into an array of photodiode is used to determine the deflection. This deflection can record the shift of beam, and therefore the movement of the cantilever and tip. The vertical movement of the tip is measured as a voltage change, which then translates to the surface profile.

The AFM can be operated in a number of modes, depending on the application. In general, possible imaging modes are divided into static (also called Contact) modes and a variety of dynamic (or non-contact) modes. Contact mode is suitable for hard surfaces

like III-nitride semiconductors. In the contact mode operation, the static tip deflection is used as a feedback signal. Because the measurement of a static signal is prone to noise and drift, low stiffness cantilevers are used to boost the deflection signal.

In contact mode, the force between the tip and the surface is kept constant during scanning by maintaining a constant deflection. The cantilever is externally oscillated at or close to its fundamental resonance frequency in the non-contact mode. The oscillation amplitude, phase and resonance frequency are modified by interaction forces between tip-sample; these changes in oscillation with respect to the external reference oscillation provide information about the sample's characteristics. Contact mode was employed in this study to measure surface roughness of samples surface.

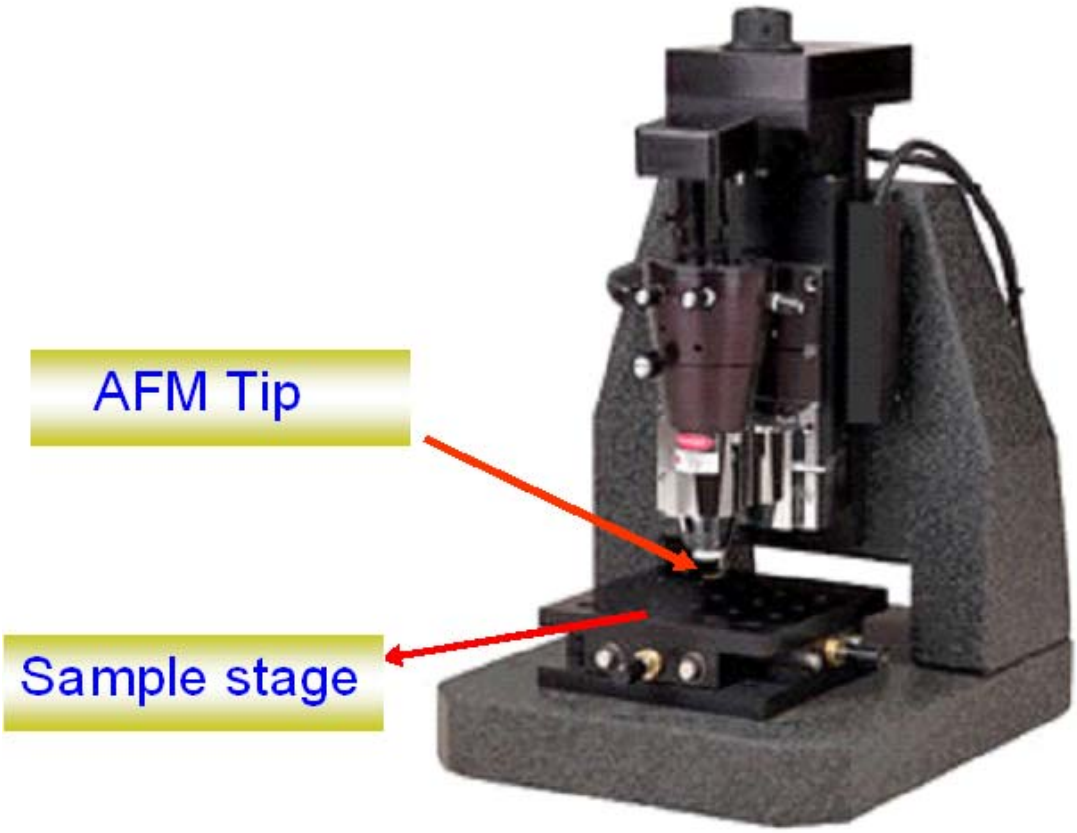

Figure 2.10 AFM (Q-scope 250 model from Quesant Company)

A root mean square (RMS) deviation given by the AFM software contains the information about the surface roughness of the sample. Figure 2.11 shows an image of InN epilayer scanned by AFM with RMS of 22 nm on 10x10 μm^2 scale

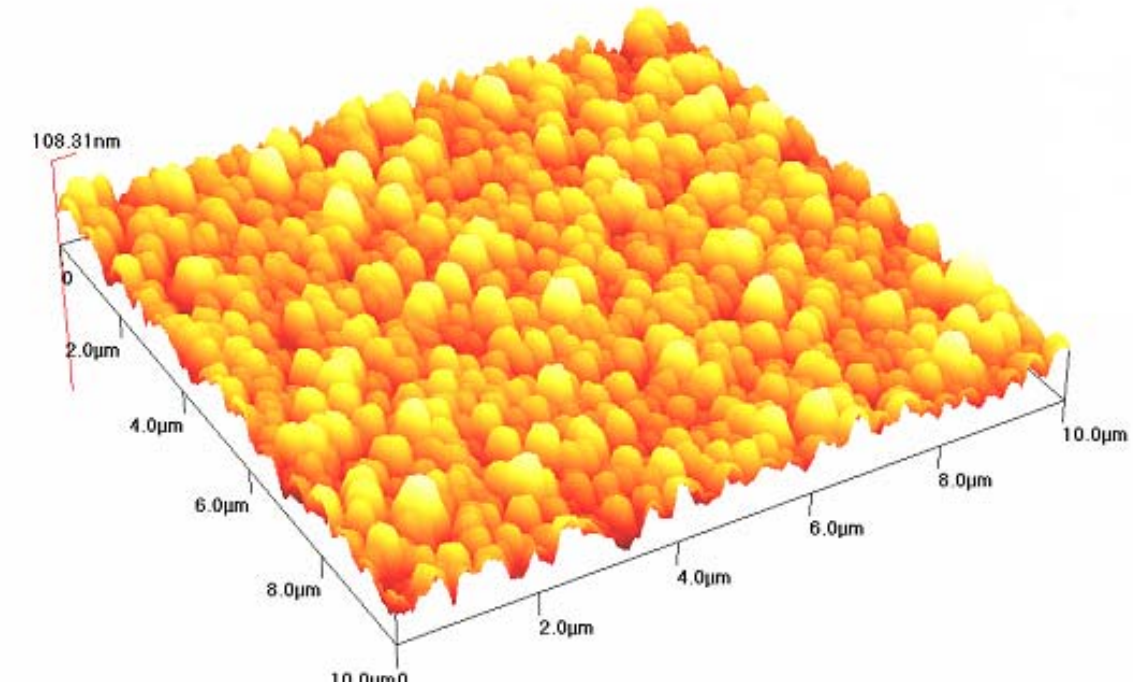

Figure 2.11 AFM image of InN epilayer scanned on 10x10 μm^2 scale

2.2.5 Photoluminescence (PL)

Photoluminescence (PL) spectroscopy is a contact less, nondestructive method of probing the electronic structure of materials. Light is absorbed when directed onto a sample and it transfers excess energy into the material in a process called photo-excitation. Luminescence or emission of light is one way this excess energy can be dissipated by the sample. In the case of photo-excitation, this luminescence is called photoluminescence.

Photo-excitation causes the electrons to move within the material into allowed excited states. When these electrons return to their equilibrium states, the excess energy is released and may emit the light through a radiative process or a nonradiative process. The energy of the emitted light (photoluminescence) relates to the difference in energy levels between the two electron states involved in the transition between the excited state and the equilibrium state. The quantity of the emitted light is related to the relative contribution of the radiative process.

PL spectroscopy is an efficient tool in order to probe the optical transitions in the semiconductor and other materials. Information about both the fundamental optical band edge transition and impurity or defect related transitions of semiconductor can be measured by PL directly and precisely. The experimental set up used for the PL measurement of InN and In-rich InGaN alloys is shown in figure 2.12. The system consists of two solid state lasers: Ti-sapphire laser emitting 780 nm photons with mode locked power around 1.46 watts, which is optically pumped with coherent verdi-10 emitting 10 watt at 532 nm. The excitation laser has a repetition rate of 76 MHz and pulse width of 100 femto-seconds. The IR detection system has a 0.3 m monochromator with the capability to cover the wavelength range from 800 to 1700 nm. InGaAs detector has very good sensitivity in the spectral region around the band gap of InN and In-rich InGaN alloys. The sample is mounted on a stage with a copper cold finger in a closed-cycled helium refrigerator. The PL measurement temperature can be varied anywhere between 10 and 800 K.

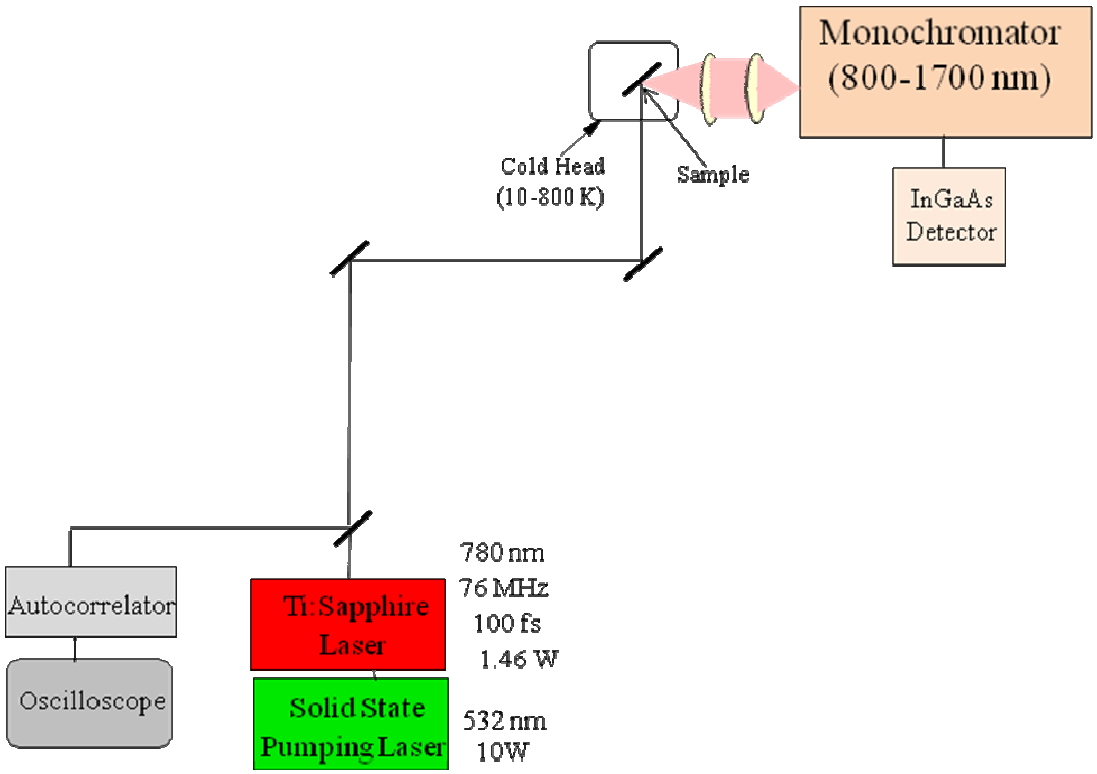

Figure 2.12 The experimental set up used for the PL measurement of InN and In-rich InGaN alloys

2.2.6 Electroluminescence (EL)

EL is an optical process in which a material emits light in response to an electric current passed through it, or to a strong electric field. EL is the result of radiative recombination of electrons and holes at the p-n junction or quantum wells in a semiconductor. The excited electrons release their energy as photons - light. Figure 2.13 shows the actual photograph and of EL set up employed to probe light emitting diodes in this work. A variable bias and current was applied to the devices from a Keithley 2430 source meter. Nikon eclipse ME 600 microscope was used for device positioning and probing at the surface. EL emission to detection system was transferred by an ocean optics USB 2000- mixed bifurcated fiber (200-800 nm) Figure 2.10 (a) shows the EL spectra positioned at 480 nm measured for blue LED.

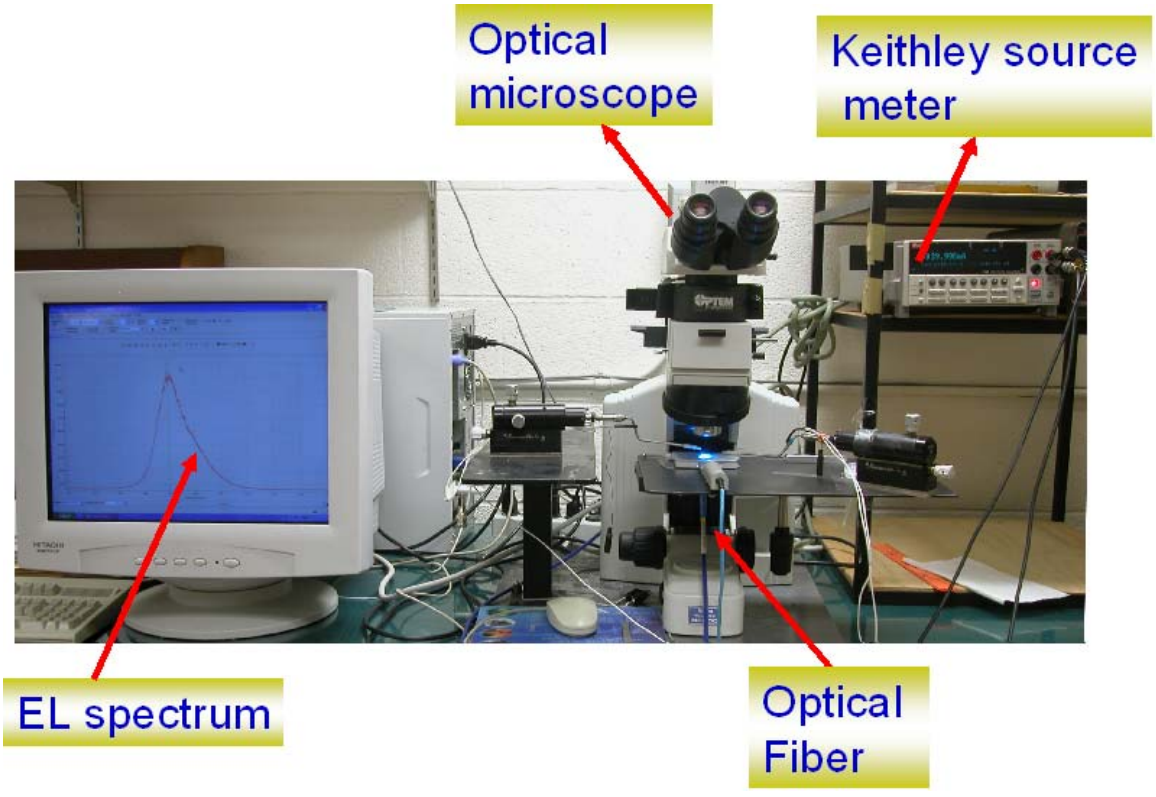

Figure 2.13 The photograph for Electroluminescence set up used to probe light emitting diodes in this work

CHAPTER 3 - Experimental results and discussions

3.1 Growth and Characterization of Ga-rich InGaN alloys

InGaN alloys are widely used as an active media for high brightness III-nitride blue/green light emitting diodes (LEDs) and violet and blue injection laser diodes (LDs). The emission wavelength of InGaN alloys in principle can be tuned from infrared to blue by varying the In content to provide full color emission. If red color emitting InGaN epilayers with high optical qualities can be obtained, it may be possible to achieve all nitride monolithic white LEDs by mixing red, green, and blue emissions from InGaN active layers with different In contents.

The growth of InGaN alloys has proven to be extremely challenging, mainly due to very high equilibrium vapor pressure of nitrogen over InN, a large lattice mismatch (11%) between InN and GaN and low dissociation rate of ammonia at low growth temperature which degrades the crystalline quality. Growth using high temperatures of approximately 800^{o}C typically results in high crystalline quality but the amount of InN in the solid is limited to low values because InN starts to evaporate at high temperatures [61]. Ho and Stringfellow [62] studied the temperature dependence of the binodal and spinodal lines in the InGaN system using a modified valance-force-field model in which lattice was allowed to relax beyond first nearest neighbor. He predicted that at a growth temperature of 800^{o}C, the equilibrium solubility of InN in GaN would be less than 6% as is shown in figure 3.1(a). This low solubility results in the miscibility gap that covers almost entire composition range in InGaN. However at low temperatures, indium droplets may form, which acts as sink for InN and prevent the growth of InGaN alloys with high In content [63, 64]. Furthermore, at low temperatures the crystalline quality of the film is inferior at due to poor surface mobility of the ad-atoms, resulting in the three-dimensional growth. In addition, InGaN alloys suffer from phase separation because of the strain produced by large lattice mismatch (due to very different tetrahedral radii) between InN and GaN. Nevertheless Karpov's [65] calculations showed that phase separation can be considerably suppressed if the strain produced during the epitaxial growth from underneath layer is taken into account as is shown in figure 3.1(b).

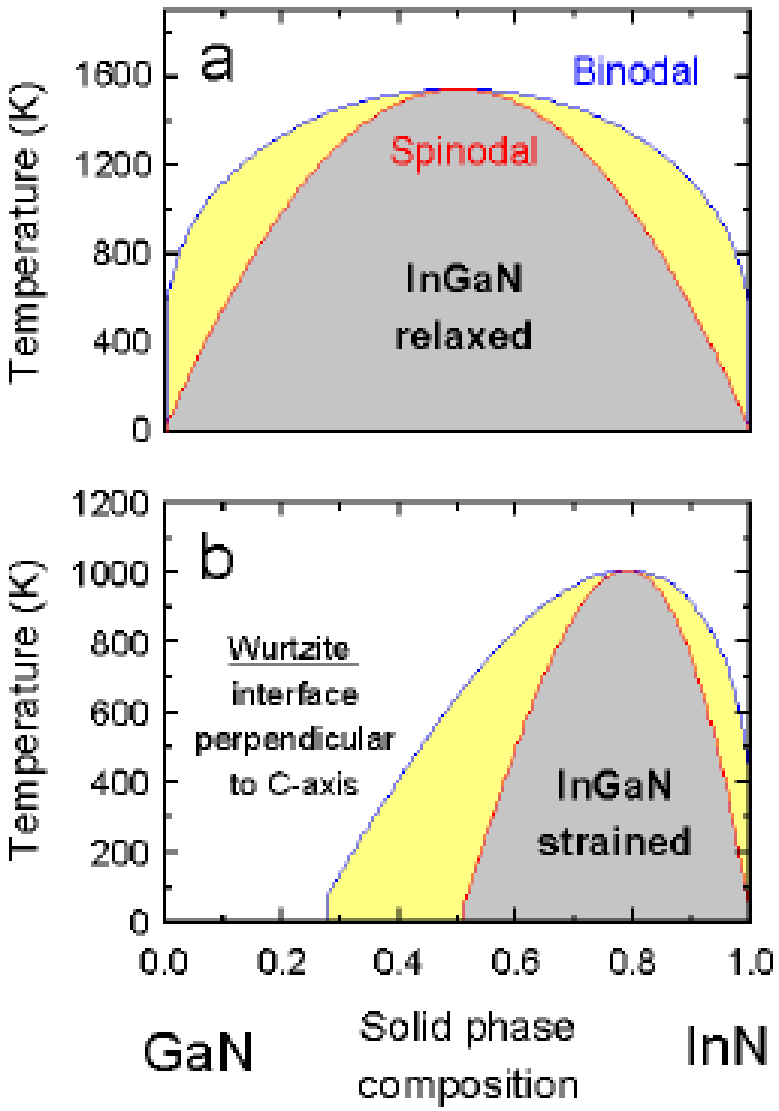

Figure 3.1 Temperature and In content (x) diagram for (a) relaxed relaxed [62] (b) strained $In_xGa_{1-x}N$ alloy[65]. Solid and dotted curves represent binodal and spinodal limits

He calculated much less critical temperature and increased solubility in the strained InGaN alloys that was 35% at 750^{o}C. Based on XRD and optical absorption studies, Singh and co-workers [66-68] provided strong evidence of phase separation in InGaN thick films grown by MBE. Other researchers reported phase separation in InGaN films grown by MOCVD [43, 69].

In this chapter, we summarize our studies of the growth, crystalline quality and PL properties of Ga- rich InGaN epilayers. Single phase was observed up to 37% In content in Ga-rich InGaN alloys. For In content ≥ 0.4, XRD showed phase separation. There was always one main peak from XRD for (0002) θ-2θ-scan showing one phase from 40 % In content with other phases at different peak positions.

The $In_xGa_{1-x}N$ epilayers of about 30- 150 nm thickness were grown on top of 1.0 μm GaN epilayers by MOCVD. Prior to the GaN growth, a 20 nm thick GaN buffer layer was grown on c-plane sapphire at 550^{o}C. Subsequent growth was carried out at 1050^{o}C for GaN and (630-800)^{o}C for $In_xGa_{1-x}N$. TMGa and TMIn were used as precursors. Nitrogen and hydrogen were used as carrier gases for InGaN and GaN, respectively.

In content in $In_xGa_{1-x}N$ was varied by varying the In flow rate or the growth temperature (T_g). The growth rate of GaN and $In_xGa_{1-x}N$ were 2.6 μm/hr and (0.03-0.2) μm/hr respectively. In content in InGaN epilayers was estimated from peak value of XRD curves of (0002) plane in θ-2θ scan and applying Vegard's law. The thickness of the films was estimated from in-situ interference measurements during the epi-growth. The optical properties of $In_xGa_{1-x}N$ alloys were characterized by PL measurments. The PL spectroscopy system used consists of a frequency tripled 100 femtosecond Ti:sapphire laser with an excitation wavelength set at 266 nm with 40 mW average power and 76 MHz repetition rate.

Figure 3.2 (a) and (b) shows the variation of Indium content and full width at half maximum (FWHM) of (0002) XRD rocking curve for InGaN epilayers grown under different growth temperature (T_g) respectively. The T_g was decreased from 800^{o}C to 720^{o}C while In and Ga flow rates remained constant.

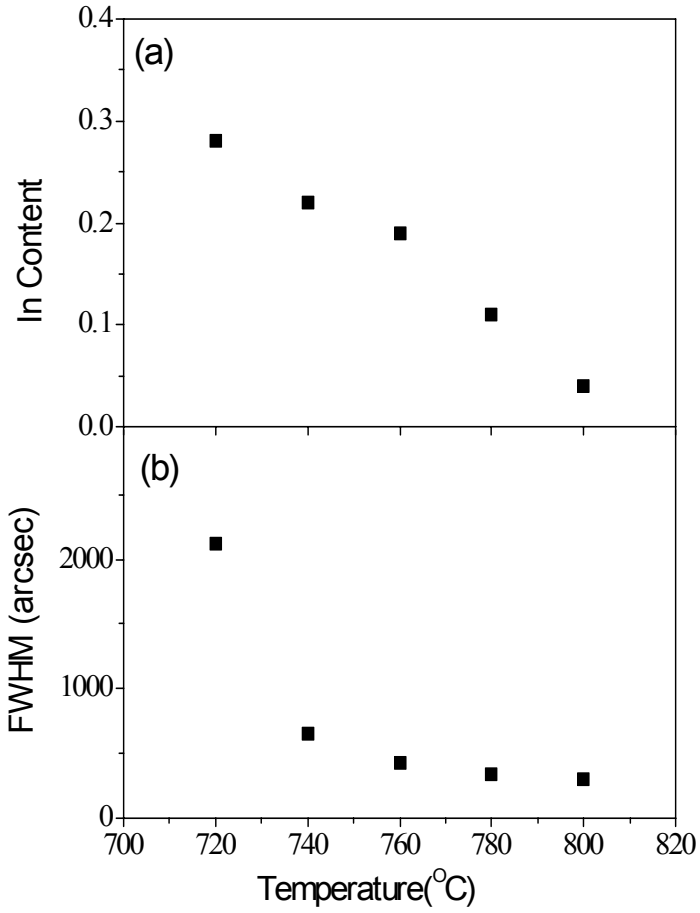

Figure 3.2 (a) Indium content variation with temperature for InGaN epilayers (b) FWHM from (0002) XRD rocking curve.

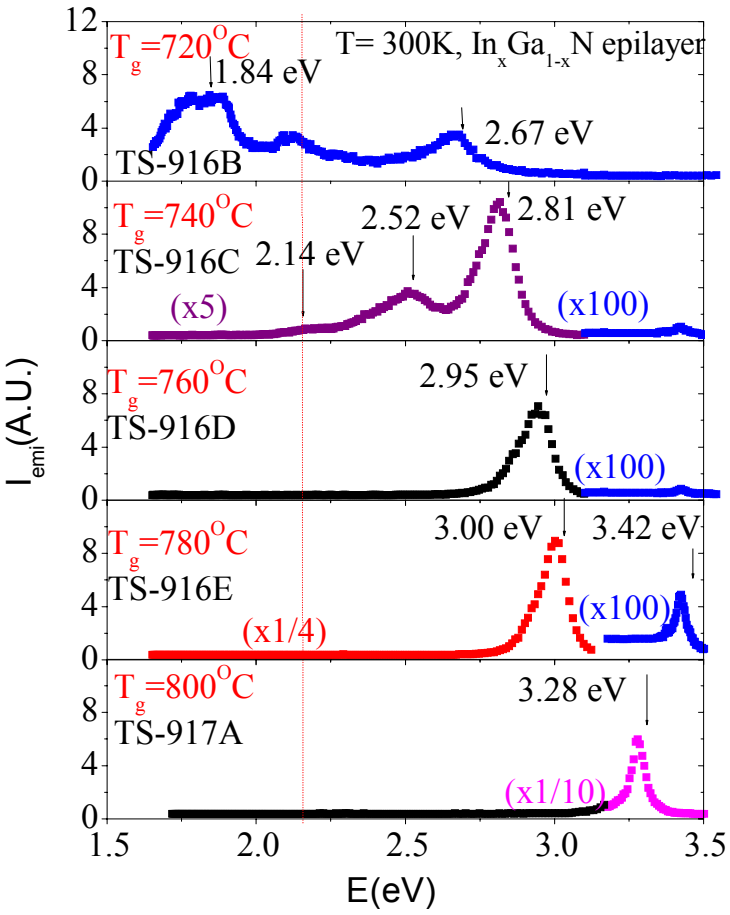

Figure 3.3 Room temperature PL spectra of InGaN epilayers as a function of T_g

As depicted in figure 3.2 (a) indium content in the epilayer increases with the decrease of temperature indicating the evaporation of InN at high temperature because of high volatility of nitrogen over InN. Almost linear relation between T_g and the amount of In- corporation ease us to engineer the InGaN/GaN heterostructure for device applications. The FWHM for InGaN epilayers increases with the decrease of T_g as is shown in figure 3.2 (b). Thus the indium content increases at the expense of reduced crystalline quality.

Figure 3.3 shows the PL spectra of InGaN epilayers grown as a function of T_g. When T_g was decreased from 800^{o}C to 720^{o}C, the PL peak position shows a shift from 3.28 eV to 2.67 eV. The Indium composition in InGaN epilayers decreases with increase of T_g, which gives rise to wavelength tunability in this set of epilayers. At low temperatures of 720^{o}C and 740^{o}C some impurity peaks were also observed along with band edge peaks, which disappear at $T_g > 740^o$C. Also the PL intensity increases at high temperatures which shows the improvement in optical quality, and is consistent with the XRD rocking curve results.

Figure 3.4. (a) shows the (0002), θ-2θ, XRD scans for InGaN films grown at 670^{o}C with 37% In content and (b) at 630^{o}C with 40 % In content. All samples grown with indium composition ≤ 37% showed single crystal diffraction peaks by θ-2θ XRD scan. Single peak from θ-2θ XRD scan indicates the films were single phase. Samples grown with 40% In content showed the diffraction peak for this main In composition along with extra peaks. These extra peaks corresponds to 65% and 58 % In content as is shown in figure 3.4. (b). The observed phase separation is evidently driven by strain due to the mixing of the two lattice mismatched components of the InGaN alloy system. Indium atoms are excluded from the InGaN lattice to form an alloy of a different composition and reduce the strain energy of the system.

InGaN epilayers with 37% In content showed higher XRD intensity and lower line width from rocking curve as compared to 40 % In content. This decrease in intensity for phase separated InGaN epilayer was also evident from PL spectra for these epilayers. Figure 3.5 (a) and (b) shows the room temperature PL spectra for 37 % In content and 40 % In content respectively.

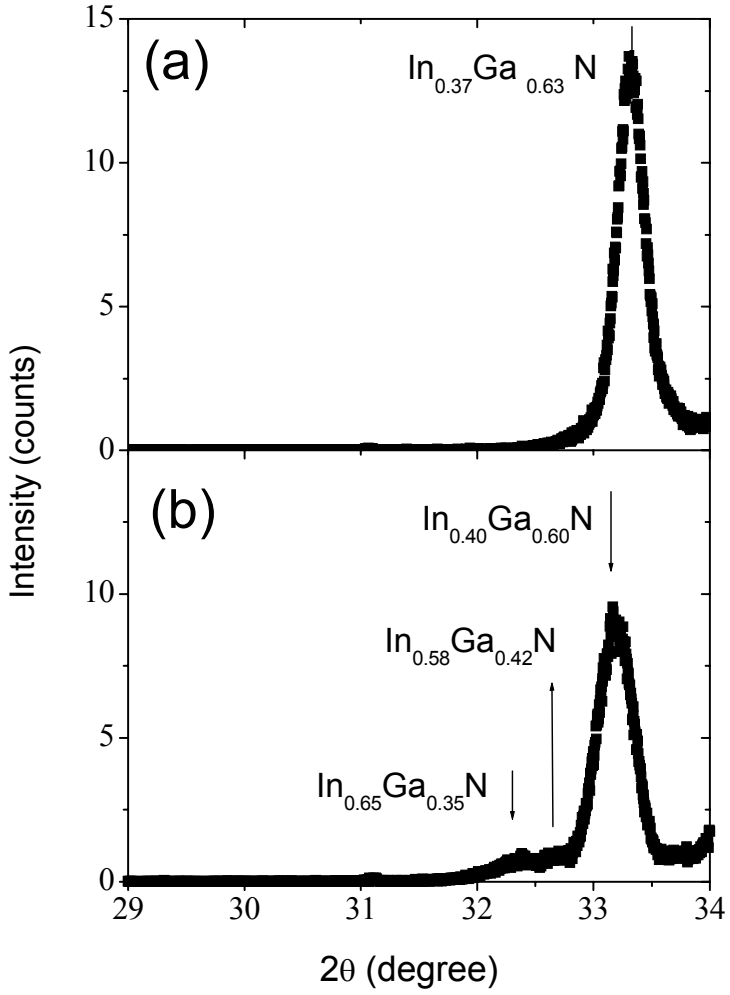

Figure 3.4 (a) (0002) θ-2θ, XRD scan for InGaN films with 37% In content and (b) 40% In content

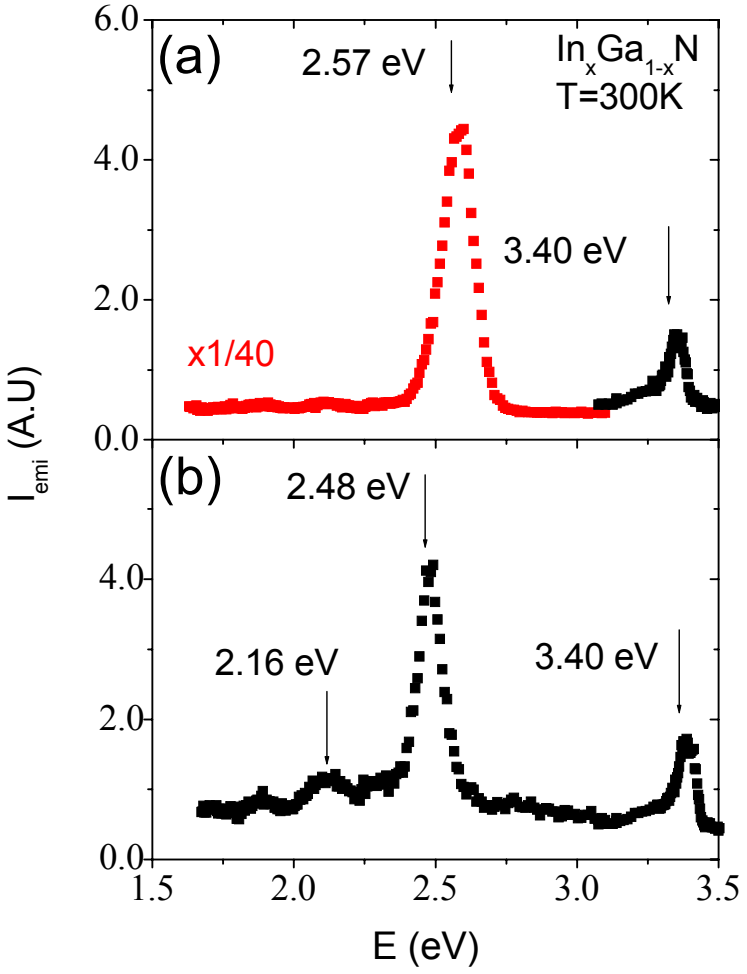

Figure 3.5 (a) PL spectra for InGaN films with 37% In content and (b) 40% In content

PL peak position showed a shift from 2.57 eV to 2.48 eV and intensity decreased by a factor 40 as the In content was increased from 37% to 40 %. This shift indicates the wavelength tunability. Peak at 3.40 eV from PL spectra represents the GaN peak position and 2.16 eV from figure 3.5 (b) could be from underneath GaN template.

Ga-rich $In_xGa_{1-x}N$ ($x \leq 0.4$) epilayers were grown on sapphire substrates by MOCVD and were characterized by XRD and photoluminescence PL. The indium concentration was found to be sensitive to growth temperature. As growth temperature was increased from 720 to 800^oC, the indium content decreased linearly from 27% to 5%. XRD measurements showed InGaN films with an Indium incorporation of 37% with single phase, phase separation occurred for $x \geq 40\%$. To understand the issue of phase separation in Ga-rich InGaN, studies on the growth of pure InN and In-rich $In_xGa_{1-x}N$ alloys were carried out.

3.2 High mobility InN epilayers grown on AlN epilayer templates

Among III-nitrides, InN has the narrowest direct band gap, the smallest electron effective mass, the highest mobility and drift velocity [70, 71]. These distinctive properties make InN an interesting material for applications in full color displays and high frequency/high speed/high power electronic devices such as high electron mobility transistors (HEMTS) [72, 73]. When alloyed with GaN, the energy band gap of InGaN can be tuned to cover the entire solar spectral region [29], which makes InGaN alloys highly promising for high efficiency multijunction solar cell applications. InGaN alloys could be potentially important thermoelectric materials for directly converting waste heat energy to electricity [74]. In addition, the significant lattice mismatch between InN and GaN or AlN can give rise to large piezoelectric charge, which may be advantageous for HEMT applications [75].

As grown unintentionally doped InN epilayers generally exhibit *n*-type conductivity, with unintentional free electron concentrations as high as $10^{21}cm^{-3}$ [34]. Theoretical calculations as well as experimental results give conflicting views regarding the major reason behind such high n-type conductivity. Oxygen and hydrogen impurities are proposed as the potential causes of the unintentional *n*-type conductivity in as-grown InN [46-48]. On the hand, the presence of nitrogen vacancies due to insufficient thermal decomposition of NH_3 at low growth temperatures (~ 500^oC) has also been suggested as another major reason for the high background electron concentration in InN epilayers grown by MOCVD [34, 76]. More recently, it is widely accepted that InN films possess a surface electron accumulation layer due the pinning of Fermi level at about 0.8 eV above the conduction band minimum due to intrinsic surface states [22, 53, 54]. In general, due to the much lower dissociation temperature of InN than GaN, it has been exceedingly difficult to grown InN epilayers with high quality by using MOCVD method. As of today, InN epilayers with highest material qualities are produced by molecular beam epitaxy (MBE) [77, 78]. The highest room temperature electron mobility reported for MOCVD grown InN was about 1100 cm^2/Vs with an electron concentration $\geq 10^{19}$ cm^{-3} with the use of GaN/sapphire templates[79, 80] and it was found to be challenging to simultaneously enhance the electron mobility while reducing the background electron concentration [79].

From practical point of view, there is a great need to develop and understand the growth processes to produce InN films with improved quality by MOCVD, which is currently the primary technique for producing all the commercial available III- nitride devices.

In this section of chapter, we discuss the MOCVD growth, transport and optical property studies of *c*-plane InN epilayers on *c*-plane AlN epilayer templates. There have not been many reports for InN epilayers grown on AlN templates, although it was pointed out that InN/AlN hetrojunction structure may provide a platform for future InN device applications due to its potentially excellent structural and electronic properties as a consequence of the large band gap difference between InN and AlN [81]. Compared to InN epilayers grown on GaN/sapphire templates, the use of AlN/sapphire templates facilitates a straightforward electrical property characterization by conventional techniques such as Hall Effect measurement due to the insulating nature of AlN. Furthermore, we found that the use of AlN templates allows InN to be grown at higher temperatures than in case of GaN templates, which enhanced the supply of nitrogen atoms from NH_3 at higher growth temperatures.

The 0.8 μm thick undoped InN epilayers were grown in a custom built MOCVD on AlN-or GaN-epilayer/sapphire (0001) templates. More details on the growth conditions and structural properties of AlN/sapphire templates can be found in our previous publications [82, 83]. TMIn, TMAl and NH_3 were used as In, Al, and N sources, respectively. N_2 was used as a carrier gas for InN epilayer growth. The optimal growth temperature (T_G) for InN epilayers deposited on GaN templates (InN/GaN) was 510^{o}C, and InN films decomposed (or evaporated) as T_G was raised to above 510^{o}C. By varying the growth conditions, the highest electron mobility (μ) of InN/GaN we attain was ~1000cm^2/Vs with an electron concentration (n) of ~1.2x10^{19} cm^{-3}. In contrast, the highest T_G employed for InN epilayers deposited on AlN templates (InN/AlN) was ~570^{o}C, above which evaporation of InN starts to occur.

Figure 3.6 (a) and (b) shows the sample structure for undoped InN epilayers grown on AlN/Al_2O_3 and GaN/Al_2O_3 templates respectively.

Figure 3.6 Sample structure for undoped InN epilayers grown on (a) AlN/Al_2O_3 and (b) GaN/Al_2O_3 templates.

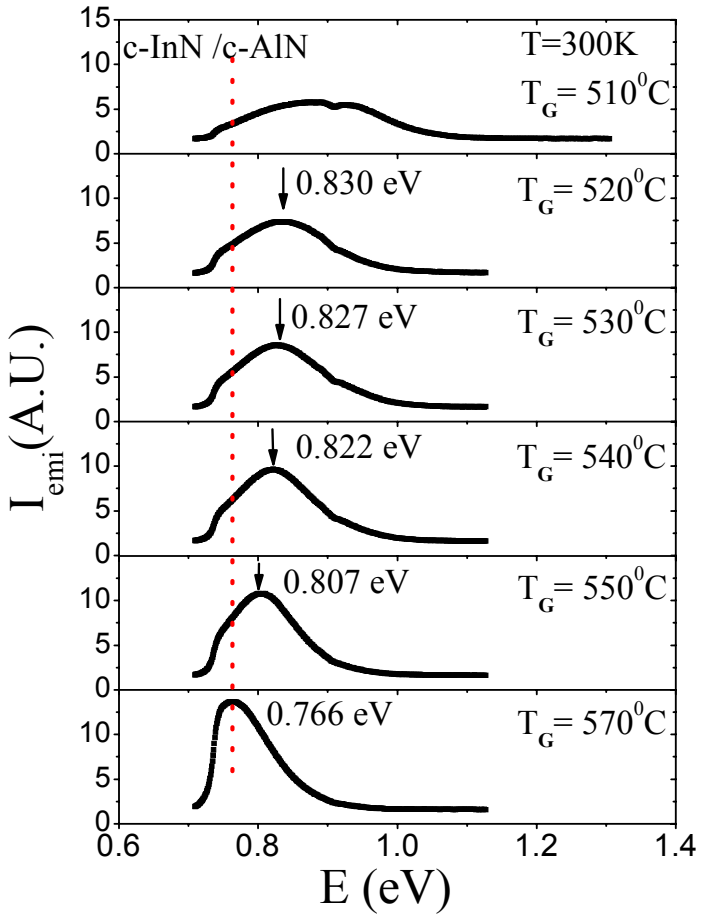

Figure 3.7 300 K PL spectra of undoped InN epilayers grown on AlN templates (c-InN/c-AlN). The growth temperature (T_G) was varied from 510 to 570 ^{o}C.

Figure 3.7 shows the PL spectra of undoped InN epilayers grown on AlN templates (InN/AlN) when T_G was increased from 510 to 570^{o}C. The band-to-band PL emission peak shifted from 0.87 eV to 0.76 eV as T_G was increased from 510^{o}C to 570^{o}C.

Figure 3.8 summarizes the effects of T_G on the electrical and optical properties [integrated PL emission intensity (I_{emi}), PL emission peak position (E_p), background electron concentration (n) and mobility (μ)] of InN epilayers grown on AlN templates. Figure 3.8 (a) and (b) show that I_{emi} increases while E_p decreases as T_G was raised from 510 to 570^o C. Depicted in Fig. 3.8 (c) and (d) are the plots of n and μ versus T_G. A decrease in n from 3.1 to 1.1 x 10^{19} cm^{-3} and increase in μ from 690 to 1000 cm^2/Vs was observed as T_G was increased from 510 to 570^o C. These results are believed to be associated with an enhanced decomposition rate of NH_3 at higher T_G.

An enhanced decomposition of NH_3 is likely to reduce the nitrogen vacancies and henceforth a decrease in the background electron concentration and increase in mobility[51, 84]. This observed decrease in n is consistent with the PL results shown in Fig. 3.7 and 3.8 (a), where a red shift of E_p with T_G is clearly illustrated, attributing to a reduced Burstein-Moss blue shift due to a reduction in n [85-87]. This attainment of higher growth temperature for the InN/AlN system may be related to the fact that the initial surface conditions for MOCVD growth are different from those of the InN/GaN system, but a further understanding concerning the exact mechanisms is needed.

The x-ray diffraction (XRD) θ-2θ scan results for InN epilayers grown on AlN templates are shown in Fig.3.9. As illustrated in Fig. 3.9 (a), $(\theta$-$2\theta)$ peak position for InN decreases from 31.41° to 31.33° as T_G increases from 510 to 570^{o}C. The InN lattice constant c, c(InN) deduced from InN (0002) peak position is shown in Fig. 3.9 (b), which shows that c(InN) increases from 5.690 to 5.705 Å as T_G increases from 510 to 570^{o}C. The measured value of c(InN) grown at 570^{o}C agrees well with a previously determined value of 5.704 Å [88, 89]. We also note that the lattice constant c(InN) grown on AlN template at 570^{o}C is the same as that of InN grown on GaN template at 510^{o}C. The observed increase in c(InN) is related to an increase in compressive strain with increasing T_G. Concomitantly, InN lattice constant a, a(InN) is decreased with increasing T_G to compensate with the lattice constant of a(AlN). The full width at half maximum of the rocking curve of the (0002) peak of InN/AlN ranges from 700 – 1000 arcsec.

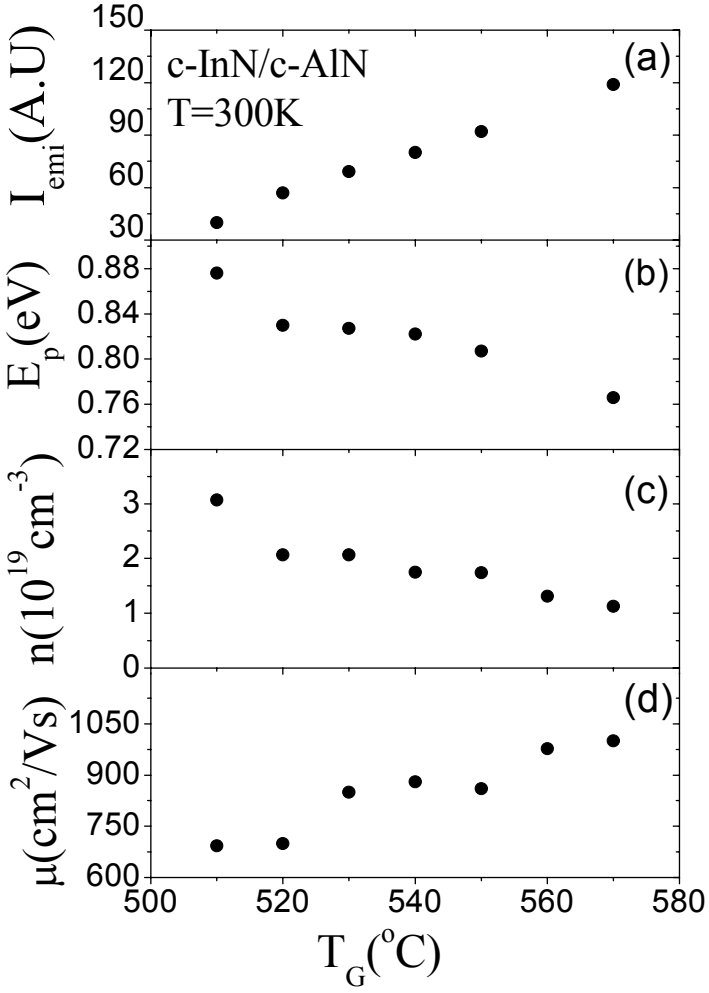

Figure 3.8 Variations of (a) I_{emi}, (b) E_p, (c) n, and (d) μ of undoped InN grown on AlN template with the growth temperature (T_G).

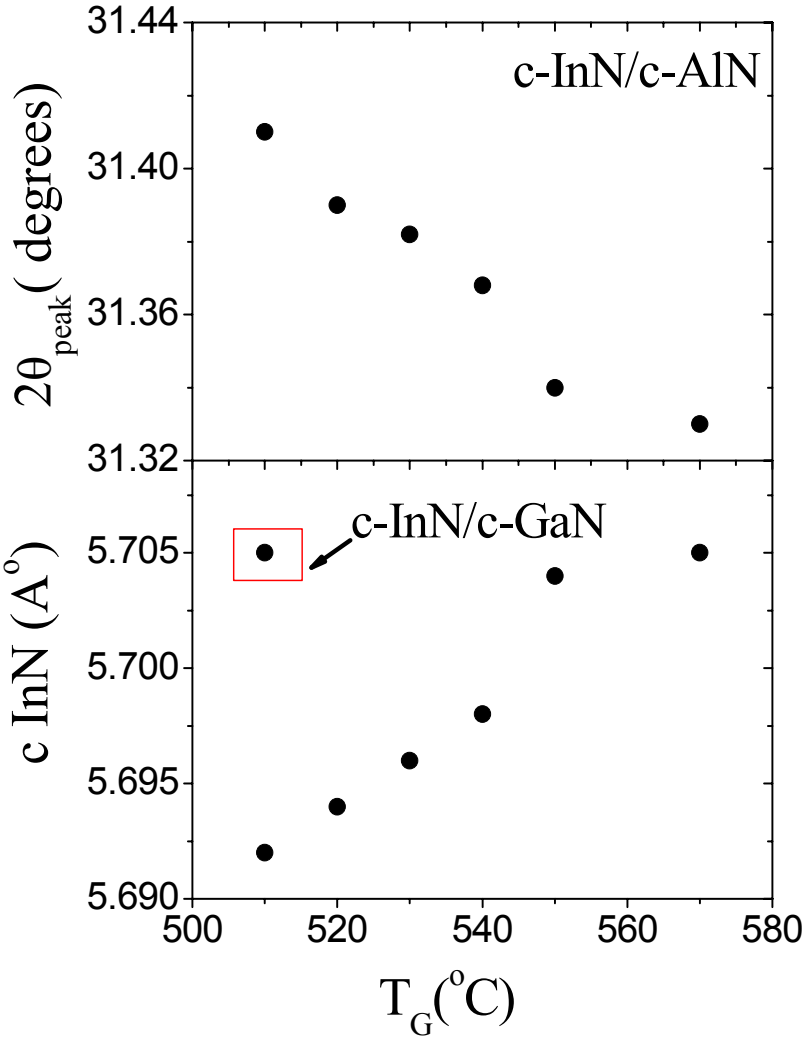

Figure 3.9 Variations of (a) XRD (θ-2θ) scan peak position (b) calculated lattice constant *c*(InN) of undoped InN grown on AlN template with the growth temperature (T_G). Lattice constant *c* of InN grown on GaN template at 510 °C is also shown for comparison.

Further enhancement in the electrical properties of InN/AlN was obtained by increasing the V/III ratio during the growth. Figure 3.10 shows the dependence of n and μ of InN on the V/III ratio for layers grown at 570°C. n decreases from 1.1 x 10^{19} to 6 x10^{18} cm^{-3} and μ increases from ~1000 to ~1400 cm^2/ Vs as the V/III ratio is increased from 1.3 x10^4 to 4.3 x 10^4. This is the highest electron mobility ever reported for InN epilayers grown by MOCVD. The band-to-band emission peak position in samples with n = (6-7) x10^{18} cm^{-3} and μ = (1350-1400) cm^2/Vs is further reduced to ~0.75 eV. Intuitively, the results shown in Fig. 3.10 seem to suggest that the reduction of n is associated with a decrease in nitrogen vacancies. However, the V/III may also impact the incorporation of other unintentional impurities, such as hydrogen and oxygen.

A comparison for growth and characterization of InN on AlN and GaN templates is made in table 3.1. That shows improved electrical and optical properties for InN epilayers grown on AlN templates as compared to on GaN templates. Approaches for stress managements such as incorporation of intermediate strain relieve layers are still needed to improve the crystalline quality of InN

In summary the electrical and optical properties of InN epilayer deposited on AlN templates have been studied as functions of the MOCVD growth temperature and V/III ratio. A room temperature Hall mobility of 1400 cm^2/Vs with a carrier concentration of 7x$10^{18}$$cm^{-3}$ was achieved, which represents the highest electron mobility value reported for MOCVD grown InN epilayers. The results suggested that the use of AlN templates could open up a new avenue for obtaining InN with reduced background electron concentrations and enhanced mobilities.

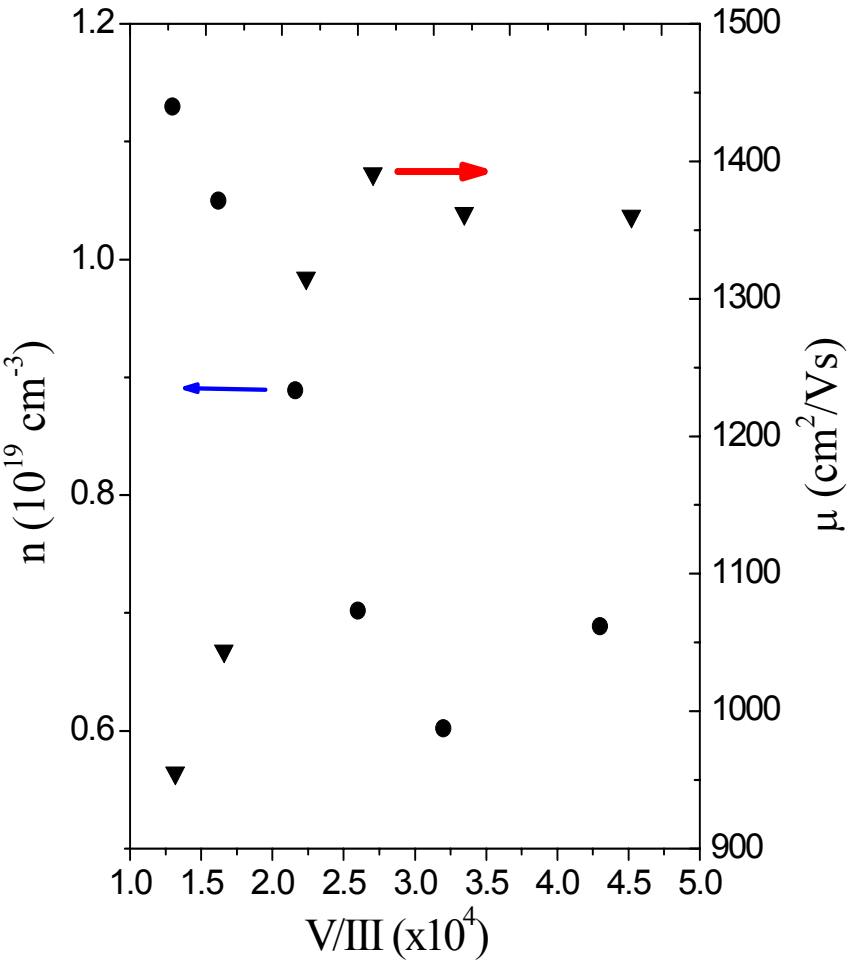

Figure 3.10 Free electron concentration (n) and mobility (μ) of undoped InN grown on AlN template as a function of the V/III ratio with a growth temperature of 570^{o}C. Indium flow rate was changed from 200 to 60 ml/min which corresponds to a V/III ratio variation from 1.3 x10^{4} to 4.3 x 10^{4}.

Table 3.1 Comparison of growth and characterization of InN epilayers grown on GaN and AlN templates

	InN/GaN template	InN/ AlN template
Growth Temperature	510^{o}C	570^{o}C
Hall effect measurement	μ = 1000 cm^{2}/ Vs n=1.21 x10^{19} cm^{-3}	μ = 1400 cm^{2}/ Vs n=7 x10^{18} cm^{-3}
PL spectra E (eV)	0.78 eV	0. 75 eV
XRD rocking curve	400- 550 arcsec	860-1000 arcsec

3.3 Growth and characterization of In-rich InGaN alloys

Group III-nitrides including GaN, AlN, InN and their related alloys are important materials for optoelectronic devices. $Al_xGa_{1-x}N$, GaN and Ga-rich $In_xGa_{1-x}N$ have been intensively studied for optical devices covering wide spectrum range from near-ultraviolet to green region. On the other hand, In-rich $In_xGa_{1-x}N$ has been attracting much attention since the year 2002, when several groups began to report that the band gap of InN is ~ 0.7 eV [26, 29, 89] rather than the previously accepted value of 1.9 eV [61, 90]. By this new finding the potential application fields of $In_xGa_{1-x}N$ were extended to longer wavelength region. Especially, In- rich $In_xGa_{1-x}N$ is considered to be promising material for high efficiency solar cells, covering most useful part of solar spectrum and temperature sensitive laser diodes for optical communications. $In_xGa_{1-x}N$ alloys with energies from 0.7 to 3.4 eV, can be tuned from ultraviolet to near infrared region by varying the In content. Figure 1.3 shows the band gap energy verses Ga content in $In_{1-x}Ga_xN$ alloys which covers almost the whole solar spectrum range. One can get the useful part of solar spectrum by varying Ga content between 0 and 0.63 in the $In_{1-x}Ga_xN$ alloys, which varies band gap energies from 0.7 to 2.4 eV. Figure also shows the band gap energies of currently used materials for high efficiency multijunction (MJ) solar cell such as Ge (0.66 eV), GaAs (1.43 eV) and GaInP (1.9 eV). The deposition process of currently high efficiency MJ solar cells require number of different precursor streams such as Al, In, Ga, As and P and up to 20 different layers including the tunnel junctions. Thus it is potentially attractive to design the MJ solar cells using single ternary alloy system of InGaN, as it provides the flexibility of choosing the number and band gap energies of the constituent junctions. Furthermore, InGaN alloys have great potential for use in solar cells for space applications as they offer a higher degree of resistance to radiation damage [29,35].

In-rich $In_xGa_{1-x}N$ alloys are also promising for high speed electronic devices possibly employing InN channel layer. These serious interests in In-rich $In_xGa_{1-x}N$ have arisen from the recent improvement of InN quality and the bandgap-energy re-evaluation of ~ 0.7 eV instead of 1.9 eV. In-rich $In_xGa_{1-x}N$ alloys have been less studied than InN, which is the least studied of the group III-nitride binary compounds.

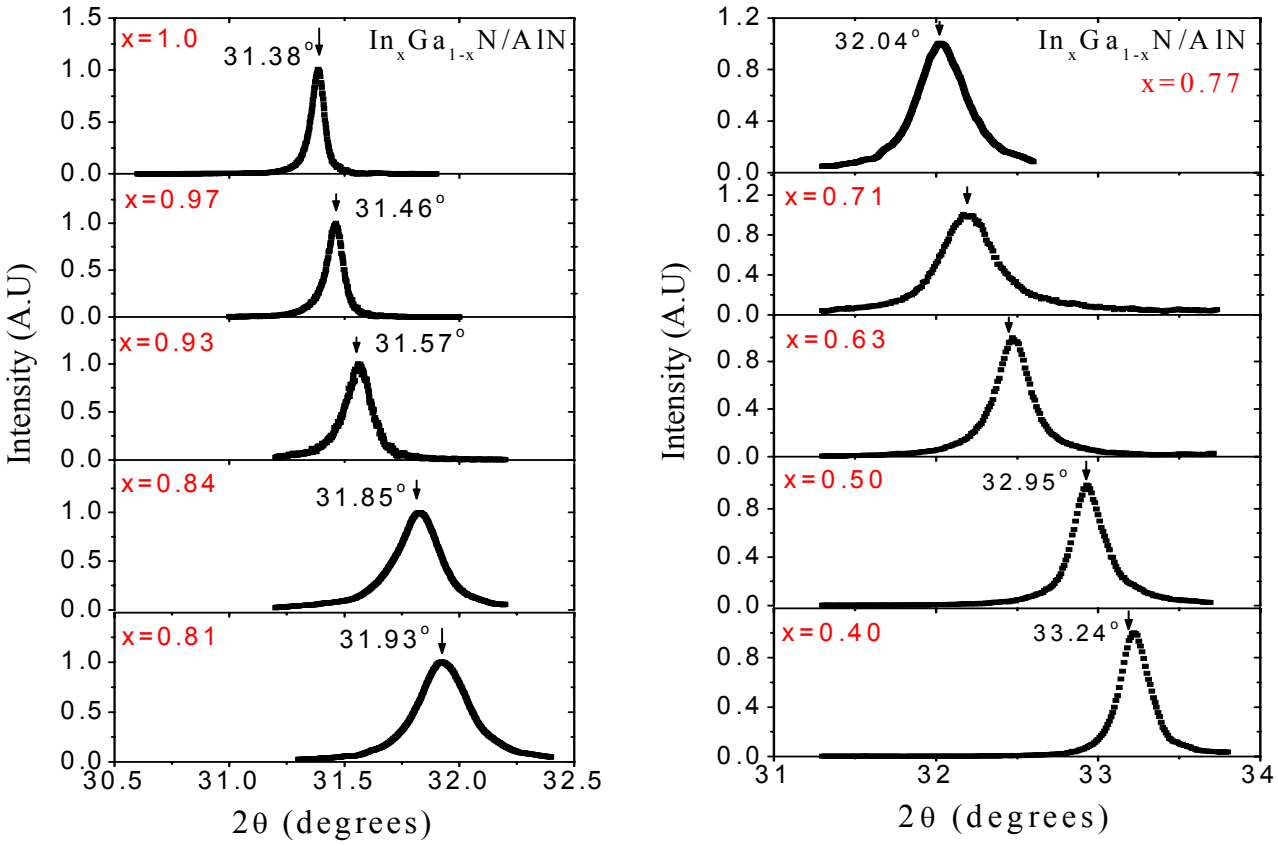

Figure 3.11 (θ-2θ), XRD curves of $In_xGa_{1-x}N$ films, x for (1) to (10) are 1.0, 0.97, 0.93, 0.84, 0.81, 0.77, 0.71, 0.63, 0.50, 0.40 respectively.

The phase separation of InGaN near the GaN side makes it difficult to grow InGaN with high In content for the optical devices [67]. This difficulty could be addressed by studying pure InN and In-rich InGaN for an understanding of the phase separation issue. Furthermore, the study of In-rich InGaN also provides valuable information about the bandgap energy of these materials.

Many previous experimental studies have shown that the growth of high quality In-rich $In_xGa_{1-x}N$ is extremely challenging and their properties are still not fully understood due to phase separation issue, lack of suitable substrate and low dissociation temperature of InN. Few groups reported the growth of In-rich $In_xGa_{1-x}N$ with entire alloy composition range without phase separation by radio frequency molecular beam epitaxy [39, 91]. Growth of single crystalline $In_xGa_{1-x}N$ films with In content of (70-100%) were grown by MOCVD, however PL measurements showed phase separation for $In_{0.8}$ $Ga_{0.2}N$ [92]. So far no detailed studies on optical, structural and transport properties for In-rich $In_xGa_{1-x}N$ alloys with x = (1.0- 0.4) by MOCVD had been reported.

In this section of chapter, we report the growth and characterization of In-rich $In_xGa_{1-x}N$ epilayer with x ~ (0.4 - 1.0) by MOCVD on AlN templates. $In_xGa_{1-x}N$ alloys of thickness (300-800 nm) with varying x~ (0.4 - 1.0) were grown on AlN/Al_2O_3 templates by MOCVD. Metalorganic precursors used were TMAl for Al, TMIn for In, TEGa for Ga and NH_3 for nitrogen. Templates were preheated in NH_3 environment prior to growth. $In_{0.15}Ga_{0.85}N$ epilayer grown at 800^{o}C with thickness of ~ 20 nm was employed to reduce the lattice mismatch between In-rich $In_xGa_{1-x}N$ and AlN epilayers and to improve the quality of top In-rich $In_xGa_{1-x}N$ epilayers. Typical flow rate used was 100-200 ml/min for TMIn, with increasing flow rates of TEGa (3 ml/min -140ml/min) to increase the Ga content from 0 % to 60 %, and 7.0-2.4 L/min of NH_3. The growth pressure of 600 torr was found the optimum pressure for all percentages. Growth temperature was increased from 570^{o}C for InN to 700^{o}C for $In_{0.4}Ga_{0.6}N$ to improve the quality of In-rich $In_xGa_{1-x}N$ epilayers. In-contents in InGaN epilayers were estimated from peak position of XRD curves of (0002) plane in θ-2θ scan mode and applying Vegard's law. The growth rate and thickness of the films were estimated from in-situ interference measurements during the epi-growth. Transport, optical and structural properties were studied by Hall Effect measurement, PL, and XRD respectively.

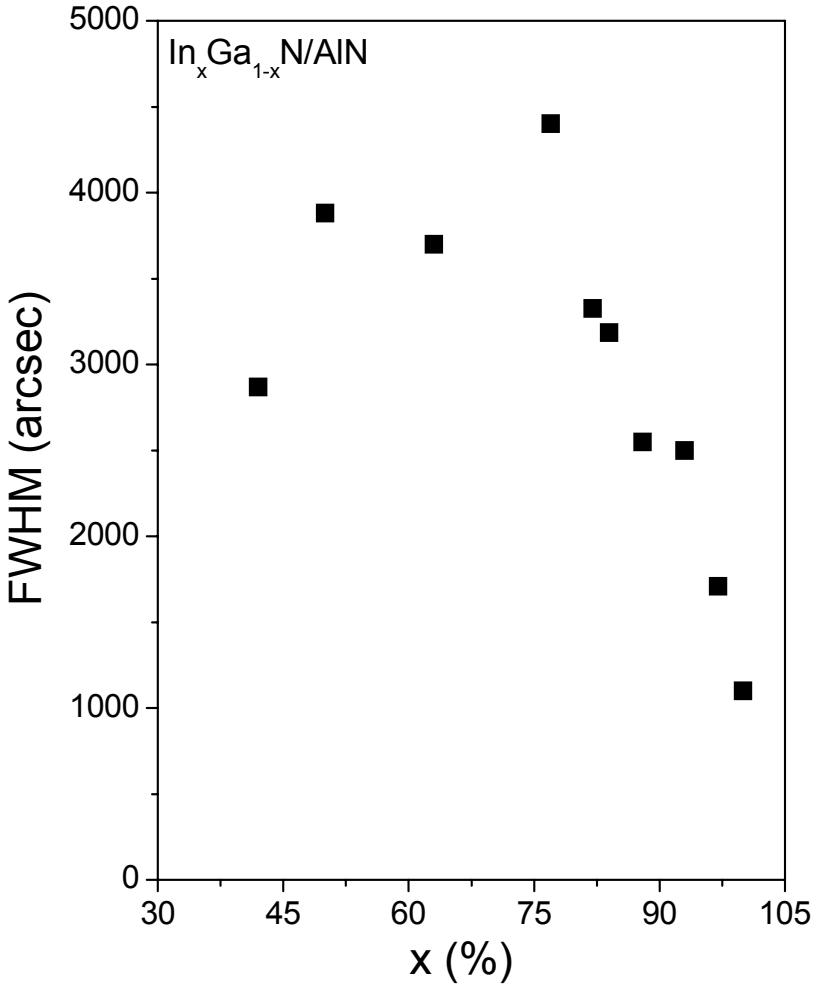

Figure 3.12 Plot of XRD rocking curves for In-rich $In_xGa_{1-x}N$ alloys verses Indium content

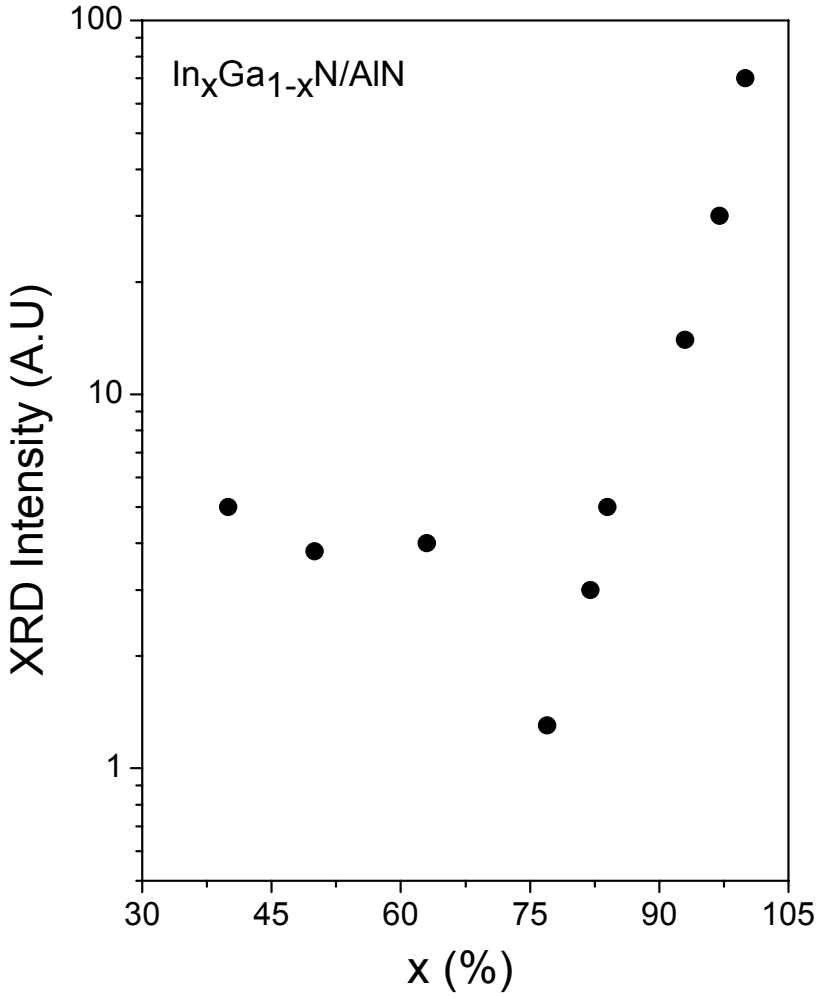

Figure 3.13 XRD rocking curve intensity in log scale verses Indium content for In-rich $In_xGa_{1-x}N$ alloys.

Figure 3.11 shows the normalized XRD (0002) θ-2θ curves of $In_xGa_{1-x}N$ with (x= 0.4 – 0.1) alloys grown on AlN/Al_2O_3 templates. The diffraction angle of 31.38^o is attributed to InN and other angles ranged from 31.46^o- 33.24^o to $In_xGa_{1-x}N$ with (x=0.97-0.40). However with increase of Ga composition in $In_xGa_{1-x}N$, the (0002) bragg reflection is broadened, indicating that the $In_xGa_{1-x}N$ alloy may not be chemically homogenous [42]. The broadening is maximum for $In_xGa_{1-x}N$ with (x = 0.71) and the line width starts to improve again with increasing Ga percentage. Phase separation was observed for $In_xGa_{1-x}N$ with (x = 0.63, 0.71) but was suppressed by optimizing the growth temperature and V/III ratio. Thus $In_xGa_{1-x}N$ alloys with (x= 0.4-0.1) were successfully grown without phase separation.

Plot of XRD rocking curves of InGaN alloys verses Indium content is shown in figure 3.12. Figure shows that FWHM value increases from 1100 arcsec to 4700 arcsec as In content varied from 1.0 to 0.74 in In- rich $In_xGa_{1-x}N$ alloys grown on AlN templates, then starts to decrease again from 4700 to 2800 arcsec as In content changed from 0.74 to 0.40. Figure 3.13 shows the XRD rocking curve intensity in log scale verses In content for In-rich $In_xGa_{1-x}N$ alloys. The plot shows that intensity correlated well, with the FWHM from XRD rocking curve shown in figure 3.12. The higher the XRD intensity the smaller is the FWHM and vice versa, which indicated the improvement in quality.

Compositional dependence of hall mobility (μ) of $In_xGa_{1-x}N$ alloys with In content is plotted in figures 3.14. The electron mobility was ~ 1400 cm^2/ Vs for the best grown InN films, but decreased for In-rich $In_xGa_{1-x}N$ films with increasing Ga content as can be seen from figure 3.14. For example the electron mobilities were 800, 480, 350, 220, 53, 45, and 30 cm^2/Vs for InGaN films with 97%, 93%, 88%, 81%, 71%, 63% and 40% In content respectively. Whereas the μ measured for GaN epilayers was 400 cm^2/Vs. Thus it is predicted that the μ Vs x curve may increase again below 40% to 0% In content.

Figure 3.15 shows the plot of electron concentration (n) verses In content for $In_xGa_{1-x}N$ alloys. It is observed that n increases with decreasing In content from $7x10^{18}$ cm^{-3} for InN to a maximum of 1.4 $x10^{19}$ cm^{-3} for 74% In content and then decreases afterwards. The n measured for GaN epilayers was $3x10^{17}$ cm^{-3}.

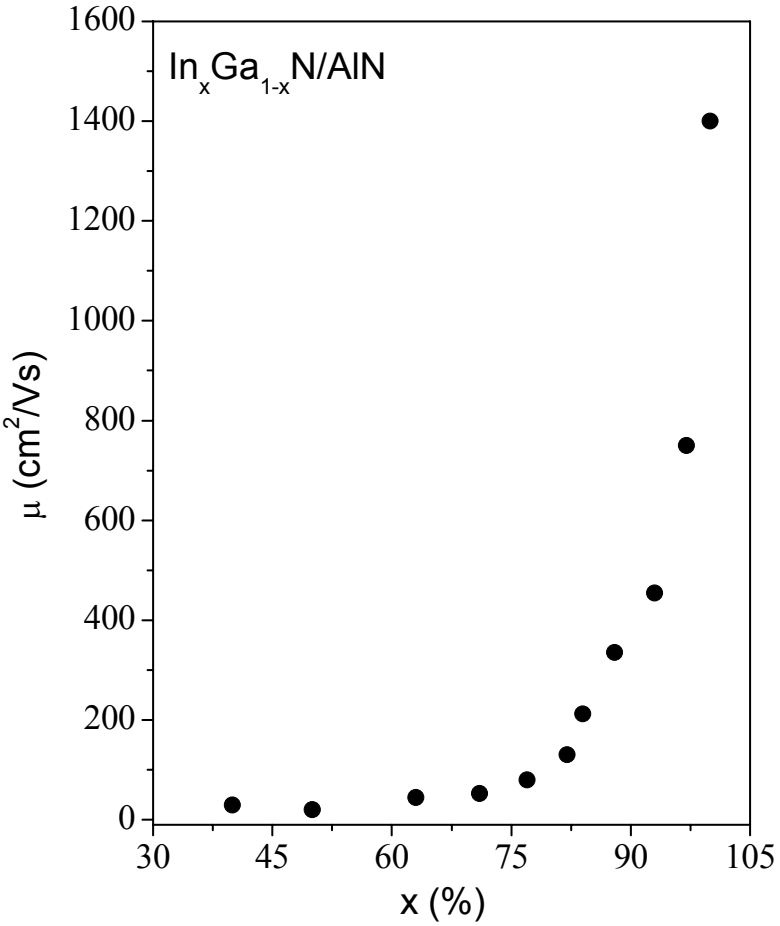

Figure 3.14 Compositional dependence of hall mobility (μ) of In-rich $In_xGa_{1-x}N$ alloys with In content.

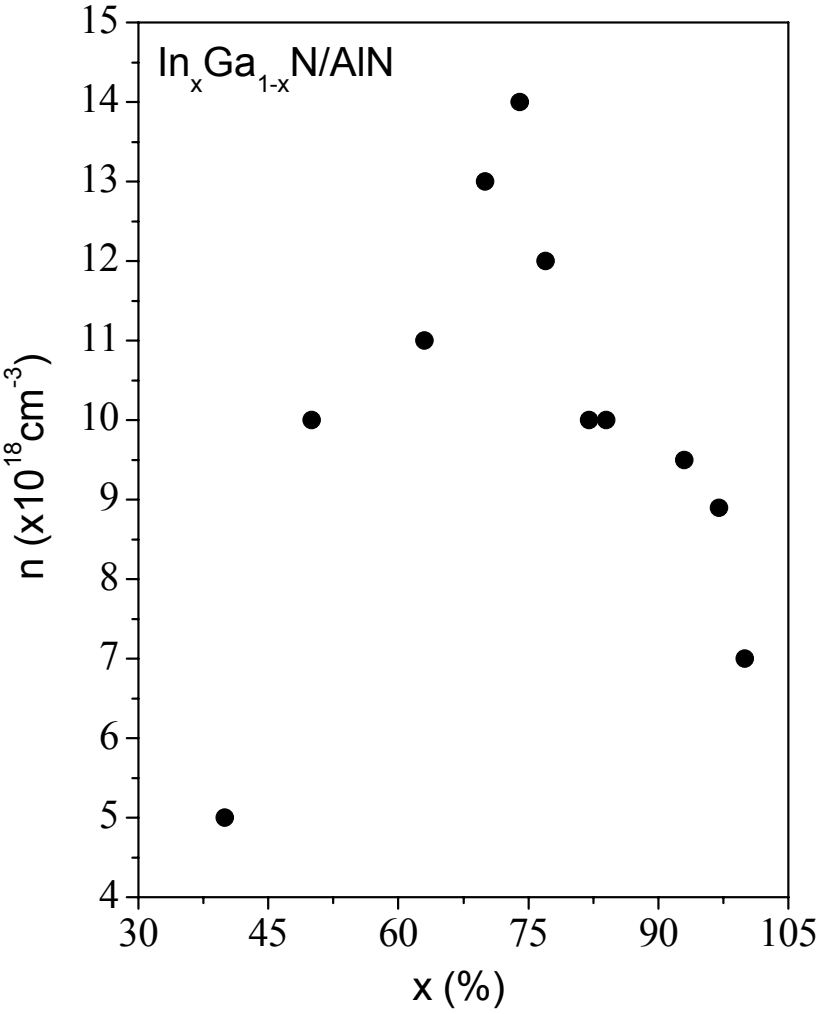

Figure 3.15 The plot of electron concentration (n) verses In content for In-rich $In_xGa_{1-x}N$ alloys.

The increase in n up to 74% In content is consistent with the XRD rocking curve FWHM which was maximum for 74% In content, thus indicates that the generation of defects or inhomogeniety of In and Ga increases the electron concentration.

Figure 3.16 shows room temperature PL spectra for In-rich $In_xGa_{1-x}N$ containing 100%, 97%, 93%, 88%, 82%, 77% and 63% In content respectively. The PL spectra revealed band to band emission for InN epilayers at 0.76 eV and shifts to 1.15 eV when In content varies from 100% to 63%. The inset in figure shows 10 K PL spectra for InGaN with 63% In content. At low temperature PL intensity increases and PL spectra peak blue shifts to 1.17 eV, which is the usual behavior for III-nitrides at low temperature. There is in addition a high energy PL wing in InN and In-rich InGaN alloys and the same was observed in[93, 94] which could be due to non uniform spatial distribution of electrons in conduction band[95].

PL emission intensity (I_{emi}) increases for $In_xGa_{1-x}N$ epilayers with the increase of Ga content up to 88% and then shows a decrease again. The increase in intensity may be due to improved PL quality because of increased growth temperature with Ga content. But decrease in PL intensity above 88% In content could be due to increase in defects and inhomogeneous distribution of Ga and In atoms in $In_xGa_{1-x}N$ epilayers.

In summary InN and In-rich $In_xGa_{1-x}N$ (x~0.97- 0.40) epilayers were grown on AlN/Al_2O_3 templates. The photoluminescence (PL) emission spectra revealed a band to band emission peak at ~0.76 eV for InN. This peak shifted to 1.15 eV when In content was varied from 1.0 to 0.63 in In-rich $In_xGa_{1-x}N$ epilayers. After growth process optimization, In- rich $In_xGa_{1-x}N$ alloys with (x= 0.97-0.40) were successfully grown without phase separation.

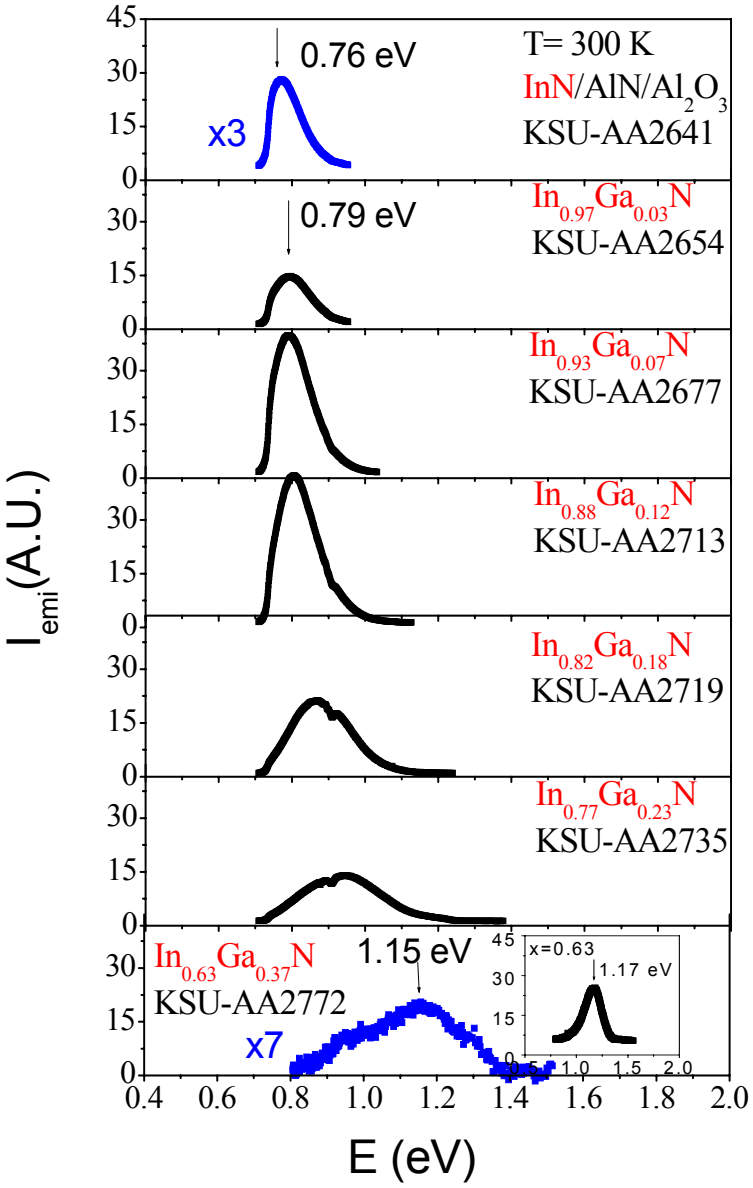

Figure 3.16 Room temperature photoluminescence spectra (PL) for In-rich $In_xGa_{1-x}N$. The inset shows 10 K PL for x=0.63.

3.4. Mg acceptor level in InN epilayers probed by photoluminescence

In recent years, research interest in Indium nitride (InN) has significantly increased due to the new confirmation of its small band gap energy ~ 0.62-0.7 eV [22-29, 96] and its potential applications in semiconductor devices such as light emitting diodes, laser diodes, high efficiency solar cells, high performance electronic devices and in the telecommunications wavelength region (1.55 μm) [34, 94, 97]. Achieving p-type conduction in InN and high In content InGaN alloys is essential for many device applications, but has been exceedingly difficult due to the fact that as-grown InN epilayers are generally highly n-type. There has been strong evidence that InN contains an electron accumulation layer on its surface [22]. Thus even if p-type conductivity in bulk InN is successfully achieved by Mg doping, its surface will remain highly n-type which creates problems in the demonstration of p-type InN, as electrical measurements are often dominated by surface n-type conducting layers [98, 99].

Compared to Mg-doped GaN, very few studies have been done so far concerning the basic properties of Mg-doped InN [55, 57, 100, 101]. A previous study using X-ray absorption fine structure analysis suggested that Mg atoms occupy either the In metal (Mg_{In}) or interstitial (Mg_{Int}) site; Hall effect measurements, however, revealed n-type behavior [101]. More recently, the evidence of a buried p-type layer in Mg doped InN was provided by capacitance-voltage (CV) measurements [57]. Further evidence of a buried p-layer beneath a surface electron accumulation layer in heavily Mg-doped InN was provided by variable magnetic field Hall effect and CV measurements, from which an energy level of about 110 meV was suggested for the Mg acceptors in InN [55]. So far, detailed studies concerning the optical transitions and the Mg acceptor energy level in Mg-doped InN have not been possible due to the fact that most Mg-doped InN films exhibit no (or weak photoluminescence (PL) emission.

In this section, we discuss the growth and PL emission characteristics of Mg-doped InN epilayers grown on sapphire substrates by metal organic chemical vapor deposition (MOCVD). The effects of the Mg flow rate (R_{Mg}) on the PL emission properties of Mg-doped InN epilayers have been investigated by varying R_{Mg} from 8.5 to 60 ml/min corresponding to Mg doping concentration of 1.8 x 10^{20} to 1.3 x 10^{21} cm^{-3}. The PL spectroscopy system consists of a 100 fs Ti: Sapphire laser (λ_{exc} = 780 nm), a 0.3

m monochromator, and an InGaAs detector. Electrical properties of Mg-doped InN epilayers were examined by Hall effect measurement. X-ray diffraction (XRD) was employed to study the crystalline quality of Mg-doped InN.

The 0.2 μm thick Mg-doped InN epilayers were grown by MOCVD on sapphire (0001) substrates using 1.5 μm thick GaN epilayer templates. $In_{0.2}Ga_{0.8}N$ with thickness of about 15nm was inserted to reduce the mismatch between GaN and InN. Trimethylindium (TMIn), Trimethylgallium (TMGa) and NH_3 were used as In, Ga, and N sources, respectively. For Mg doping, bis-cyclopentadienylmagnesium (CP_2Mg) was transported into the growth chamber during InN growth. The growth rates of InN and GaN were 80 nm/hr and 2.4 nm/hr respectively. Figure 3.17 shows the sample structure of Mg-InN grown on GaN templates. Atomic force microscopy (AFM) revealed a root mean square (rms) of surface roughness of about 25-30 nm on 10 μm x 10 μm area scans, which was comparable to that of undoped InN. The surface morphology started to deteriorate when R_{Mg} exceeded 35 ml/min. Both undoped and Mg-doped InN films were shown to be single crystals by XRD, with a c-spacing of around 0.568 nm. The FWHM of the rocking curve of the (0002) plane of undoped (Mg-doped) InN epilayers was ~ 500-540 (550-630) arcsec.

Hall effect measurement was attempted to measure the conductivity of Mg-doped InN epilayers. Complete electron compensation by Mg acceptors could not be observed. However, increasing the Mg flow rate from 8.5 to 60 ml/min reduced the electron concentration (n) from $2x10^{19}$ to $3x10^{18}$ cm^{-3} and the n-type conductivity (σ) from 1250 to 125 $(\Omega cm)^{-1}$ for samples annealed at 500^o C for 4 min in air.

Figure 3.18 shows 10 K PL spectra of a set of Mg-doped InN grown under different R_{Mg}, where the PL spectrum of an undoped InN epilayer is also included for comparison. The dominant PL emission peak is at 0.82 eV in the undoped InN epilayers, which is higher than the recently reported band gap of InN (0.62-0.7 eV) [22-29, 96]. This spectral blue shift has been previously observed in both optical absorption [44, 87] and PL spectra of InN [86, 87, 102] and can be accounted for by the fact that the electron Fermi level (E_F) is above the conduction band minimum or the so-called Moss-Burstein blue shift due to high electron concentration [44, 86, 87, 102].

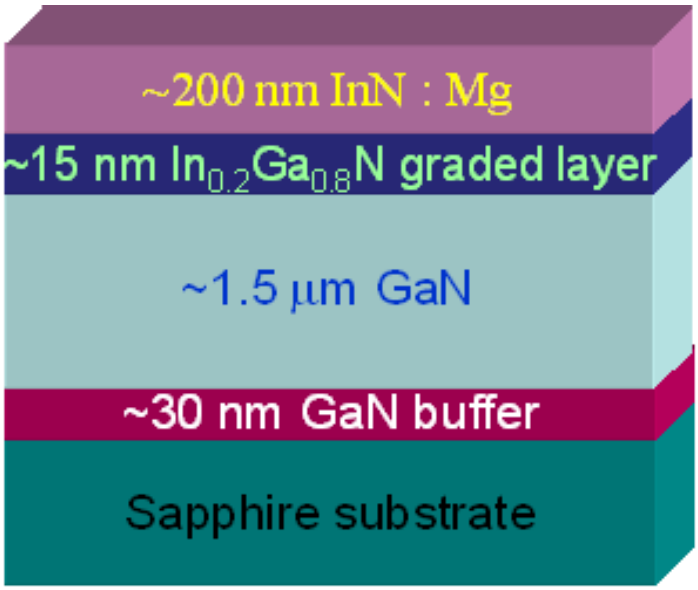

Figure 3.17 Sample structure of Mg-InN grown on GaN templates

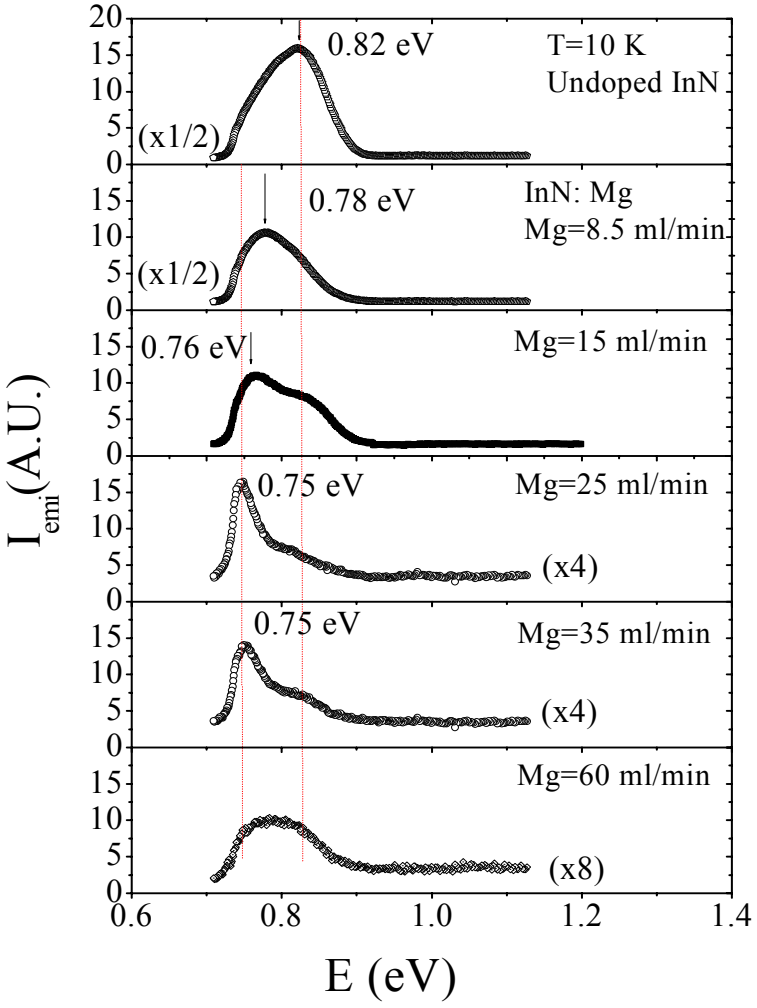

Figure 3.18 10 K PL spectra of Mg doped InN epilayers grown under different Mg flow rates (R_{Mg}). PL spectrum of an undoped InN epilayer is also included for comparison.

With respect to the conduction band minimum, E_F can be written as $E_F = \hbar^2/2m^* (3\pi^2 n/\upsilon_D)^{2/3}$ [103], where υ_D is the degeneracy factor which is 2 for this case, and n and m* are the electron concentration and electron effective mass, respectively. Using m* ~ 0.11 m_o [104] and n= (1.9-2.0) x 10^{19} cm^{-3} for undoped InN, we obtained E_F = 140-150 meV.

Based on this and the room temperature spectral peak position of about 0.80 eV observed in the undoped InN, the band gap of InN is thus deduced to be 0.66-0.65 eV which is in reasonable agreement with the previously reported band gap of InN (~ 0.62-0.7 eV). We thus label the 0.82 eV emission line as the band edge emission line in InN. Compared to the undoped InN layer, a new emission line at ~ 0.76 eV emerges and is the dominant emission line in Mg-doped InN epilayers. Since this 0.76 eV emission line is absent in undoped InN, we attribute it to the Mg- related line. This Mg-related emission line is about 60 meV below the band edge emission line at 0.82 eV.

Fig. 3.19 summarizes the influence of R_{Mg} on the PL emission properties of the Mg-related line in terms of (a) the spectral peak position, E_p (b) line width, FWHM and (c) the intensity ratio of the Mg-related emission line to the band edge emission line. Both E_p and FWHM decrease initially with increasing R_{Mg} up to 25 ml/min and then increase. A similar trend is seen for the band edge emission line at 0.82 eV. The spectral blue shift seen for R_{Mg} > 25ml/min could be due to the increased incorporation of defects and impurities at higher R_{Mg} that increase n and E_F [105]. The integrated emission intensity (I_{emi}) of the Mg-related transition is observed to decrease exponentially with increasing the Mg doping concentration, following a similar trend of the Mg related transition line in Mg-doped GaN [106]. However, the relative intensity of the Mg-related emission line to the band edge emission line exhibits a maximum at R_{Mg} =25 ml/min as shown in Fig. 2 (c).

Figure 3.20 presents the PL spectra measured at different temperatures for the Mg-doped InN epilayer grown under R_{Mg} =15 ml/min. The spectral peak separation of about 60 meV between the Mg-related and band edge emission lines can be clearly measured at T < 100 K. At T > 100 K, only the Mg-related emission line can be resolved.

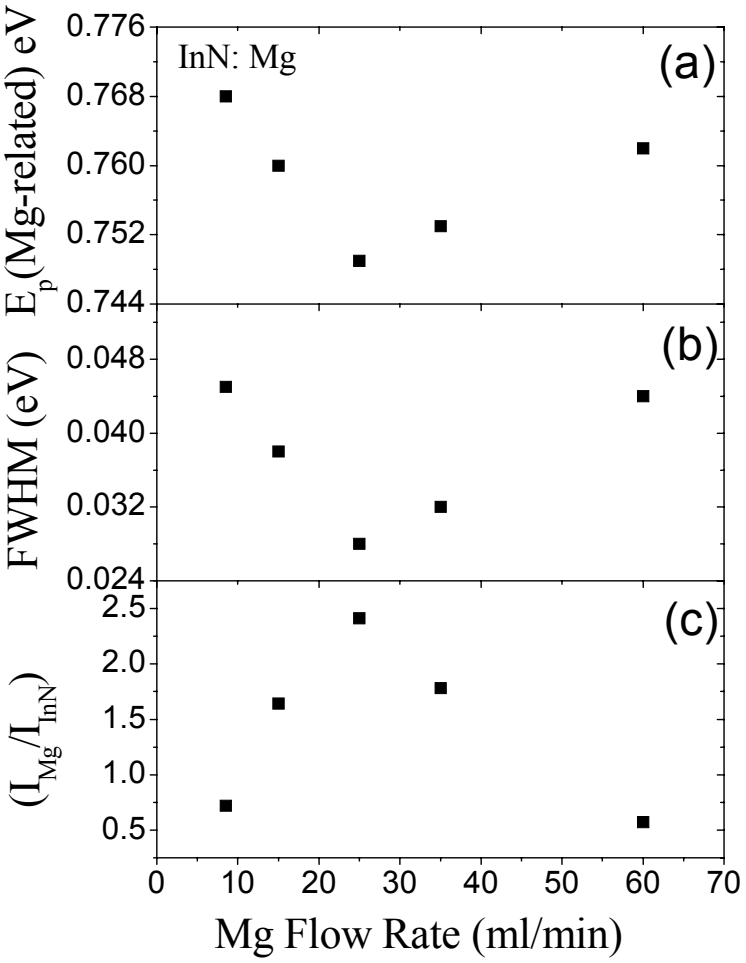

Figure 3.19 Variations of the (a) spectral peak position, E_p, (b) full width at half maximum, FWHM and (c) intensity ratio of the Mg related emission line to the band edge transition line with the Mg flow rate, R_{Mg}.

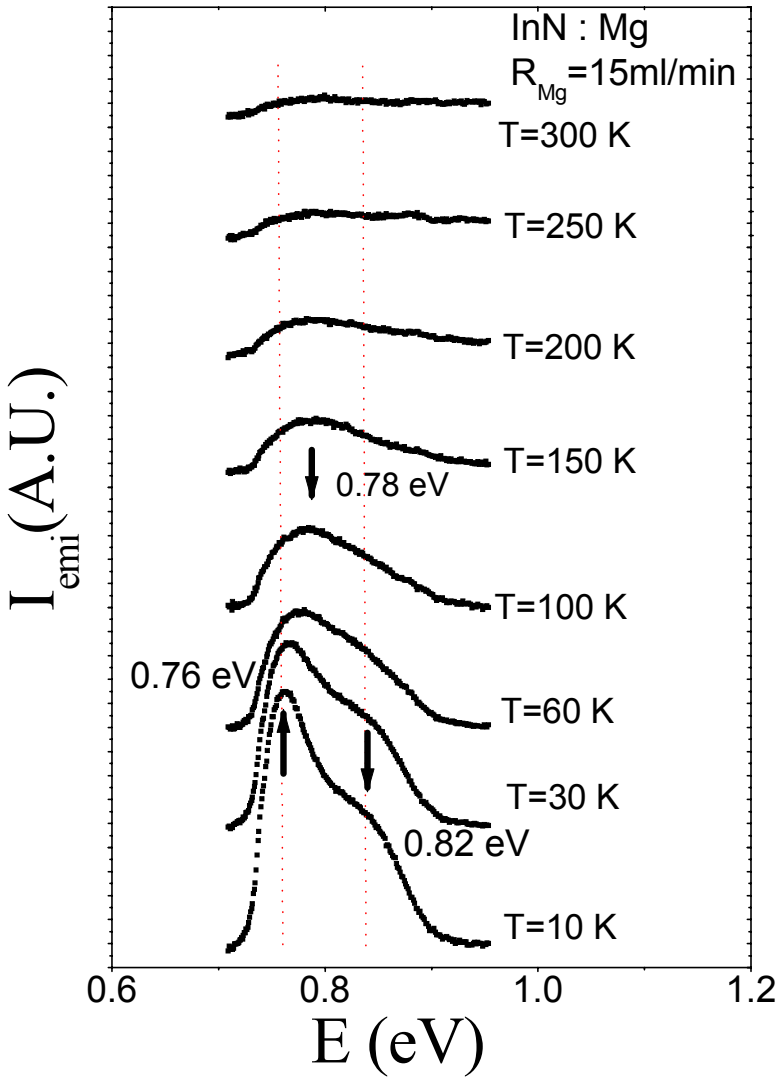

Figure 3.20 PL spectra of Mg doped InN grown under the Mg flow rate R_{Mg}=15ml/min, measured at different temperatures.

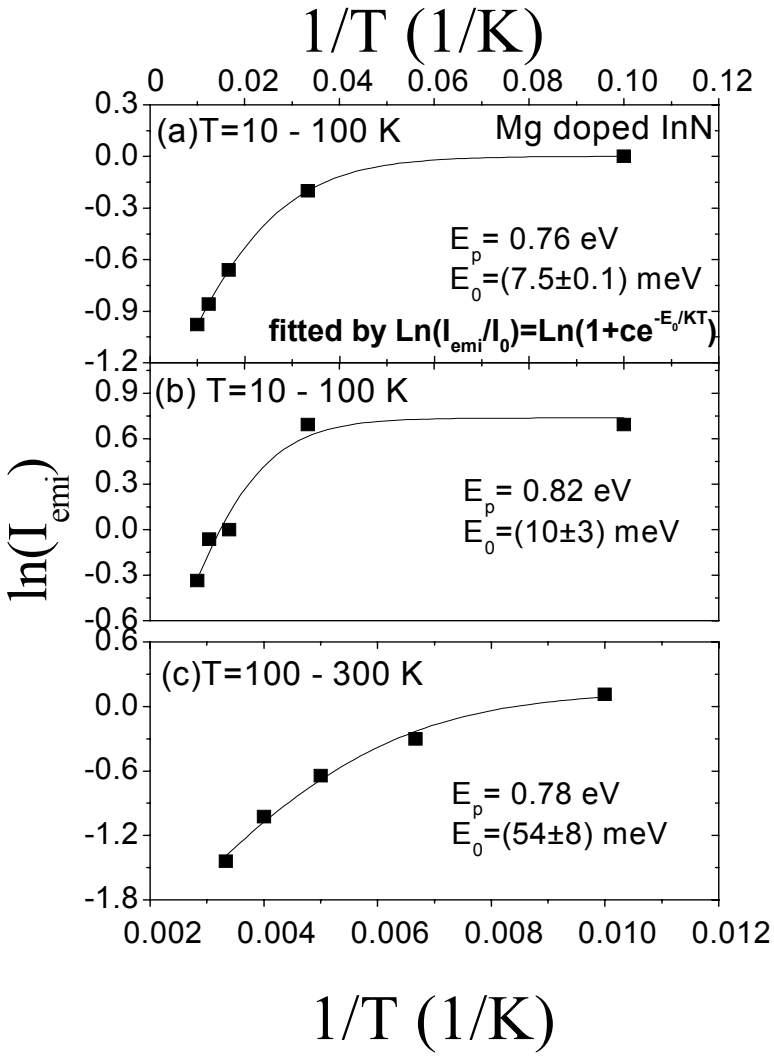

Figure 3.21 The Arrhenius plots of PL emission intensity, ln (I_{emi}) vs. 1/T], for (a) the Mg related emission line measure in the temperature range of T =10-100 K, (b) the band edge emission line measured in the temperature range of T= 10-100K and (c) the Mg related emission line measured at T=100-300 K. The fitted activation energies (E_0) are indicated in the figure.

Both of the emission lines exhibit a blue shift with increasing temperature. This blue shift with temperature is in a sharp contrast to the temperature dependence of the direct band gap (E_g) in most semiconductors, in which a reduction of E_g with increasing temperature is typically observed. The spectral blue shift with temperature may be caused by the increase of the electron Fermi level due to an increase of the electron concentration at higher temperatures [28, 107]. This interpretation is also supported by the Hall Effect measurement results that revealed a linear increase of electron concentration with temperature.

The Arrhenius plots of PL emission intensities measured in different temperature ranges for Mg-doped InN with R_{Mg} =15 ml/min is shown in Fig. 3.21. The solid lines are the least square fit of data with equation $I_{emi}(T) = I_0/[1+ C \exp(-E_0/KT)]$, where E_0 is the activation energy of I_{emi}. The Arrhenius plots in the temperature range 10-100 K as shown in Fig. 3.21 (a) and 3.21 (b) yield activation energies of 7.5 meV and 10 meV, respectively, for the Mg-related emission line and the band edge emission line, which may be accounted for by non radiative recombination channels [94, 102]. In the temperature range of 100-300 K, the activation process is governed by an activation energy of 54 meV. This activation energy coincides fairly well with the spectral peak energy difference of about 60 meV between the Mg-related and band edge transition lines. We therefore believe that the Mg acceptor energy level in InN is about 60 meV above the valance band maximum. The Mg acceptor binding energy of 60 meV in InN obtained from our present work matches well with a recently reported value of about 62 meV observed in Mg-doped InN epilayers grown by molecular beam epitaxy [77].

In summary we have grown by MOCVD and studied the PL emission characteristics of Mg-doped InN epilayers. An emission line of about 60 meV below the band edge emission, which was absent in undoped InN epilayers, was observed in Mg doped InN. Together with the temperature dependent PL emission intensity result, we suggest that the Mg acceptor level in InN is about 60 meV above the valance band maximum.

3.5 Effects of compressive strain on optical properties of $In_xGa_{1-x}N$/GaN quantum wells

Current intensive research on III-nitrides has led to significant progress in optoelectronic devices such as blue/green light emitting diodes (LEDs) and laser diodes (LDs) and high power electronic devices. To further improve the performance of III-nitride-based optoelectronic and microelectronic devices, a better knowledge of its growth kinetics, surface morpholgy and strain or stress states between the epitaxial layers and the substrate, because of difference in lattice mismatch and thermal expansion coefficients is needed [108-110]. The effect of mis-orientaion of a substrate on surface morphology and structural properties of GaN epilayers have already been studied[108, 111, 112]. The slightly mis-oriented c-plane sapphire has been widely used after it was reported that they significantly affect the surface morphology of GaN epilayers [112]. Mechanical stresses are known to greatly effect the semiconductor band gaps and effective masses of electrons and holes. [113] Several groups have studied effects of stress or strain on the optical properties of $In_xGa_{1-x}N$/GaN quantum wells (QWs) subjected to variable amount of lattice mismatch induced strain by changing In content or QW width[114-116]. However, there is no report on the strain induced variation in the band gap of $In_xGa_{1-x}N$/GaN MQWs, which is critical for the performance of nitride LEDs.

In this section, we discuss the effects of compressive strain on the optical properties of blue LEDs based on InGaN/GaN multiple quantum wells (MQWs), grown by MOCVD. And also the effect of mis-orientaion on surface morphology of blue LED will be described. We designed a substrate which provides varying degrees of off-cut angle with respect to c-plane, within a single wafer and also increasing thickness from edge (450 μm) to center (350 μm) of wafer to study the effect of geometry on the strain or stress states and the optical properties of Blue LED. The 3D image and variation of off-cut angle with distance of specially designed substrate are shown in figure 3.22 (a) and (b) respectively. The inset in figure 3.22 (b) shows the top view of specially designed substrate. The off-cut angle increased from 0.035 in the specially designed substrates center to about 0.7 degrees near the edge and had the same trend in all directions A, B, C and D. The direction of the off-cut angle also varied with azimuthal angle.

(a)

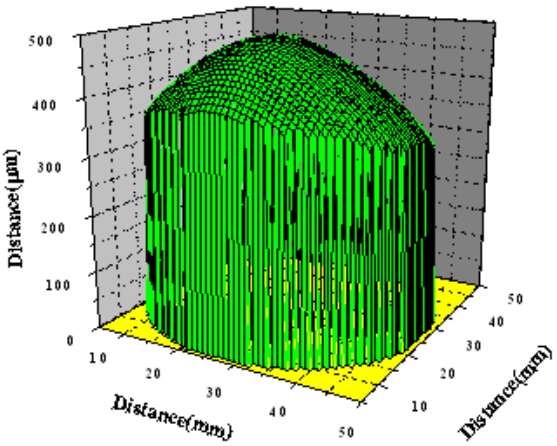

(b)

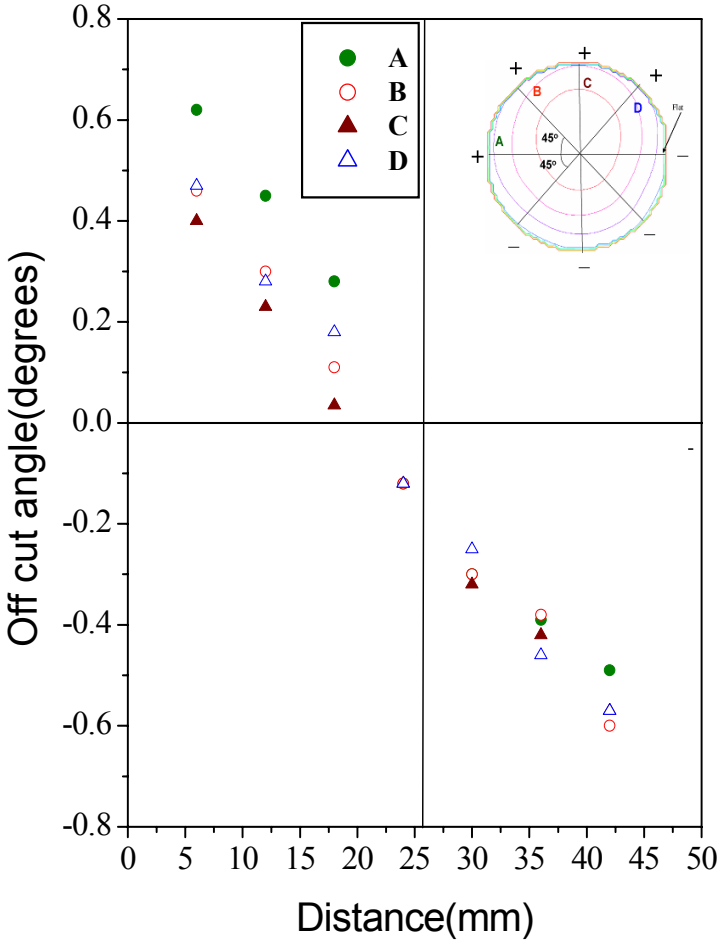

Figure 3.22 (a) The 3D image, and (b) The variation of off-cut angle with distance of specially designed substrate. The inset shows top view of specially designed substrate.

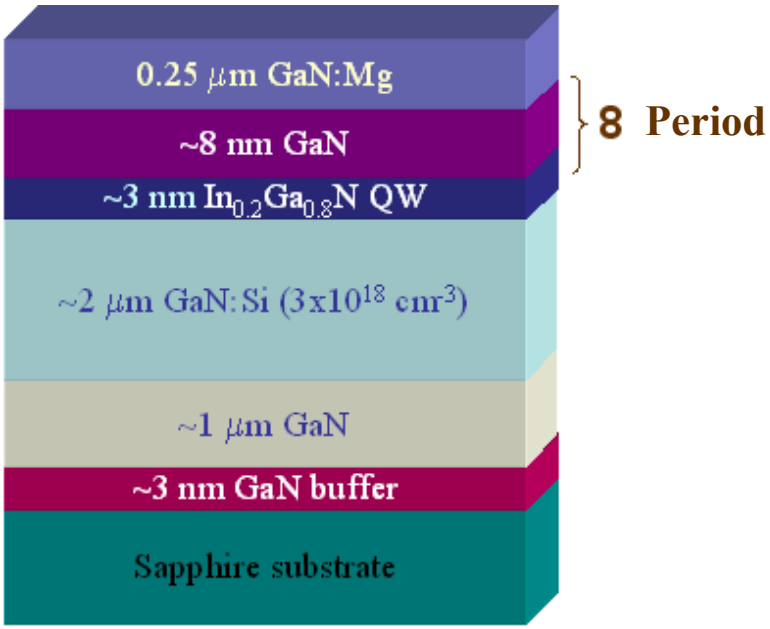

Figure 3.23 The schematic of the layered structure of blue LEDs

X- ray diffraction (XRD) was employed to characterize the crystalline structure and studying strain in GaN epilayers. The ratio of elastic stiffness constants (C_{33}/C_{13}) for GaN was deduced to be ~ 5.0 ± 1.0, which was in agreement with calculated value of ~ 4.0 [117]. Electroluminescence (EL) was measured to study the optical properties of $In_{0.2}Ga_{0.8}N$/GaN MQW. Linear coefficient of $In_xGa_{1-x}N$ alloys which describes the variation of $In_xGa_{1-x}N$ band gap per unit stress is obtained.

Nitride blue LED wafers were grown by MOCVD on 2 inches specially designed sapphire substrate and flat sapphire substrates, simultaneously in the reactor. A low temperature GaN buffer layer with thickness ~30 nm was deposited at ~ 530^o C prior to the growth of ~ 3 μm GaN with Si doping of 3x $10^{18}cm^{-3}$ at ~ 1100^o C. Then 8 periods of $In_{0.2}Ga_{0.8}N$/GaN (3nm/8nm) MQWs and lastly ~0.25 μm Mg-doped GaN was deposited at ~1040^o C. Figure 3.23 shows the schematic of the layered structure of blue LEDs.
Surface morphology of LED wafers grown on specially designed and flat sapphire substrates was measured at different positions from one end of the wafers to other using optical microscope. Fig.3.24 (a) shows optical microscope images of an area of 200 μm x 200 μm blue LED wafer grown on the specially designed substrate, at different positions from one end to the other. Corresponding off cut angle to each position is also shown. It was seen that surface morphology was best for $\theta = \pm 0.3^o$ off cut angles for the specially designed substrate. However, the surface morphology was almost uniform at all positions for blue LED wafer grown on flat sapphire substrate as shown in Fig.3.24 (b).

It is predicted that 0.3 degree of off cut angle provides optimum step density for smoother growth by MOCVD. These steps have an average distance of about 50 nm, which is smaller than diffusion length of Ga atoms adsorbed on the surface [118].

The most direct approach for studying strain or crystalline structure in epitaxial GaN is done through (XRD) measurements [119]. Crystalline structure of these wafers was studied by using XRD. The inset of Fig. 3.25 shows the top view of the specially designed substrate. GaN lattice constant “c” was deduced from (0002) peak position. It increased from center of wafer towards edge, and had the same trend in all directions A, B, C and D as shown in Fig. 3.25.

(a)

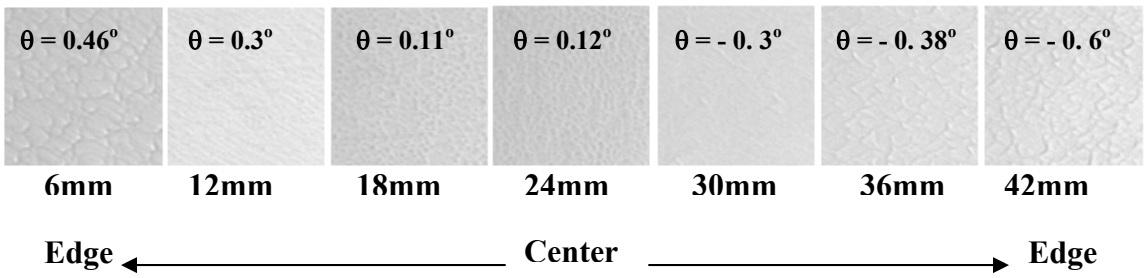

(b)

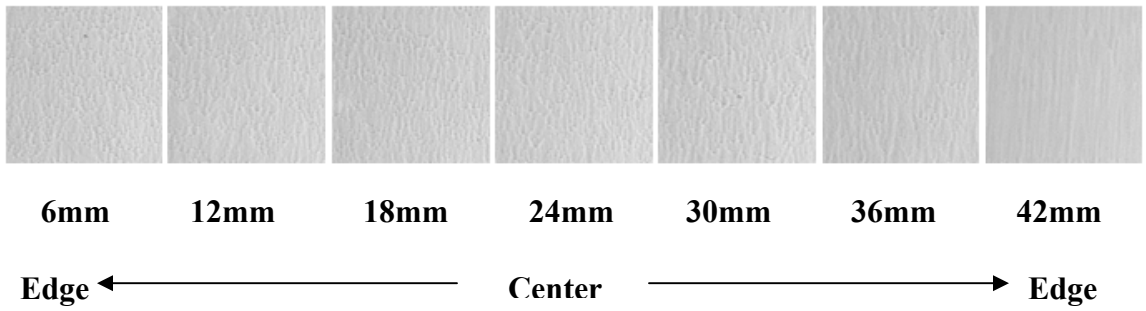

Figure 3.24 Optical microscope image (200 μm x 200 μm) of LED wafer grown on (a) specially designed and (b) flat sapphire substrates.

GaN in plane lattice constant "a" was calculated from (104) peak position, and an inverse relation between lattice constants "c" and "a" was observed. Whereas, there was no variation in (0002) and (104) GaN peak positions for LED wafers grown on flat sapphire substrates.

The measured variation of GaN lattice constants "c" and "a" for LED wafer grown on the specially designed substrate was related to the compressive strain which was larger at the edges as compared to the center. This difference in strain may have to do with geometry of substrate as it has varying thickness but the reason is un clear for this trend of variation in compressive strain and may need further investigation.

We calculated ratio of elastic stiffness constants for GaN epilayer using our experimental data for GaN lattice constants "c" and "a". We consider the case of biaxial strain along the c-axis for GaN. The corresponding stress tensor follows Hooke's law as

$$\sigma_{xx} = (C_{11} + C_{12})\,\varepsilon_{xx} + C_{13}\varepsilon_{zz}\,, \tag{3.1}$$

$$\sigma_{zz} = 2C_{13}\varepsilon_{xx} + C_{33}\,\varepsilon_{zz}\,, \tag{3.2}$$

Where, $\varepsilon_{xx} = (a-a_o)/a_o$ and $\varepsilon_{zz} = (c-c_o)/c_o$, and a ($a_o$) and c ($c_o$) are strained (unstrained) lattice constants.

The biaxial strain parallel to the c-axis is characterized by vanishing forces in this direction, $\sigma_{zz} = 0$, for all layers of a multilayer structure.[113, 117] Using this condition and Eq. (3.2) we have

$$a = (1+C_{33}/2C_{13})\,a_o - (a_oC_{33}/2c_oC_{13})\,c, \tag{3.3}$$

As shown in Fig. 3.26, GaN lattice constant "a" is plotted against lattice constant "c". From linear fitting of our data with Eq. 3.3, we obtained $(1+C_{33}/2C_{13})\,a_o = (11.19 \pm 1.61)$ and $(a_oC_{33}/2c_oC_{13}) = (1.55 \pm 0.31)$ which both gives $C_{33}/C_{13} \sim 5.0 \pm 1.0$, which was in agreement with the calculated value, $C_{33}/C_{13} \sim 4.0$. [117]

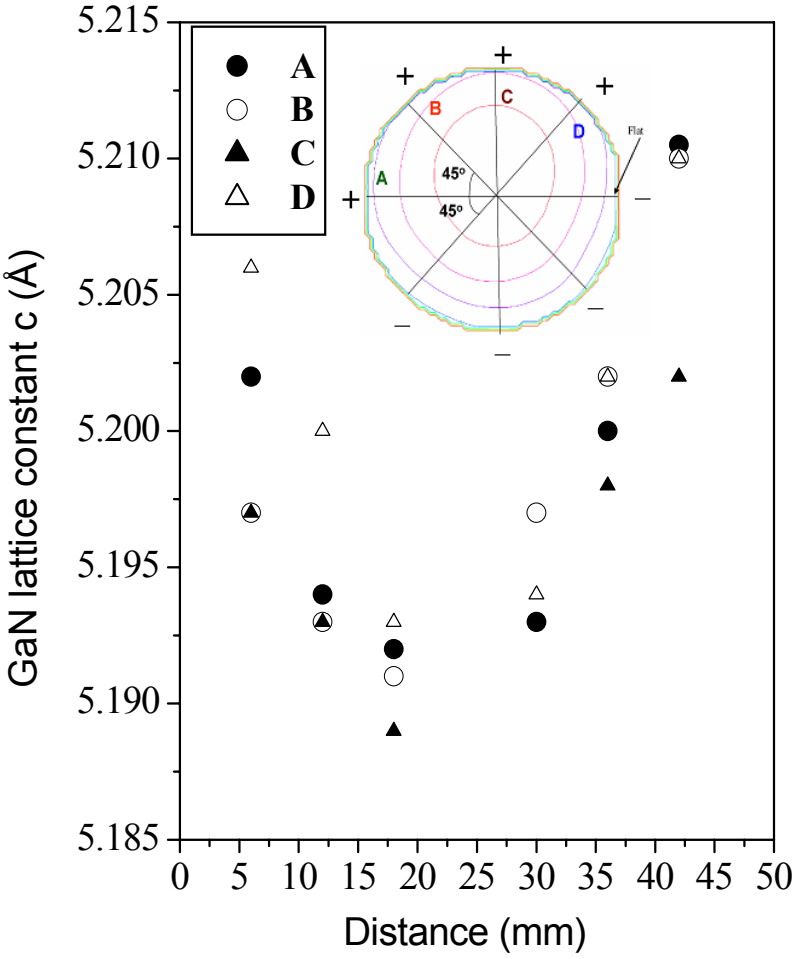

Figure 3.25 GaN lattice constant "c" verses off cut angle,θ, along directions A, B, C and D. The inset shows top view of specially designed substrate.

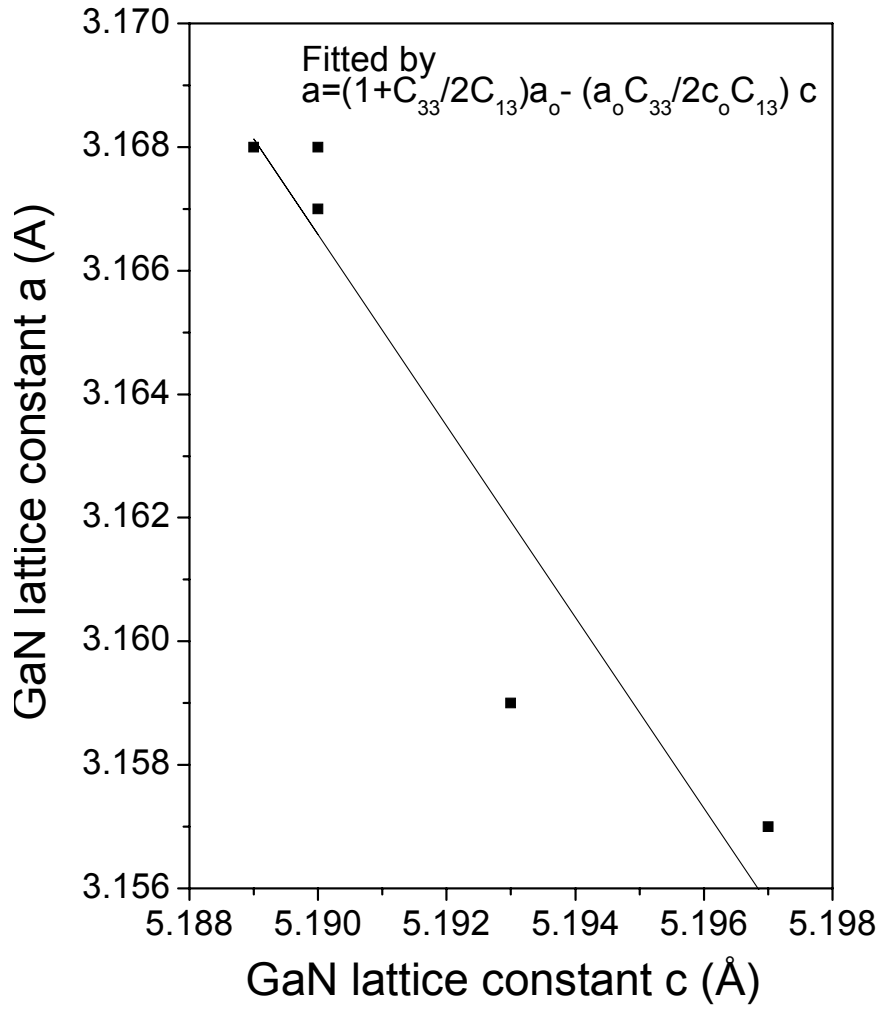

Figure 3.26 GaN lattice constants “c” verses “a” for LED wafer grown on specially designed substrate.

EL was measured for blue LEDs grown on specially designed and flat sapphire substrates as shown in Fig. 3.27. Emission peak positions were almost constant at all the positions on the flat sapphire substrate (Fig. 3.27a).

However, LEDs grown on the specially designed substrate showed emission at shorter wavelength ~ 456 nm at the edges as compared to at the center ~ 464 nm (Fig. 3.27 b). This was due to larger compressive strain at positions close to the edges of the specially designed substrate, than to the center. It is known that the band gap energy of a nitride layer is affected by the residual stress in the film. A tensile stress will result in a decrease of energy band gap while a compressive strain causes an increase of the band gap [109, 120, 121]. So the larger compressive strain resulted in EL emission peak position moving towards shorter wavelength.

The EL emission energy peak position as a function of GaN lattice constant "c" is plotted in Fig. 3.28. A linear dependence of emission energy with lattice constant "c" is apparent. After linear fit of the data as is shown in Fig. 3.27, band gap energy of $In_{0.2}Ga_{0.8}N$/GaN QWs can be expressed in terms of change in GaN lattice constant according to

$$E_g = 2.67+2.43\Delta c, \tag{3.4}$$

Where $\Delta c=c-c_{o,}$ which represents change in GaN lattice constant. Here E_{go}= 2.67eV is the emission energy of $In_{0.2}Ga_{0.8}N$/GaN MQWs without stress. The biaxial stress dependence of the band gap energy can be expressed as.

$$E_g = E_{go} + B\sigma_{xx}\,(eV), \tag{3.5}$$

Where E_{go} and σ_{xx} are unstrained band gap energy and biaxial stress, respectively. B is the linear coefficient characterizing the relationship between the band gap and biaxial stress [109]. Again considering the case of biaxial strain along c-axis for $In_{0.2}Ga_{0.8}N$ which is characterized by vanishing forces in this direction, $\sigma_{zz} = 0$.

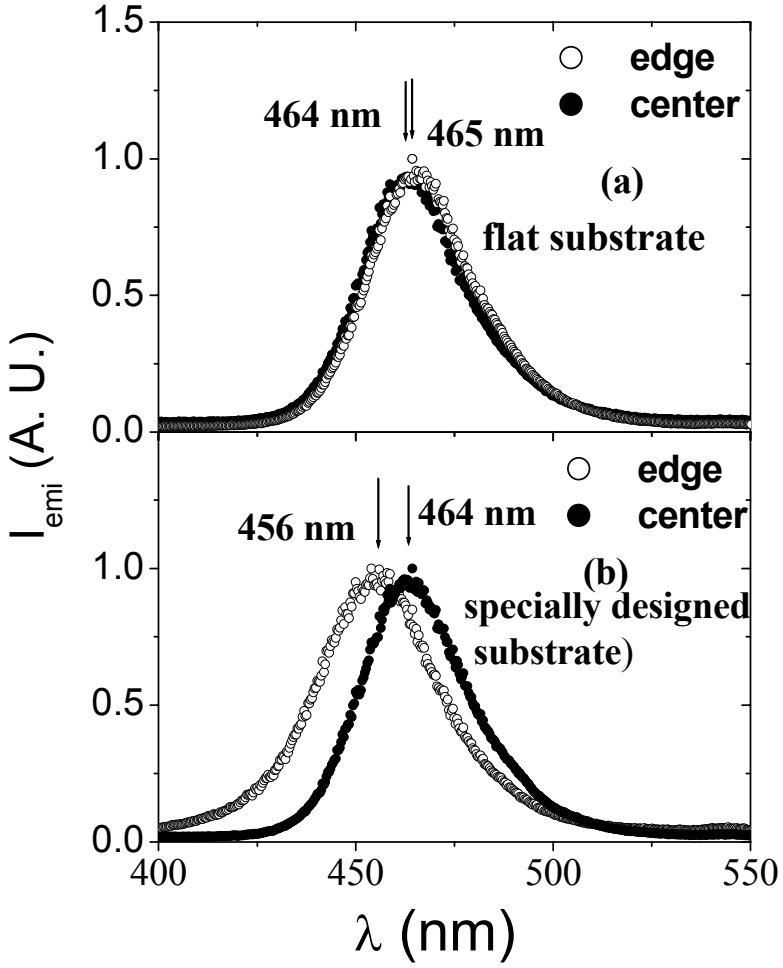

Figure 3.27 Electroluminescence spectra of blue LED grown on (a) flat and (b) specially designed substrates.

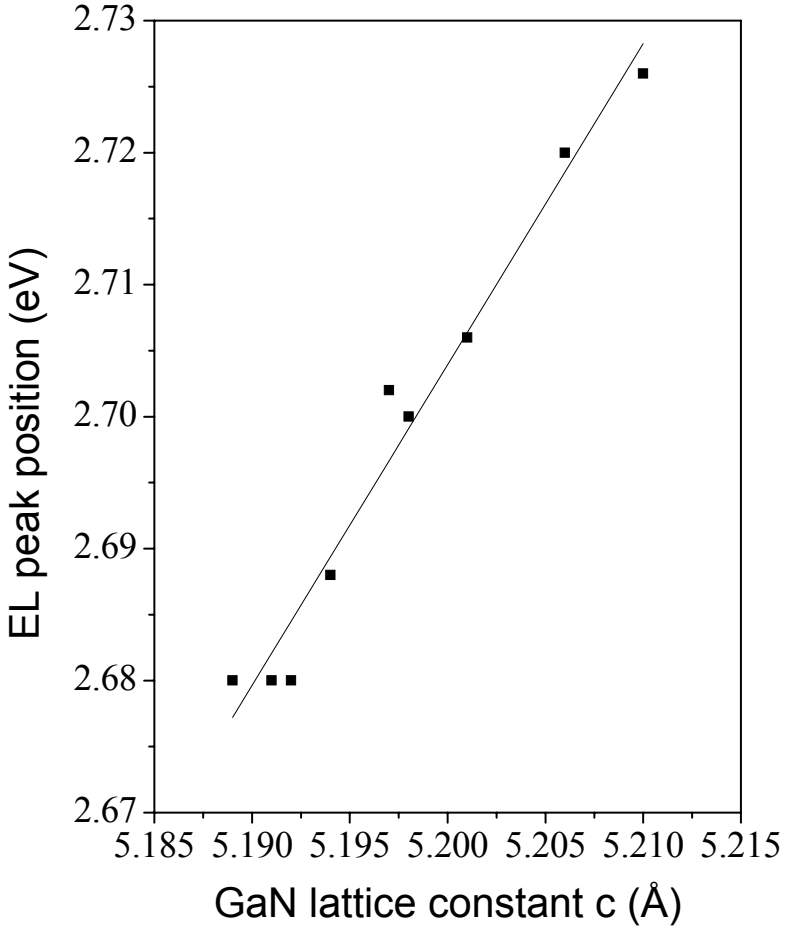

Figure 3.28 Plot of GaN lattice constant "c" verses emission energy of blue LED wafer grown on specially designed substrate.

The relationship between two components ε_{xx} and ε_{zz} of the strain tensor follows with a coefficient of $-C_{33}/2C_{13}$ and Eq. (3.1) will take the form

$$\sigma_{xx} = -[C_{13} - (C_{11} + C_{12}) C_{33}/2C_{13}]\Delta c/c_o, \quad (3.6)$$

Here the negative sign represents the compressive stress[122]. Where, C_{13}, C_{11}, C_{12}, C_{33} are the elastic stiffness constants and Δc is the lattice constant change of $In_{0.2}Ga_{0.8}N$. We found elastic stiffness constants of $In_{0.2}Ga_{0.8}N$ by assuming the linear relation between elastic stiffness constants of GaN and InN. For $In_{0.2}Ga_{0.8}N$ alloy, $C_{11} = 350$ GPa, $C_{12} = 137$ GPa, $C_{13} = 109$ GPa and $C_{33} = 355$ GPa. Eq. 6 can be written as $\sigma_{xx} = 129\ \Delta c$ and Eq. 3.5 as follows

$$E_g = 2.67 + 129B\Delta c, \quad (3.7)$$

Since we do not know the Δc of $In_{0.2}Ga_{0.8}N$ so if we assume Δc of $In_{0.2}Ga_{0.8}N$ is comparable to that of Δc of GaN, we can compare Eq. (3.7) and Eq. (3.4) to get the linear coefficient "B" of $In_{0.2}Ga_{0.8}N$, which we found was ~19 meV/GPa.

In conclusion, an off-cut of ±0.3 degree provides the optimum atomic step density for smooth growth by MOCVD. The strain effects on the emission properties of InGaN/GaN MQWs were studied using a single blue LED wafer possessing a continuous variation in compressive strain. Experimentally, a ratio of elastic stiffness constants $(C_{33}/C_{13}) \sim 5.0 \pm 1.0$ for GaN was deduced, which was in agreement with calculated value of ~ 4.0. The EL emission peak position of LEDs varies linearly with the biaxial strain. And coefficient of 19 meV/GPa, characterizing the relationship between the band gap energy and biaxial stress of $In_{0.2}Ga_{0.8}N$/GaN MQWs was obtained.

CHAPTER 4 - General Conclusions

In-rich $In_xGa_{1-x}N$ ($x \leq 0.4$) epilayers were grown on sapphire substrates by MOCVD and were characterized by XRD and photoluminescence PL. The Indium concentration was found to be sensitive to growth temperature. As growth temperature was increased from 720 to 800^oC, the indium content decreased almost linearly from 27% to 5%. XRD measurements showed InGaN films with an Indium incorporation of 37% with single phase, but for films with higher than 37%, phase separation occurred. To understand the issue of phase separation in Ga-rich InGaN, studies on growth of pure InN and In-rich InGaN alloys were carried out.

InN and In-rich $In_xGa_{1-x}N$ (x~0.97- 0.40) epilayers were grown on AlN/Al_2O_3 templates. A Hall mobility of 1400 cm^2/Vs with a carrier concentration of $7x10^{18}cm^{-3}$ at room temperature was observed for InN epilayers grown on AlN templates, which is so far the highest value reported for MOCVD grown InN epilayers. After growth process optimization, In- rich $In_xGa_{1-x}N$ alloys with (x= 0.97-0.40) were successfully grown without phase separation. The photoluminescence emission spectra revealed band to band emission peak at ~0.75 eV for InN and shifted to 1.15 eV by changing Indium percentage from 100 % to 63% in In-rich InGaN alloys.

Achieving p-type conduction is essential for many semiconductor device applications but has been exceedingly difficult in InN and In-rich InGaN alloys due to the fact that InN contains an electron accumulation layer on its surface that contributes to n-type conductivity. A detailed study of electrical properties and optical transitions in Mg-doped InN before and after annealing was undertaken. Hall effect measurement of Mg-doped InN epilayers revealed, electron compensation by Mg acceptors was incomplete; increasing the Mg flow rate from 8.5 to 60 ml/min reduced the free electron concentration (n) from $2x10^{19}$ cm^{-3} to $3x10^{18}$ cm^{-3} and n-type conductivity (σ) from 1250 to 125 $(\Omega\text{-cm})^{-1}$ upon post growth thermal annealing at 500^oC for 4 min. However, due to the presence of surface electron accumulation layer, the effects of post growth thermal annealing processes seem rather complicated and remain to be understood. The Mg acceptor binding energy of 60 meV in InN by photoluminescence studies, from our

present work matches well with a reported value of about 61 meV observed in Mg-doped InN epilayers grown by molecular beam epitaxy.

Orientation of substrate plays critical role in determining quality of films. Vicinal or off-cut substrates are interesting as they provide smoother growth, lower dislocation densities, higher quality films and improved optical properties, Toward these goals, the effects of mis-orientaion from the (0001) plane of sapphire were examined through growth of blue (~ 460nm) light emitting diodes incorporating InGaN/GaN QWs on a spherically polished sapphire substrate. An off-cut of ±0.3 degree provides the optimum atomic step density for smooth growth by MOCVD.

The strain effects on the emission properties of InGaN/GaN MQWs through the use of a single blue LED wafer that possesses a continuous variation in compressive strain were also studied. Experimentally, a ratio of elastic stiffness constants (C_{33}/C_{13}) ~ 5.0 ± 1.0 for GaN was deduced, which was in agreement with calculated value of ~ 4.0. The EL emission peak position of LEDs varies linearly with the biaxial strain, and a linear coefficient of 19 meV/GPa characterizing the relationship between the band gap energy and biaxial stress of $In_{0.2}Ga_{0.8}N$/GaN MQWs was obtained.

We obtained InN and In-rich InGaN epilayers with In content from 0.97-0.40 without phase separation. Phase separation was suppressed successfully and growth parameters were optimized to improve the crystalline quality. Quality was good enough to allow us to probe the photoluminescence from 97% to 63% In content, which supported us to determine the bandgap energy for these percentages. MOCVD grown InN and In-rich InGaN epilayers suffer from very large root mean square values of roughness as compared to GaN and AlN. More studies are needed to improve the surface morphology and quality of these epilayers to realize optical devices, employing InN/InGaN quantum wells as well as for solar cell applications. Employing different intermediate layers between InN, In-rich InGaN and underneath templates may help to improve the crystalline quality and surface morphology.

References

1. Razeghi, M. and M. Henini, *Optoelectronic devices: III-Nitrides*. Ist ed. 2004: Elsevier Ltd.
2. Nakamura, S., *Circuits and Devices.* Institute of Electrical and Electronics Engineers, May 19 (1995).
3. Matsuoka, T., Okamoto, H., Nakao, M., Harima, H., and Kurimoto, E. *Optical Bandgap Energy of Wurtzite InN.* Applied Physics Letters, 2002. **81**(7): pp. 1246-1248.
4. http://en.wikipedia.org/wiki/Wurtzite_(crystal_structure).
5. Jain, S.C., Willander, M., Narayan, J., and Van Overstraeten, R. *III-nitrides: Growth, characterization, and properties.* Journal of Applied Physics, 2000. **87**(3): pp. 965-1006.
6. Fichter, F., *Uber aluminumnitride*. Z. Anorg. Chem., 1907. **54**: p. 322.
7. Fichter, F.and Schroter, F., Berichte der Deutschen Chemischen Gesellschaft, 1910. **43**: p. 1465.
8. Johnson, V.C., Parsons, J. B. and Crew, M. C., *Nitrogen compounds of gallium. I, II*, Journal of physical chemistry, 1932. **36**: p. 2588.
9. Maruska, H.P. and J.J. Tietjen, *Preparation and properties of vapor-deposited single-crystalline GaN,* Applied Physics Letters, 1969. **15**(10): p. 327-&.
10. Manasevi, H.M, Erdmann, F.M. and Simpson,W. I., *Use of Metalorganics preparation of semiconductor materials .4. Nitrides of Aluminum and Gallium.* Journal of the Electrochemical Society, 1971. **118**(11): p. 1864-&.
11. Yoshida, S., S. Misawa, and S. Gonda, *Improvements on the Electrical and Luminescent properties of reactive molecular-beam epitaxially grown GaN films by using AlN-coated sapphire substrates.* Applied Physics Letters, 1983. **42**(5): p. 427-429.
12. Amano, H., Kito, M., Hiramatsu, K., and Akasaki, I., *P-Type conduction in Mg-Doped GaN treated with low-energy electron-beam irradiation (LEEBI).* Japanese Journal of Applied Physics Part 2-Letters, 1989. **28**(12): p. L2112-L2114.

13. Nakamura, S., Mukai, T., Senoh, M., and Iwasa, N., *Thermal annealing effects on P-Type Mg-doped GaN Films.* Japanese Journal of Applied Physics Part 2-Letters, 1992. **31**(2B): p. L139-L142.
14. Kamiyama, S., Iida, K., Kawashima, T., Kasugai, H., Mishima, S., Honshio, A., Miyake, Y., Iwaya, M., Amano, H., and Akasaki, I., *UV laser diode with 350.9-nm-lasing wavelength grown by hetero-epitaxial-lateral overgrowth Technology,* Institute of Electrical and Electronics Engineers, Journal of Selected Topics in Quantum Electronics, 2005. **11**(5): p. 1069-1073.
15. Nakamura, S., M. Senoh, and T. Mukai, *High-power InGaN/GaN double-heterostructure violet light-emitting-diodes.* Applied Physics Letters, 1993. **62**(19): p. 2390-2392.
16. Nakamura, S., M. Senoh, and T. Mukai, *P-GaN/N-InGaN/N-GaN double-heterostructure blue-light-emitting diodes.* Japanese Journal of Applied Physics Part 2-Letters, 1993. **32**(1A-B): p. L8-L11.
17. Nakamura, S., T. Mukai, and M. Senoh, *Candela-class high-brightness InGaN/AlGaN double-heterostructure blue-light-emmitting diodes.* Applied Physics Letters, 1994. **64**(13): p. 1687-1689.
18. Nakamura, S., T. Mukai, and M. Senoh, *High-brightness InGaN/AlGaN double-heterostructure blue-green-light-emitting diodes.* Journal of Applied Physics, 1994. **76**(12): p. 8189-8191.
19. Nakamura, S., Senoh, N., Iwasa, N., and Nagahama, S. I., *High-brightness InGaN blue,green and yellow light-emitting-diodes with quantum-well structures.* Japanese Journal of Applied Physics Part 2-Letters, 1995. **34**(7A): p. L797-L799.
20. Yasan, A., McClintock, R., Mayes, K., Shiell, D., Gautero, L., Darvish, S. R., Kung, P., and Razeghi, M., *4.5 mW Operation of AlGaN-based 267 nm deep-ultraviolet light-emitting diodes.* Applied Physics Letters, 2003. **83**(23): p. 4701-4703.
21. Yasan, A., McClintock, R., Mayes, K., Darvish, S. R., Zhang, H., Kung, P., Razeghi, M., Lee, S. K., and Han, J. Y.*Comparison of ultraviolet light-emitting diodes with peak emission at 340 nm grown on GaN substrate and sapphire.* Applied Physics Letters, 2002. **81**(12): p. 2151-2153.

22. Mahboob, I., Veal, T. D., McConville, C. F., Lu, H., and Schaff, W. J., *Intrinsic electron accumulation at clean InN surfaces.* Physical Review Letters, 2004. **92**(3): p. 036804.
23. Fu, S.P., T.T. Chen, and Y.F. Chen, *Photoluminescent properties of InN epifilms.* Semiconductor Science and Technology, 2006. **21**(3): p. 244-249.
24. Carrier, P. and S.H. Wei, *Theoretical study of the band-gap anomaly of InN.* Journal of Applied Physics, 2005. **97**(3).
25. Walukiewicz, W., *Narrow band gap group III-nitride alloys.* Physica E-Low-Dimensional Systems & Nanostructures, 2004. **20**(3-4): p. 300-307.
26. Walukiewicz, W., Ager, J. W., Yu, K. M., Liliental-Weber, Z., Wu, J., Li, S. X., Jones, R. E., and Denlinger, J. D., *Structure and electronic properties of InN and In-rich group III-nitride alloys.* Journal of Physics D-Applied Physics, 2006. **39**(5): p. R83-R99.
27. Wei, S.H., Nie, X. L., Batyrev, I. G., and Zhang, S. B., *Breakdown of the band-gap-common-cation rule: The origin of the small band gap of InN.* Physical Review B, 2003. **67**(16).
28. Wu, J., Walukiewicz, W., Yu, K. M., Ager, J. W., Haller, E. E., Lu, H., Schaff, W. J., Saito, Y., and Nanishi, Y., *Unusual properties of the fundamental band gap of InN.* Applied Physics Letters, 2002. **80**(21): p. 3967-3969.
29. Wu, J., Walukiewicz, W., Yu, K. M., Shan, W., Ager, J. W., Haller, E. E., Lu, H., Schaff, W. J., Metzger, W. K., and Kurtz, S., *Superior radiation resistance of $In_{1-x}Ga_xN$ alloys: Full-solar-spectrum photovoltaic material system.* Journal of Applied Physics, 2003. **94**: p. 6477-6482.
30. Wu, J., Walukiewicz, W., Shan, W., Yu, K. M., Ager, J. W., Li, S. X., Haller, E. E., Lu, H., and Schaff, W. J., *Temperature dependence of the fundamental band gap of InN.* Journal of Applied Physics, 2003. **94**(7): p. 4457-4460.
31. Mohammad, S.N. and H. Morkoc, *Progress and prospects of group-III nitride semiconductors.* Progress in Quantum Electronics, 1996. **20**(5-6): p. 361-525.
32. Chin, V.W.L., T.L. Tansley, and T. Ostochan, *Electron mobilities in gallium, indium, and aluminum nitrides.* Journal of Applied Physics, 1994. **75**(11): p. 7365-7372.

33. Lu, H., Schaff, W. J., Eastman, L. F., Wu, J., Walukiewicz, W., Look, D. C., and Molnar, R.J., *Growth of thick InN by molecular beam epitaxy.* Materials Research Society Symposium Proceedings, 2003. **743**(L4.10.1).
34. Bhuiyan, A.G., A. Hashimoto, and A. Yamamoto, *Indium nitride (InN): A review on growth, characterization, and properties.* Journal of Applied Physics, 2003. **94**(5): p. 2779-2808.
35. Ager, J. W and Walukiewicz. W, *High efficiency radiation hard solar cells,* Lawrence Berkeley National Laboratory report 56326, 2004.
36. Nakamura, S., *The Blue Laser Diode*. 2nd Ed. 2000, Berlin: Springer.
37. Che, S.B., Shinada, T., Mizuno, T., Wang, X. Q., Ishitani, Y., and Yoshikawa, A., *Effect of precise control of V/III ratio on In-rich InGaN epitaxial growth.* Japanese Journal of Applied Physics Part 2-Letters & Express Letters, 2006. **45**(46-50): p. L1259-L1262.
38. Davydov, V.Y., Klochikhin, A. A., Emtsev, V. V., Smirnov, A. N., Goncharuk, I. N., Sakharov, A. V., Kurdyukov, D. A., Baidakova, M. V., Vekshin, V. A., Ivanov, S. V., C.G., Van de Wall, Graul, J., Hashimoto, A., and Yamamoto, A. *Photoluminescence and Raman study of hexagonal InN and in-rich InGaN alloys.* Physica Status Solidi B-Basic Research, 2003. **240**(2): p. 425-428.
39. Hori, M., Kano, K., Yamaguchi, T., Saito, Y., Araki, T., Nanishi, Y., Teraguchi, N., and Suzuki, A. *Optical properties of InxGa1-xN with entire alloy composition on InN buffer layer grown by RF-MBE.* Physica Status Solidi B-Basic Research, 2002. **234**(3): p. 750-754.
40. Wu, J., Walukiewicz, W., Yu, K. M., Ager, J. W., Haller, E. E., Lu, H., and Schaff, W. J., *Small band gap bowing in $In_{1-x}Ga_xN$ alloys.* Applied Physics Letters, 2002. **80**(25): p. 4741-4743.
41. Naoi, H., Kurouchi, M., Muto, D., Araki, T., Miyajima, T., and Nanishi, Y., *Growth of high-quality In-rich InGaN alloys by RF-MBE for the fabrication of InN-based quantum well structures.* Journal of Crystal Growth, 2006. **288**(2): p. 283-288.
42. Doppalapudi, D., Basu, S. N., Ludwig, K. F., and Moustakas, T. D., *Phase separation and ordering in InGaN alloys grown by molecular beam epitaxy.*

Journal of Applied Physics, 1998. **84**(3): p. 1389-1395.

43. El-Masry, N.A., Piner, E. L., Liu, S. X., and Bedair, S. M., *Phase separation in InGaN grown by metalorganic chemical vapor deposition.* Applied Physics Letters, 1998. **72**(1): p. 40-42.
44. Wu, J., Walukiewicz, W., Li, S. X., Armitage, R., Ho, J. C., Weber, E. R., Haller, E. E., Lu, H., Schaff, W. J., Barcz, A., and Jakiela, R., *Effects of electron concentration on the optical absorption edge of InN.* Applied Physics Letters, 2004. **84**(15): p. 2805-2807.
45. Wu, J., Walukiewicz, W., Shan, W., Yu, K. M., Ager, J. W., Haller, E. E., Lu, H. and Schaff, W. J., *Effects of the narrow band gap on the properties of InN.* Physical Review B, 2002. **66**(20).
46. Janotti, A. and C.G.V. de Walle, *Sources of unintentional conductivity in InN.* Applied Physics Letters, 2008. **92**(3): p. 032104.
47. Look, D.C., Lu, H., Schaff, W. J., Jasinski, J., and Liliental-Weber, Z., *Donor and acceptor concentrations in degenerate InN.* Applied Physics Letters, 2002. **80**(2): p. 258.
48. Stampfl, C., Van de Wall C.G., Vogel, D., Kruger, P., and Pollman, J., *Native defects and impurities in InN: First-principles studies using the local-density approximation and self-interaction and relaxation-corrected pseudopotentials.* Physical Review B, 2000. **61**: p. R7846.
49. Tansley, T.L. and Egan, R.J., *Point-Defect Energies in the Nitrides of Aluminum, Gallium, and Indium.* Physical Review B, 1992. **45**(19): p. 10942.
50. Jenkins, D.W. and J.D. Dow, *Electronic-Structures and Doping of InN, $In_xGa_{1-X}N$, and $In_xAl_{1-X}N$.* Physical Review B, 1989. **39**(5): p. 3317.
51. Yamamoto, A., Murakami, Y., Koide, K., Adachi, M., and Hashimoto, A., *Growth temperatue dependences of MOVPE InN on sapphire substrates.* Physica Status Solidi B, 2001. **228**: p. 5.
52. Yamamoto, A., Tanaka, T., Koide, K., and Hashimoto, A., *Improved electrical properties of metalorganic chemical vapor phase epitaxial InN films.* Physica Status Solidi A, 2002. **194**: p. 510.

53. Segev, D. and Van de Walle, C.G., *Origins of fermi-level pinning on GaN and InN polar and nonpolar surfaces.* Europhysics Letters, 2006. **76**(2): p. 305.
54. Lu, H., Schaff, W. J., Eastman, L. F., and Stutz, C. E., *Surface charge accumulation of InN films grown by molecular-beam epitaxy.* Applied Physics Letters, 2003. **82**(11): p. 1736-1738.
55. Anderson, P.A., Swartz, C. H., Carder, D., Reeves, R. J., Durbin, S. M., Chandril, S., and Myers, T. H., *Buried p-type layers in Mg-doped InN.* Applied Physics Letters, 2006. **89**(18).
56. Veal, T.D., Piper, L.F. J., Schaff, W. J., Mc Conville, C. F., *Inversion and accumulation layers at InN surfaces.* Journal of Crystal Growth, 2006. **288**(2): p. 268.
57. Jones, R.E., Yu, K. M., Li, S. X., Walukiewicz, W., Ager, J. W., Haller, E. E., Lu, H., and Schaff, W. J., *Evidence for p-type doping of InN.* Physical Review Letters, 2006. **96**(12).
58. Walukiewicz. W., Li. S.X., Wu. J., Yu. K. M, Ager III, Haller. E. E., Lu. H., Schaff. W. J., *Optical properties and electronic structure of InN and In-rich group III-nitride alloys.* Journal of crystal growth, 2004, **269**(119).
59. Takahashi. K., Yoshikawa. A., and Sandhu. A, *Wide band gap semiconductors.* 2007: (Springer - Verlag Berlin Heidelberg), p. 7.
60. Fewster, P.F., *X-ray scattering from semiconductors.* 2003: (Imperial college press London).
61. Matsuoko, T., Yoshimoto, N., Sasaki T., and Katsui A.,*Wide-gap semiconductor InGaN and InGaAlN grown by MOVPE,* Journal of Electronic Materials, 1992. **21**: p. 157.
62. Ho, I.H. and G.B. Stringfellow, *Solid phase immiscibility in InGaN.* Applied Physics Letters, 1996. **69**(18): p. 2701-2703.
63. Piner, E.L., McIntosh, F. G., Roberts, J. C., Boutros, K. S., Aumer, M. E., Joshkin, V. A., El-Masry, N. A., Bedair, S. M., and Liu, S. X., *A model for indium incorporation in the growth of InGaN films,* Materials Research Society Symposium Proceedings, 1997. **449**: p. 85.

64. Matsuoko, T., T. Sakai, and A. Katsui, *Growth and properties of a wide band gap semiconductor InGaN,* Optoelectronic devices and technologies, 1990. **5**: p. 53.
65. Karpov, S.Y., *Suppression of phase separation in InGaN due to elastic strain.* Mrs Internet Journal of Nitride Semiconductor Research, 1998. **3**(16).
66. Singh, R., Herzog. W. D., Doppalapudi, D., Unlu, M. S., Goldberg, B. B., and Moustakas, T. D., *MBE growth and optical characterization of InGaN/AlGaN multi-quantum wells*, Materials Research Society Symposium Proceedings, 1997. **449**: p. 185.
67. Singh, R., Doppalapudi, D., Moustakas, T. D., and Romano, L. T., *Phase separation in InGaN thick films and formation of InGaN/GaN double heterostructures in the entire alloy composition.* Applied Physics Letters, 1997. **70**(9): p. 1089-1091.
68. Singh, R. and T.D. Moustakas, *Growth of InGaN films by MBE at growth temperature of GaN,* Materials Research Society Symposium Proceedings, 1996. **395**: p. 163.
69. Wakahara, A., Tokuda, T., Dang, X. Z., Noda, S. and Sasaki, A., *Compositional inhomogeneity and immiscibility of a GaInN ternary alloy.* Applied Physics Letters, 1997. **71**(7): p. 906-908.
70. Nanishi, Y., Y. Saito, and T. Yamaguchi, *RF-molecular beam epitaxy growth and properties of InN and related alloys.* Japanese Journal of Applied Physics Part 1-Regular Papers Short Notes & Review Papers, 2003. **42**(5A): p. 2549-2559.
71. Yang, F.H., Hwang, J. S., Yang, Y. J., Chen, K. H., and Wang, J. H., *Growth of high-quality epitaxial InN film with high-speed reactant gas by organometallic vapor-phase epitaxy.* Japanese Journal of Applied Physics Part 2-Letters, 2002. **41**(11B): p. L1321-L1324.
72. Bellotti, E., Doshi, B. K., Brennan, K. F., Albrecht, J. D., and Ruden, P. P., *Ensemble Monte Carlo study of electron transport in wurtzite InN.* Journal of Applied Physics, 1999. **85**(2): p. 916-923.
73. Foutz, B.E., O'Leary, S. K., Shur, M. S., and Eastman, L. F., *Transient electron transport in wurtzite GaN, InN, and AlN.* Journal of Applied Physics, 1999. **85**(11): p. 7727-7734.

74. Pantha, B.N., Dahal, R., Li, J., Lin, J. Y., Jiang, H. X., and Pomrenke, G., *Thermoelectric properties of $In_xGa_{1-x}N$ alloys.* Applied Physics Letters, 2008. **92**.
75. Foutz, B.E., Ambacher, O., Murphy, M. J., Tilak, V., Eastman, L. F., *Polarization induced charge at heterojunctions of the III-V nitrides and their alloys.* Physica Status Solidi B, 1999. **216**: p. 415.
76. Bhuiyan, A.G., Tanaka, T., Yamamoto, A., and Hashimoto, A., *Laser-assisted metalorganic vapor-phase epitaxy (LMOVPE) of indium nitride (InN).* Physica Status Solidi A, 2002. **194**: p. 502.
77. Wang, X.Q., Che, S. B., Ishitani, Y., and Yoshikawa, A., *Growth and properties of Mg-doped in-polar InN films.* Applied Physics Letters, 2007. **90**(20).
78. Lu, H., Schaff, W. J., Hwang, J., Wu, H., Koley, G., and Eastman, L. F., *Effect of an AlN buffer layer on the epitaxial growth of InN by molecular-beam epitaxy.* Applied Physics Letters, 2001. **79**(10): p. 1489-1491.
79. Yamamoto, A., Miwa, H., Shibata, Y., and Hashimoto, A., *NH_3/TMI molar ratio dependence of electrical and optical properties for atmospheric-pressure MOVPE InN.* Physica Status Solidi C, 2006. **3**: p. 1527.
80. Chang, C.A., Shih, C. F., Chen, N. C., Chang, P., and Liu, K.S., *High mobility InN films grown by metal-organic vapor phase epitaxy.* Physica Status Solidi C, 2004. **1**: p. 2559.
81. Wu, C.L., C.H. Shen, and S. Gwo, *Valence band offset of wurtzite InN/AlN heterojunction determined by photoelectron spectroscopy.* Applied Physics Letters, 2006. **88,** 032105.
82. Pantha, B.N., Dahal, R., Nakarmi, M. L., Nepal, N., Li, J., Lin, J. Y., Jiang, H. X., Paduano, Q. S., and Weyburne, D., *Correlation between optoelectronic and structural properties and epilayer thickness of AIN.* Applied Physics Letters, 2007. **90**(24): p: 241101
83. Pantha, B.N., Nepal, N., Al Tahtamouni, T. M., Nakarmi, M. L., Li, J., Lin, J. Y., and Jiang, H. X. *Correlation between biaxial stress and free exciton transition in AlN epilayers.* Applied Physics Letters, 2007. **91**. p. 121117

84. Higashiwaki, M. and T. Matsui, *Epitaxial growth of high-quality InN films on sapphire substrates by plasma-assisted molecular-beam epitaxy.* Journal of Crystal Growth, 2003. **252**(1-3): p. 128.

85. Davydov, V.Y., Klochikhin, A. A., Emtsev, V. V., Ivanov, S. V., Vekshin, V. V. Bechstedt, F., Furthmuller, J., Harima, H., Mudryi, A. V., Hashimoto, A., Yamamoto, A., Aderhold, J.,Graul, J., and Haller, E. E., *Band gap of InN and In-rich $In_xGa_{1-x}N$ alloys (0.36 < x < 1).* Physica Status Solidi B-Basic Research, 2002. **230**(2): pp. R4-R6.

86. Higashiwaki, M., T. Inushima, and T. Matsui, *Control of electron density in InN by Si doping and optical properties of Si-doped InN.* Physica Status Solidi B-Basic Research, 2003. **240**(2): p. 417.

87. Sugita, K., Takatsuka, H., Hashimoto, A., and Yamamoto, A., *Photoluminescence and optical absorption edge for MOVPE-grown InN.* Physica Status Solidi B-Basic Research, 2003. **240**(2): p. 421.

88. Semchinova, O.K., Aderhold, J., Graul, J., Filimonov, A. and Neff, H., *Photoluminescence, depth profile, and lattice instability of hexagonal InN films.* Applied Physics Letters, 2003. **83**(26): p. 5440.

89. Davydov, V.Y., Klochikhin, A. A., Seisyan, R. P., Emtsev, V. V., Ivanov, S. V., Bechstedt, F., Furthmuller, J., Harima, H., Mudryi, V., Aderhold, J., Semchinova, O., and Graul, J., *Absorption and emission of hexagonal InN. Evidence of narrow fundamental band gap.* Physica Status Solidi B-Basic Research, 2002. **229**(3): pp. R1-R3.

90. Tansley, T.L. and C.P. Foley, *Optical Band-Gap of Indium Nitride.* Journal of Applied Physics, 1986. **59**(9): p. 3241.

91. Iliopoulos, E., Georgakilas, A., Dimakis, E., Adikimenakis, A., Tsagaraki, K., Androulidaki, M., and Pelekanos, N. T., *InGaN(0001) alloys grown in the entire composition range by plasma assisted molecular beam epitaxy.* Physica Status Solidi A-Applications and Materials Science, 2006. **203**(1): p. 102.

92. Chang, C.A., Shih, C. F., Chen, N. C., Lin, T. Y., and Liu, K. S., *In-rich $In_{1-x}Ga_xN$ films by metalorganic vapor phase epitaxy.* Applied Physics Letters, 2004. **85**(25): p. 6131-6133.

93. Briot, O., Maleyre, B., Ruffenach, S., Gil, B., Pinquier, C., Demangeot, F., Frandon, J., *Absorption and raman scattering processes in InN films and dots.* Journal of Crystal Growth, 2004. **269**(1): p. 22-28.

94. Intartagilla, R., Maleyre, B., Ruffenach, S., Briot, O., Taliercio, T. and Gil, B., *Radiative and nonradiative recombination processes in InN films grown by metal organic chemical vapor deposition.* Applied Physics Letters, 2005. **86**(14).

95. Davydov, V.Y. and A.A. Klochikhin, *Electronic and vibrational states in InN and $In_xGa_{1-x}N$solid solutions.* Semiconductors, 2004. **38**(8): p. 861-898.

96. Li, S.X., Yu, K. M., Wu, J., Jones, R., Walukiewicz, W., Ager, J. W.,Shan, W., Haller, E. E., Lu, H., and Schaff, W. J.., *Fermi-level stabilization energy in group III nitrides.* Physical Review B, 2005. **71**(16).

97. Johnson, M.C., Konsek, S. L., Zettl, A., and Bourret-Courchesne, E. D., *Nucleation and growth of InN thin films using conventional and pulsed MOVPE.* Journal of Crystal Growth, 2004. **272**(1-4): p. 400-406.

98. Cimalla, V., Niebelschutz, M., Ecke, G., Lebedev, V., Ambacher, O., Himmerlich, M., Krischok, S., Schaefer, J. A.,Lu, H., and Schaff, W. J., *Surface band bending at nominally undoped and Mg-doped InN by Auger electron spectroscopy.* Physica Status Solidi a-Applications and Materials Science, 2006. **203**(1): p. 59-65.

99. Cimalla, V., Niebelschutz, M., Ecke, G., Ambacher, O., Goldhahn, R., Lu, H. and Schaff, W. J., *The conductivity of Mg doped InN.* Physica status Solidi C, 2006. **3**: p. 1721.

100. Mamutin, V.V., Vekshin, V. A., Davydov, V. Y., Ratnikov, V. V., Kudriavtsev, Y. A., Ber, B. Y., Emtsev, V. V., and Ivanov, S. V., *Mg-doped hexagonal InN/Al_2O_3 films grown by MBE.* Physica Status Solidi a-Applied Research, 1999. **176**(1): p. 373-378.

101. Blant, A.V., Cheng, T. S., Jeffs, N. J., Flannery, L. B., Harrison, I., Mosselmans, J. F. W. Smith, A. D., and Foxon, C. T., *EXAFS studies of Mg doped InN grown on Al_2O_3.* Materials Science and Engineering B-Solid State Materials for Advanced Technology, 1999. **59**(1-3): p. 218-221.

102. Shu, G.W., Wu, P. F., Lo, M. H., Shen, J. L., Lin, T. Y., Chang, H. J., Chen, Y. F. Shih, C. F., Chang, C. A., and Chen, N. C., *Concentration dependence of carrier*

localization in InN epilayers. Applied Physics Letters, 2006. **89**(13).

103. Boer, K.W., *Electrons and other particles in bulk semiconductors.* 1990: p. 240.
104. Fu, S.P. and Y.F. Chen, *Effective mass of InN epilayers.* Applied Physics Letters, 2004. **85**(9): p. 1523-1525.
105. Li, S.X., Jones, R. E., Haller, E. E., Yu, K. M., Walukiewicz, W., Ager, J.W., Liliental-Weber, Z., Lu, H., and Schaff, W. J., *Photoluminescence of energetic particle-irradiated $In_xGa_{1-x}N$ alloys.* Applied Physics Letters, 2006. **88**.
106. Lachab, M., Youn, D. H., Fareed, R. S. Q., Wang, T. and Sakai, S., *Characterization of Mg-doped GaN grown by metalorganic chemical vapor deposition.* Solid-State Electronics, 2000. **44**(9): p. 1669-1677.
107. Chen, F., Cartwright, A. N., Lu, H., and Schaff, W. J., *Temperature-dependent optical properties of wurtzite InN.* Physica E-Low-Dimensional Systems & Nanostructures, 2004. **20**(3-4): p. 308-312.
108. Xie, M.H., Seutter, S.M., Zheng, L.X., Cheung, S.H., Ng, Y.F., Wu. H., and Tong, S.Y., MRS Internet J. Nitride Semicond Res., 2000. **5S1**: p. W3.29.
109. Zhao, D.G., Xu, S. J., Xie, M. H., Tong, S. Y., and Yang, H., *Stress and its effect on optical properties of GaN epilayers grown on Si(111), 6H-SiC(0001), and c-plane sapphire.* Applied Physics Letters, 2003. **83**(4): p. 677-679.
110. Rieger, W., Metzger, T., Angerer, H., Dimitrov, R., Ambacher, O., and Stutzmann, M., *Influence of substrate-induced biaxial compressive stress on the optical properties of thin GaN films.* Applied Physics Letters, 1996. **68**(7): p. 970-972.
111. Shen, X.Q., H. Matsuhata, and H. Okumura, *Reduction of the threading dislocation density in GaN films grown on vicinal sapphire(0001) substrates.* Applied Physics Letters, 2005. **86**(2).
112. Kim, S.W., H. Aida, and T. Suzuki, *The effect of a slight mis-orientation angle of c-plane sapphire substrate on surface and crystal quality of MOCVD grown GaN thin films.* Physica Status Solidi C, 2004. **1**: p. 2483.
113. Dems, M. and W. Nakwaski, *Thermal and molecular stresses in multi-layered structures of nitride devices.* Semiconductor Science and Technology, 2003. **18**(8): p. 733.

114. Bai, J., T. Wang, and S. Sakai, *Study of the strain relaxation in InGaN/GaN multiple quantum well structures.* Journal of Applied Physics, 2001. **90**(4): p. 1740.

115. Aumer, M.E., LeBoeuf, S. F., Moody, B. F., Bedair, S. M., Nam, K., Lin, J. Y. and Jiang, H. X., *Effects of tensile, compressive, and zero strain on localized states in AlInGaN/InGaN quantum-well structures.* Applied Physics Letters, 2002. **80**(17): p. 3099.

116. Perlin, P., Kisielowski, C., Iota, V., Weinstein, B. A., Mattos, L., Shapiro, N. A. Kruger, J., Weber, E. R., and Yang, J. W. *InGaN/GaN quantum wells studied by high pressure, variable temperature, and excitation power spectroscopy.* Applied Physics Letters, 1998. **73**(19): p. 2778.

117. Wagner, J.M. and F. Bechstedt, *Phonon deformation potentials of alpha-GaN and -AlN: An ab initio calculation.* Applied Physics Letters, 2000. **77**(3): p. 346.

118. Scholz, F., Bruckner, P., Habel, F., Peter, M., and Kohler, K., *Improved GaN layer morphology by hydride vapor phase epitaxy on misoriented Al2O3 wafers.* Applied Physics Letters, 2005. **87**(18).

119. Ahmad, I., Holtz, M., Faleev, N. N., and Temkin, H., *Dependence of the stress-temperature coefficient on dislocation density in epitaxial GaN grown on alpha-Al_2O_3 and 6H-SiC substrates.* Journal of Applied Physics, 2004. **95**(4): p. 1692.

120. Kuo, C.P., Vong, S. K., Cohen, R. M., and Stringfellow, G. B., *Effect of mismatch strain on Band-Gap in Iii-V Semiconductors.* Journal of Applied Physics, 1985. **57**(12): p. 5428-5432.

121. He, H.P., Zhuge, F., Ye, Z. Z., Zhu, L. P., Wang, F. Z.,Zhao, B. H., and Huang, J. Y., *Strain and its effect on optical properties of Al-N codoped ZnO films.* Journal of Applied Physics, 2006. **99**(2).

122. Senez, V., Armigliato, A., De Wolf, I., Carnevale, G., Balboni, R., Frabboni, S., and Benedetti, A., *Strain determination in silicon microstructures by combined convergent beam electron diffraction, process simulation, and micro-Raman spectroscopy.* Journal of Applied Physics, 2003. **94**(9): p. 5574-5583.

Appendix A - Research work publications

1. **N. Khan**, J. Li, “Effect of compressive strain on the optical properties of $In_xGa_{1-x}N$/ GaN quantum wells”. Appl. Phys. Lett., 89, 151916 (2006).
2. **N. Khan**, N. Nepal, A. Sedhain, J. Y. Lin and H. X. Jiang, “Mg acceptor level in InN epilayers probed by photoluminescence”. Appl. Phys. Lett., 91, 012101 (2007).
3. **N. Khan**, A. Sedhain, J. Li, J. Y. Lin, and H. X. Jiang, " High mobility InN epilayers grown on AlN epilayers grown on AlN epilayer templates”.